Postgraduate Studies Program in Physics
Physics Department, School of Sciences
University of Ioannina, Greece

Master thesis

Study of magnetic flux emergence in the solar atmosphere using numerical simulations

Evangelos Karantanis
AM: 824

Supervisor: Vasilis Archontis

Ioannina
January 2025

Examination committee

Vasilis Archontis, Professor, Physics Department, University of Ioannina (**Supervisor**).

Alexandros Nindos, Professor, Physics Department, University of Ioannina.

Spyridon Patsourakos, Associate Professor, Physics Department, University of Ioannina.

Acknowledgements

I would like to express my gratitude to the following people that have helped me throughout my thesis. First and foremost my supervisor, professor Vasilis Archontis for his guidance and support during my thesis as well as having given me the opportunity to work on an exciting topic. His expertise and insights have been crucial for this work and i am deeply greatful to him.

I also wish to thank the members of the examination committee, Professor Alexandros Nindos and Spyros Patsourakos for their instructive comments and careful appraisal of my thesis.

Furthermore i extend my gratitude to postdoc researcher, Juxhin Zhuleku for his valuable guidance and advices along with his thoughtfull feedback during my thesis. I also have a great deal of appreciation to PhD students, Angelos Giannis and Vera Agalianou for their helpful comments and encouragement.

Finally and above all, my family and friends that have unselfishly supported me, not only during this thesis, but throughout all these years.

Abstract

The subject of this master thesis is the study of magnetic flux emergence in the solar atmosphere using numerical simulations.

It is well known that various phenomena in the Sun such as solar flares, jets, coronal mass ejections (CME), are linked to magnetic structures beneath the photosphere. These structures transport magnetic flux from the deep convection zone to the photosphere and then expand in the corona. In this thesis we focus on the interaction between the emerging magnetic field and the external ambient field leading to standard jet formation and more intense eruptions known as blowout jets. To quantify the amount of energy and magnetic field transported into the solar atmosphere we conduct three-dimensional (3D), resistive magnetohydrodynamic (MHD) numerical simulations using Lare3D code. This allows us to model the emergence process and the eruptive phenomena produced in our simulations. The magnetic flux is concentrated along rigid structures located in the convection zone and we examine different topologies of those structures to understand how their characteristics affect the amount of energy that can emerge and produce transient phenomena. Given the importance of the twist of the field lines in a flux tube, we compare cases with higher ($\alpha = 0.4$) and lower ($\alpha = 0.1$) twists.

For the high twist case ($\alpha = 0.4$) we find that both tubes produce multiple jets and blowout jets. The horizontal tube releases a significant amount of energy in the corona as compared to the toroidal tube however the toroidal tube maintains an eruptive behavior for longer time albeit with less intensity. We find that the reasons behind these behavior is that the toroidal tube maintains and increases the amount of axial flux located at the upper atmosphere whereas the horizontal tube after the first two intense eruptions can no longer create and maintain axial flux which is an important factor since it is linked to the twisted magnetic field lines that lead to eruptions. For the less twisted case ($\alpha = 0.1$) the toroidal tube cannot produce any eruptions given that the field lines emergence with almost no twist and there is no further shearing motion. The horizontal tube, due to its undulation produces one eruption.

Overall, the geometrical structure of real magnetic flux tubes in the Sun is not well established therefore numerical simulations can help identify these structures by comparing them with observational data from eruptive phenomena on the Sun.

Contents

List of Figures

Introduction

1.1 General Characteristics of the Sun

The Sun is the star that is in the center of our solar system and it has an age of $\sim 4.5 \times 10^9$ years. Its spectral type is G2V and it belongs in the main sequence of the Hertzsprung-Russell diagram. From measurements of the total flux of radiation emitted in all wavelengths, we can use the Stefan-Boltzmann law $F = \sigma T_{eff}^4$ to estimate the effective temperature of the Sun's surface. This is calculated to be roughly $T_{eff} = 5800$ K. Such high temperature means that the Sun consists of hot highly ionized plasma. We can divide the Sun in roughly two areas, the interior and its atmosphere. The interior consists of several layers such as the core, the radiation zone and the convection zone. Where the atmosphere is stratified in the following consecutive layers. The photosphere, the chromosphere, the transition region and the outer layer being the corona.

Moving from the inner to the outer layers, the core is in the center of the Sun and it is there that the Sun's energy is produced via nuclear fusion. As the temperature in the core can reach up to $\sim 15 \times 10^6$ K and has a density of ~ 150 g/cm^3 , the environment in the core is suitable for hydrogen atoms to combine and produce heavier helium atoms as well as to release large amounts of energy. That energy radiates outward to the radiation zone. The temperature in the radiation zone, which is outside the core, decreases to roughly $\sim 5 \times 10^6$ K . Here the emitted photons scatter with the free particles. Because this layer is so dense, photons scatter frequently and need thousands of years to reach the end of the radiation zone. After the end of the radiation zone there is the convection zone, where energy transfer takes place through convection. This layer is much less thick than the previous ones and the temperature now drops dramatically from a few million degrees Kelvin to 5800 K. According to the Schwarzschild criterion $(-dT/dr)_{ad} < (-dT/dr)_{rad}$ we understand that when the local temperature gradient is bigger than the adiabatic temperature gradient instability will cause plasma to move upwards through convective currents.

Moving outwards to the solar atmosphere we have the photosphere, the chromosphere the transition region and the corona. The photosphere is where solar temperature reaches it's minimum of ~ 4300 K. The average temperature of the photosphere is ~ 5800 K and it gradually diminishes to higher altitudes. It has a low density of average $\sim 2 \times 10^{-4}$ kg/m^3. This layer is responsible for emitting almost all of solar radiation, mainly at optical wavelengths. After the photosphere there is the chromosphere which is an area of density that reaches as low as $\sim 1.6 \times 10^{-11}$ kg/m^3. Even though at the base of the chromosphere the temperature can be at $\sim$4300 K, in it's end it can reach up to ~ 250000 K. The next layer is the transition region, which is a very thin layer of ~ 100 km. The main characteristic of this region is that the temperature steeply increases about two orders of magnitude, from $\sim 10^4$ K to $\sim 10^6$ K. Lastly, the outermost layer of the solar atmosphere is the corona. Here the average electron density is $\sim 10^{14} m^{-3}$, and it decreases as we move outwards. The temperature of the coronal plasma is in the order of 10^6 K. Unlike the other layers of the Sun, the corona doesn't have definite boundaries. That can be seen on the left side of figure(1.1) (Α*λυσανδράκης*, Ν*ίντος*, and Π*ατσουράκος* 2016) as the corona appears to be defused in the interplanetary space. The right side of figure(1.1) (Eric Priest 2014) shows the temperature and density change throughout the solar atmosphere in regard to height. This picture shows the mean variation of the quantities since in practice the atmosphere is dynamic and highly inhomogeneous (Α*λυσανδράκης*, Ν*ίντος*, and Π*ατσουράκος* 2016).

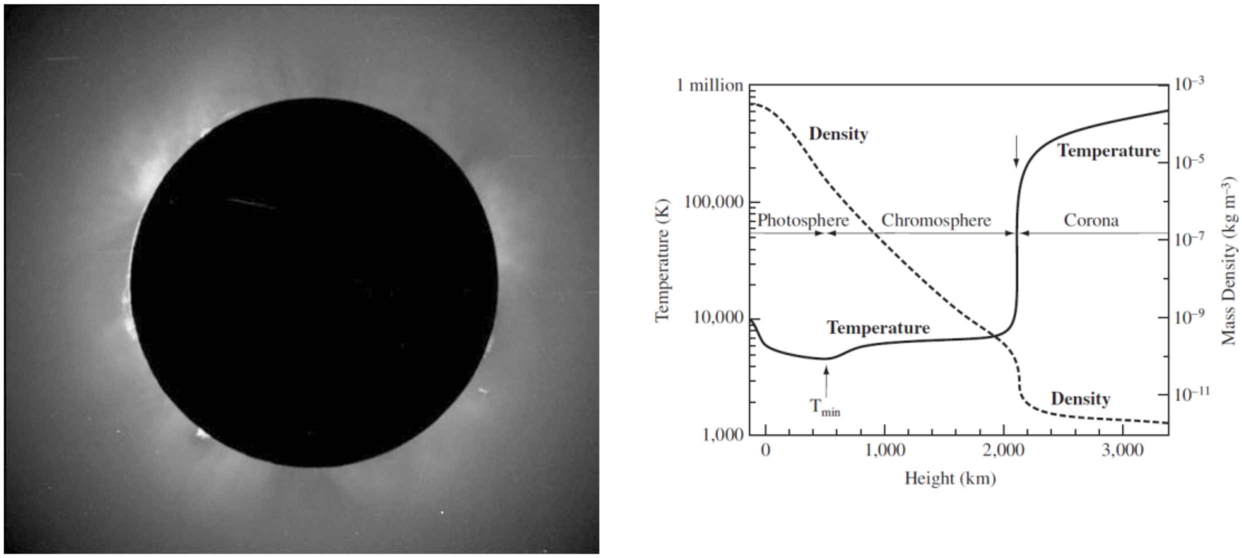

Figure 1.1: Left side is the solar corona during a total eclipse (Αλυσανδράκης, Νίντος, and Πατσουράκος 2016). Right side shows the temperature and density at different heights of the Sun (Eric Priest 2014).

1.2 Solar Active Regions

Another way of separating regions of the Sun, much like the different layers of it, is the classification of the solar surface in quiet Sun and active regions. Active regions (AR) are areas of the solar atmosphere where strong and complex magnetic fields are observed, as well as highly concentrated magnetic flux. Regions outside those comprise the quiet Sun. Active regions play a significant role in solar observations since a wide range of interesting phenomena take place there. Active regions are themselves further separated in a positive and a negative polarity region. These two opposite polarity regions are separated by a curve called neutral line or polarity-inversion line (PIL). The main observational signature in the photosphere are the solar sunspots. Sunspots are temporal structures that appear darker than the surrounding environment. They are also much colder than the rest of the photosphere because of their large magnetic field (~ 3000G) that represses upward convective flows that would otherwise transport hotter plasma from lower layers to the photosphere. The sunspots morphology consists of two regions the umbra that is very dark and the penumbra which is outside of the umbra and is less dark. The different dark shades can be seen very clearly in Figure(1.2) (Αλυσανδράκης, Νίντος, and Πατσουράκος 2016). The temperature in the umbra is ~ 3700K which justifies the darker color as the material is colder than it is in the rest of the photosphere. The magnetic field is almost normal to the surface in the umbra and as we move to the penumbra the field deviates from being vertical until it becomes almost horizontal to the photosphere. The typical length of the umbra can reach up to 20 Mkm, while the penumbra up to 50 Mkm.

At the solar corona, the magnetic field above an active region forms structures that resemble loops. In the corona as well as the photosphere, plasma movement is determined by the magnetic field and as a result, hot plasma runs along the length of the magnetic field lines that form the coronal loops. Coronal loops are large structures that connect regions of opposite polarity and at the same time extend upwards for thousands of kilometers (Aschwanden 2006).

1.3 Plasma β parameter

To further investigate the underlying physics of the solar atmosphere, we first introduce the plasma beta parameter, symbolized by β, as the ratio of plasma and magnetic pressure.

$$\beta = \frac{p}{p_{mag}} = \frac{p}{B^2/8\pi} = \frac{8\pi p}{B^2} \tag{1.1}$$

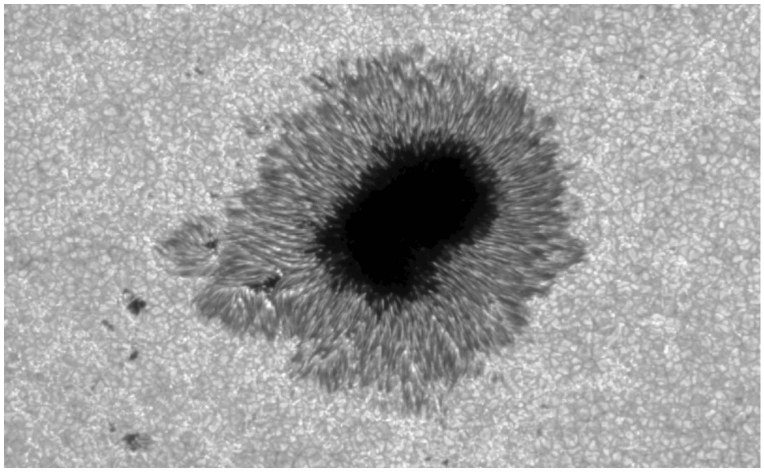

Figure 1.2: Image of a sunspot from Solar Optical Telescope of the Hinode mission (Α$\lambda\upsilon\sigma\alpha\nu\delta\rho\acute{\alpha}\kappa\eta\varsigma$, Ν$\acute{\iota}\nu\tau$ος, and Π$\alpha\tau\sigma o\upsilon\rho\acute{\alpha}\kappa$ος 2016).

A common assumption for the function that describes gas pressure is the ideal gas law, $p = nk_BT$, that changes the β parameter equation (1.1) to,

$$\beta = \frac{8\pi n k_B T}{B^2} \tag{1.2}$$

If $\beta >> 1$ it means that gas pressure prevails over plasma pressure so the plasma behaves like a hydrodynamic system. This suggests that as the plasma moves the magnetic field moves with it.
If $\beta << 1$ the magnetic pressure dominates so the dynamical movement of the plasma is determined by the magnetic field.
In the solar atmosphere for the most part the magnetic field dictates the plasma movement. However, this is not the case in the photosphere. This is illustrated in Figure(1.3) (Gary 2001).

1.4 Magnetic Flux Emergence

The term magnetic flux emergence refers to a fundamental process in the Sun since it describes the mechanism that magnetic fields are transported from the solar interior to the Sun's atmosphere. As discussed previously Active regions (ARs) are areas where there is a large concentration of magnetic field. Deep beneath these areas plasma flows emerge locally from the convection zone reaching up to the photosphere where the Active Region is formed. In order to better understand magnetic flux emergence we focus on a structure called magnetic flux tube. A magnetic flux tube is a cylindrical region of space where a magnetic field is contained in a way that the sides of the tube are always parallel to the magnetic field lines. The magnetic field lines are usually twisted and the tube could be bent in a toroidal shape. It is worth mentioning that when we refer to magnetic flux tubes we imply structures that are underneath the photosphere. In contrary twisted cylindrical or toroidal structures that are located above the photosphere are called flux ropes. This is because flux tubes are created in the solar convection zone, whereas flux ropes are created in the solar atmosphere mainly through the completely different process of magnetic reconnection.

Assuming a magnetic flux tube has been formed in the convection zone, it becomes susceptible to the buoyancy instability which allows the tube to rise through the photosphere and to appear as a bipolar region with each region being the footpoints of the tube. Suppose that the plasma pressure dominates over the magnetic pressure, $B^2/8\pi \ll p$, so the equation that describes the equilibrium between the magnetic structure and the surrounding plasma is,

$$p_{in} + \frac{B^2}{8\pi} = p_{out} \tag{1.3}$$

where p_{in} and p_{out} denotes the gas pressure inside and outside the magnetic tube respectively. If we make a

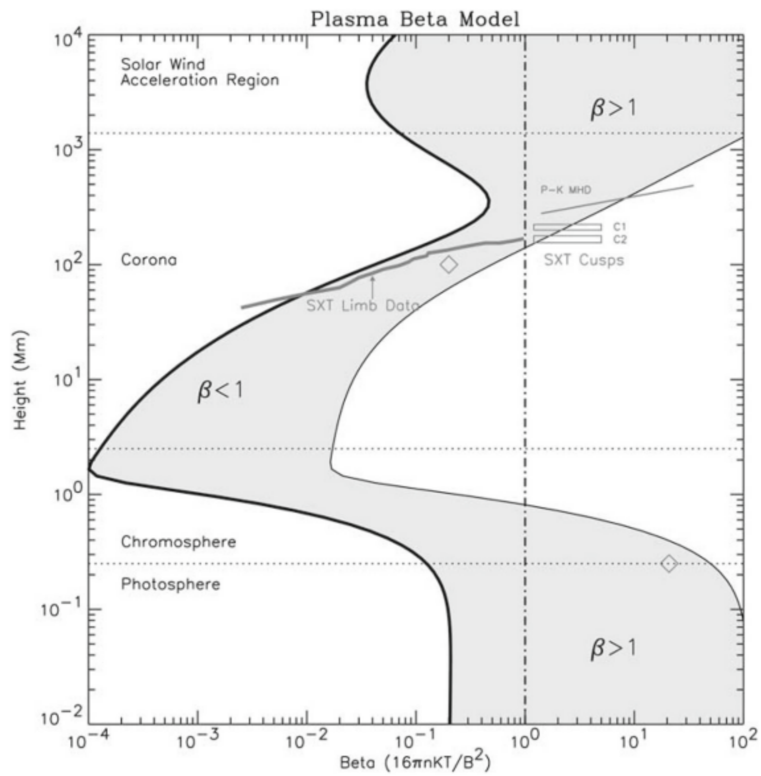

Figure 1.3: Plasma β parameter stratification above an active region (Gary 2001).

further assumption that the magnetic tube is in thermal equilibrium with its environment ($T_{in} = T_{out} = T$), then using the ideal gas law $p = \rho k_B T/\mu_m$, we have,

$$\rho_{out} = \rho_{in} + \frac{\mu_m B^2}{8\pi k_B T} \qquad \Rightarrow \qquad \frac{\rho_{out} - \rho_{in}}{\rho} = \frac{mu_m B^2}{8\pi k_B T\rho} = \frac{B^2}{8\pi p} \tag{1.4}$$

$$\frac{\Delta\rho}{\rho} = \frac{B^2}{8\pi p} \qquad \Rightarrow \qquad \frac{\Delta\rho}{\rho} = \frac{1}{\beta} \tag{1.5}$$

This implies, that the magnetic flux tube will be less dense than its surrounding environment. In that case buoyant forces will make the magnetic tube move upwards.

If we don't wish to make the assumption that the magnetic tube is in thermal equilibrium with its environment, but at the same time assume that the plasma inside and outside the magnetic tube have the same specific entropy, then the density deficit would be,

$$\frac{\Delta\rho}{\rho} = -\frac{1}{\gamma_1\beta} \tag{1.6}$$

where $\gamma_1 = \left(\frac{\partial \ln p}{\partial \ln \rho}\right)_s$ is Chandrasekhar's first adiabatic index. (Chandrasekhar and Chandrasekhar 1957) Much like in the case of thermal equilibrium, in this case the magnetic flux tube will also rise due to buoyant forces. In order to determine if a flux tube is susceptible to buoyancy forces we can examine the stability of the atmosphere with respect to perturbations.

1.4.1 Stability of the atmosphere to perturbations

As a first example we take the case were the fluid displacement is adiabatic and we also ignore the magnetic field. If the fluid is displaced in an environment with higher pressure the fluid will compress, if on the other hand the environment has a lower pressure it will expand. Using Chandrasekhar's first adiabatic index γ_1 as well as equation (1.5) we can express the change in density of the fluid with the following equation.

$$d\rho_{ad} = \frac{\rho}{p}\gamma_1 \frac{dp}{dz} dz \tag{1.7}$$

However, the density change in the environment will simply be,

$$d\rho = \frac{d\rho}{dz} dz \tag{1.8}$$

This leads us to categorize the different scenarios based on the following relations between the density differentials.

If we have $\frac{\partial \rho_{ad}}{\partial z} > \frac{\partial \rho}{\partial z}$, the buoyancy force will try to cancel the displacement of the fluid, leading it back to its original position. In that case the atmosphere stratification would be considered stable to perturbations. This is the case in the solar photosphere and it can explain why convective currents from the convection zone don't penetrate to higher layers.

If we have $\frac{\partial \rho_{ad}}{\partial z} < \frac{\partial \rho}{\partial z}$, the buoyancy force accelerates the fluid and it moves away from its original position. The two cases that the fluid can move is either to be displaced downward where it would have higher density than the environment or it can be displaced upward where its density would be smaller than that of the surrounding environment. In either case the atmosphere stratification is unstable to perturbations. Such an environment is the solar convection zone and it is the reason why in this layer convective current flows are created.

There is also the marginal case where $\frac{\partial \rho_{ad}}{\partial z} = \frac{\partial \rho}{\partial z}$ that the atmosphere is neutral to perturbations, which implies that any displacement would lead to a new position of equilibrium.

In conclusion, for the solar atmosphere it is very difficult for a fluid element to emerge from the convection zone, which is unstable, to the stable environment of the photosphere. Since the fluid would become much denser than its surrounding, the buoyancy force will make it return to its original position in the convection zone. However when we describe the solar atmosphere more realistically, by adding a magnetic field that interacts with the fluid particles, it becomes possible for the plasma to emerge through the photosphere (M. Cheung and Isobe 2014), (Nordlund, Stein, and Asplund 2009).

1.4.2 Magnetic buoyancy instability

As we mentioned in the previous section, the stability of the photosphere in hydrodynamic perturbations is a major barrier for flux emergence. However when a magnetic field is present, the difficulty with which a plasma element can penetrate the solar atmosphere can improve drastically. Magnetic buoyancy instability is an effective mechanism that allows flux to rise through the photosphere and into the corona.

We can assume the simplest case of horizontal non magnetized tube that is described by the following hydrostatic equation,

$$\frac{d}{dz} p = -g\rho \tag{1.9}$$

In the case of a magnetized flux tube the equation is modified to include the magnetic pressure. The following equation describes a fluid element that is also supported by the magnetic pressure.

$$\frac{d}{dz}\left(p + \frac{B^2}{8\pi}\right) = -g\rho \tag{1.10}$$

Since the magnetic field interacts with the fluid element, the magnetic buoyancy can also act as a mechanism for instability. The different types of instabilities are determined according to the direction of the magnetic field $\mathbf{B}$ in relation to the wave vector of the perturbation $\mathbf{k}$. For the purposes of this work we will consider the cases where the magnetic field and the wave vector are either parallel, $\mathbf{B} \parallel \mathbf{k}$ or perpendicular, $\mathbf{B} \perp \mathbf{k}$ to each other.

The first scenario where the magnetic field and the wave vector are perpendicular $\mathbf{B} \perp \mathbf{k}$, produce the interchange mode. Assuming that the flux sheet before the perturbation is similar to that of Figure(1.4), at the interchange mode in Figure(1.5) the magnetic lines remain straight. The interchange mode can have observational signatures such as sunspots at the solar surface since it is considered a mechanism that can effectively break large magnetic flux sheets, that are formed in the convection zone, into buoyant flux tube that can eventually rise through the photosphere. For the interchange mode the instability criterion as defined by (Acheson 1979) is given by equation (1.11) where there is the assumption of adiabatic perturbations.

$$\frac{d}{dz}\ln\left(\frac{B}{\rho}\right) < -\frac{C_s^2}{g}\frac{N^2}{V_A^2} \tag{1.11}$$

In this expression we have the Alfvén speed $V_A = B/\sqrt{4\pi\rho}$, the adiabatic sound speed $C_s = \sqrt{\gamma_1 p/\rho}$ and the Brunt-Väisälä frequency N. If we focus on the convection zone where the Brunt-Väisälä frequency is $N = 0$, we end up with the following criterion for instability.

$$\frac{d}{dz}\ln\left(\frac{B}{\rho}\right) < 0 \tag{1.12}$$

The other case is when the magnetic field and the wave vector are parallel to each other $\mathbf{B} \parallel \mathbf{k}$, which is called the undular mode. As it is shown in Figure(1.6) the field lines ripple, and since the plasma moves along the magnetic field lines it is forced to move away from the high point, making the cavity lighter which allows it to rise higher. The lower points on the other hand where the plasma concentrates get heavier forcing them to sink lower. This kind of plasma flow can amplify the perturbation making the structure unstable. The undular mode is also refereed to, in bibliography, as Parker instability (Parker 1955). The instability criterion for this mode is given by (Acheson 1979).

$$\frac{d}{dz}\ln B < -\frac{C_s^2}{g}\left(k_\parallel^2(1+\frac{k_z^2}{k_\perp^2}) + \frac{N^2}{V_A^2}\right) \tag{1.13}$$

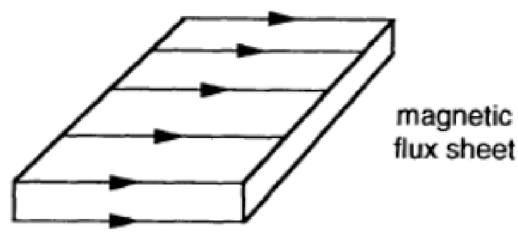

Figure 1.4: Schematic illustration of an undisturbed magnetic flux sheet (Matsumoto et al. 1993).

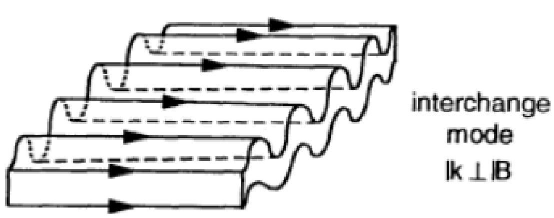

Figure 1.5: Illustration of the flux sheet due to the interchange mode of the magnetic buoyancy instability (Matsumoto et al. 1993).

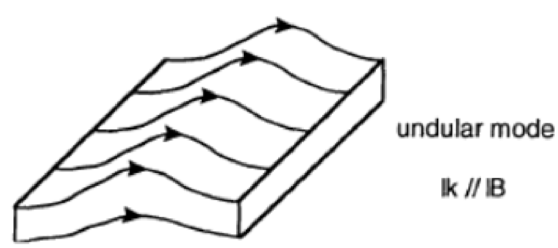

Figure 1.6: Illustration of the flux sheet due to the undular mode of the magnetic buoyancy instability (Matsumoto et al. 1993).

In this expression we have k_z which is the wave number in the vertical direction and $k_\parallel$, $k_\perp$ which are the wave numbers in direction parallel and perpendicular to magnetic field. For $N = 0$ we have,

$$\frac{d}{dz}\ln B < -\frac{C_s^2}{g}k_\parallel^2(1+\frac{k_z^2}{k_\perp^2}) \tag{1.14}$$

which suggests that,

$$-\frac{C_s^2}{g}k_\parallel^2(1+\frac{k_z^2}{k_\perp^2}) \leq 0 \tag{1.15}$$

therefore leaving us with the following inequality for the undular instability.

$$\frac{dB}{dz} < 0 \tag{1.16}$$

At last, by comparing equations (1.11) and (1.15), we conclude that for the undular mode, $\mathbf{B} \parallel \mathbf{k}$, the instability criterion depends on how fast the field strength decreases with height. This is in contrary to the interchange mode, $\mathbf{B} \perp \mathbf{k}$, where the decrease of the fraction B/ρ with height is relevant for the instability. Near the photosphere, B/ρ drops slower than the rate of decrease of the magnetic field B. Therefore the undular mode of the instability ($\mathbf{B} \parallel \mathbf{k}$) dominates this region of the photosphere, and can either be referred to as magnetic buoyancy instability or Parker instability (Matsumoto et al. 1993), (M. Cheung and Isobe 2014).

1.4.3 Magnetic twist

An important physical characteristic of a flux rope is the twist of its magnetic field. Magnetic twist in an emerging flux rope is associated with the free magnetic energy that is responsible for the solar eruptions and flares, so it plays a vital role in flux emergence through the photosphere.
We can assume that we have a cylindrical flux tube, with its magnetic field oriented in the y-axis. We exploit the axial symmetry of the tube to express the magnetic field with the following equations.

$$B_y(r) = B_0 e^{-r^2/R^2} \tag{1.17}$$

$$B_\phi(r) = \alpha r B_0 e^{-r^2/R^2} \tag{1.18}$$

The dimensionless parameter α , measures the number of twists divided by length, r is the distance from the center of the tube and R the tubes radius.
However the twist cannot take any value. If $\alpha > 0.5$, then the tube will be prone to the kink instability. This is because a twist of $\alpha = 0.5$ means that there is a 45 degree angle between B_y and B_ϕ , that will twist the tube in a loop position. If this happens in the deeper areas of the convection zone then the tube will not be able to emerge, unlike the area close to the photosphere where part of the tube will be able to come up.
A useful measure for determining whether a flux tube will be coherent throughout the process of emergence is the magnetic Weber number W_e , an analog of the Weber number in fluid mechanics. This dimensionless number is defined as,

$$W_e = \frac{u^2\rho}{B^2/4\pi} \tag{1.19}$$

where u is the velocity with which the tube rises. For the flux tube to maintain coherence, the magnetic Weber number should be $W_e \lesssim 1$.
Even though the magnetic twist is an important characteristic of flux tubes, it is very difficult to use it to effectively describe a real emerging flux tube. The main reason for that is because it is impossible to observationally measure the distribution of the magnetic field from the photosphere to the corona. So, without the field distribution, we cannot measure the quantities that are related to the twist of an active region. Also solar active regions do not form a simple bipole, and there morphology is often more complex. Because of that a well-defined axis, that is required for the concept of magnetic twist, is not distinguishable. In the following chapter we illustrate a way to deal with these problems with the concept of a force free magnetic field.

1.4.4 Force free magnetic field

A common method that is used to overcome those difficulties is to construct the full 3D coronal field using measurements from vector magnetograms. Afterwards, the magnetic field can be used to calculate the

twist of the field lines.
A force free field is defined as a field where the Lorentz force vanishes everywhere,

$$\frac{1}{c}\; j \times B = 0 \tag{1.20}$$

Along with equation (1.19) we can use the electric current density, taken from Ampere's law,

$$j = \frac{1}{\mu_0}\; \nabla \times B \tag{1.21}$$

and end up with the following equation,

$$(\nabla \times B) \times B = 0 \tag{1.22}$$

Equation (1.21) can be fulfilled either when,

$$\nabla \times B = 0 \tag{1.23}$$

which is called a current free (potential) magnetic field or when,

$$B \parallel \nabla \times B \tag{1.24}$$

The simplest assumption for the coronal magnetic field is the current free field. Using magnetograms the photospheric magnetic field can easily be measured and be used as a boundary condition to solve the Laplace equation for the scalar potential ϕ ,

$$\nabla^2 \phi = 0 \tag{1.25}$$

so the following condition is satisfied,

$$B = -\nabla \phi \tag{1.26}$$

A potential field, due to its simplicity, provides a rough view of a magnetic field in the solar corona. However, the magnetic field at an active region needs to contain free magnetic energy to drive eruptions, a property that a potential field does not have. Hence the condition of force free field can more easily be satisfied.

The $B \parallel \nabla \times B$ condition implies that,

$$\nabla \times B = \alpha B \tag{1.27}$$

which if we use Gauss's law for magnetism, $\nabla B = 0$, can be further expanded to,

$$B \cdot \nabla \alpha = 0 \tag{1.28}$$

Here, α is called the force free parameter where it is constant along magnetic field lines as well as the measure of field line twist. When $\alpha = 0$ it is the current free condition and the field is potential. If α is nonzero, it can either be a a constant or function of position. When α is constant the field is called linear force free field, and when it is a function of position it's called non-linear force free field. In order to accurately quantify the amount of twist of the magnetic field, different values for α have been fitted for different layers of the solar atmosphere. This implies that non-linear force free fields are a better match for consistent modeling of the solar atmosphere.

1.5 Solar eruptive phenomena

In order to better understand the interaction between the solar plasma and the heliosphere, whe have to look at the physical processes which drive powerful solar eruptions. Solar eruptive phenomena like flares and coronal mass ejection (CMEs) which have a great impact on space weather have their origin in the turbulent plasma flows at the solar convection zone that shape the structure and dynamics of the solar atmosphere. Solar active regions (ARs) are the areas of origin of those eruptions that are dynamically and complex (Vasilis Archontis and Vlahos 2019).

1.5.1 Flares

A solar flare is an intense, localized emission of electromagnetic radiation in the Sun's atmosphere. They were first observed in 1959 as localized, minute-long brightening in the continuum of white light (Curto 2020). The energy that is released appears in many forms, such as increase in plasma temperature, acceleration of charged particles, shock waves as well as ejection of material, albeit of significant less quantity than in the case of a CME. Part of the energy causes an increase of electromagnetic radiation in the full spectrum, from gamma rays to radio waves. Typical values of the energy released are at the range of $10^{29} - 10^{32}$erg with each flare event lasting from a few minutes to hours (Steinhilber and Beer 2011). Flares are usually classified based on their flux of X-ray radiation ($1-8$ Å) as it is measured by GOES satellites (Geostationary Orbiting Environmental Satellites). The following table shows the classes (X, M, C, B, A) along with their corresponding approximate peak flux in power per unit square (W/m^2).

	W/m^2
X_{10}	10^{-3}
X	10^{-4}
M	10^{-5}
C	10^{-6}
B	10^{-7}
A	$< 10^{-7}$

Flares usually appear in active regions (ARs) where there is a high concentration of photospheric magnetic field. Those areas in an active region are where there is an inversion of the polarity of the photospheric field's vertical component. The more complex a photospheric magnetic field is, the higher the likelihood of a flare event. The rate of flare occurrence in an active region generally follows the evolution of the active region, so when the AR first appears the chances of a flare increase, especially when the polarity of the emerging flux is opposite to the pre-existing magnetic field. On the other hand during the active region's decay phase, the chance of an eruption decreases.

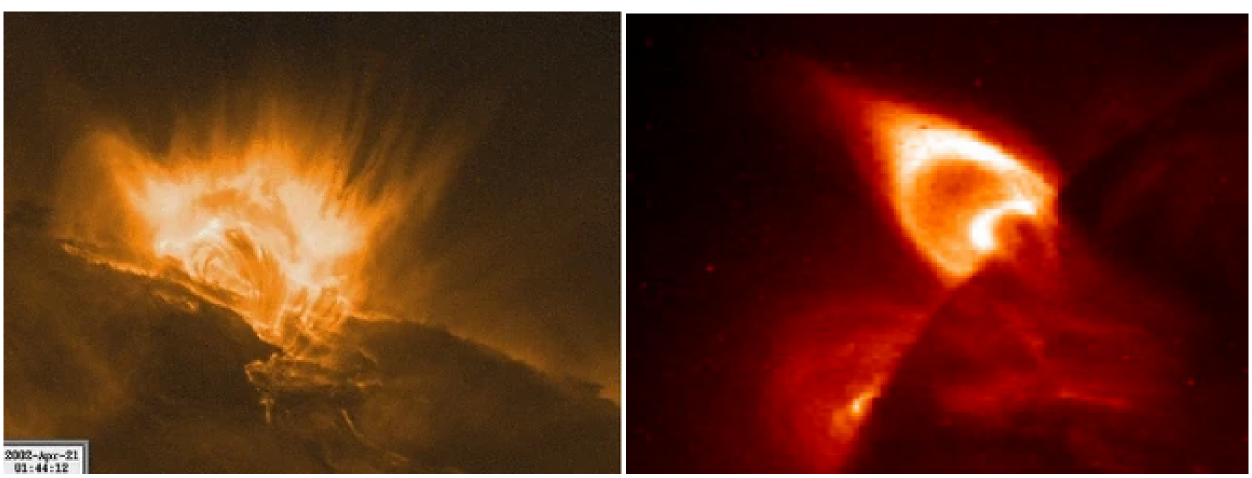

Figure 1.7: Left picture shows the eruptive phase of the SOL2002-04-21 flare observed in the Fexii line at 195 Å by the TRACE satellite (Benz 2017). Right side picture shows a different flare during its decay phase that develops a cusp shape on the top of the loop. It is observed in soft X-rays by the Yohkoh satellite (Αλυσανδράκης, Νίντος, and Πατσουράκος 2016).

The electromagnetic radiation released during a flare can either come from heated plasma (thermal emissions) or from accelerated particles (non-thermal emissions). The time scale of non-thermal emissions is much smaller than that of thermal. This is because accelerated electrons lose their energy through radiation or collision with plasma faster, while heated plasma cools with a slower rate. Either way the flare energy is released in the corona by reconnecting magnetic fields. The energy then propagates from the corona into the dense chromosphere along a magnetic loop. The chromospheric material is heated to an order of 10^7 K and expands into the corona. Before the flaring event occurs, energy is concentrated, which results in an increase of temperature and magnetic field. Afterwards the eruptive phase begins, which allows for the sudden energy release lasting about one minute. Eventually, after the the eruption the flare enters a phase of decay where the solar atmosphere move towards a state of equilibrium. This phase lasts around 20-30 minutes with the temperature of loops steadily decreasing (Αλυσανδράκης, Νίντος, and Πατσουράκος 2016), (Sigalotti and Cruz 2023), (Tandberg-Hanssen and A Gordon Emslie 1988).

An image of a flare during its eruptive phase can be seen in the left side of Figure(1.7). The luminosity peaks when a sheet-like structure appears above the initial brightening. The flare was observed in the Fe xii line at 195 Å by the TRACE satellite. After the time of this image the flare undergoes a long decay phase with post-flare loops growing in height (Benz 2017). Also, it is common for loops to develop a cusp shape on the top side of the loop during the flare's decay phase as seen in the right side of Figure(1.7). In that image, the observation of the flare loop is made in soft X-rays by Yohkoh satellite during its decay phase (Αλυσανδράκης, Νίντος, and Πατσουράκος 2016).

1.5.2 Coronal mass ejection (CME)

The term, coronal mass ejection (CME) refers to the removal of a considerable quantity of coronal plasma, which along with its magnetic field moves away from the Sun and travels through the interplanetary space. CMEs have mass of around $10^{11} - 10^{13}$ kg while reaching speeds of 200 up to 2000 km/sec. CMEs are detected with a coronagraph due to Thomson scattering of photospheric light from the ejected mass electrons.

Figure(1.8) shows a series of pictures of the morphology of a CME. These types of CMEs occur near the solar limb while they exhibit a bright arc-shaped front. Beneath the front there is a dark cavity which is believed to be a magnetic flux rope. There is also a bright core inside this cavity which is plasma from prominence trapped beneath the magnetic field lines and pushed outside during the explosion. Emissions from a CME are optically thin and the dynamic aspects of the phenomenon make it difficult to observe its shape even when two satellites could theoretically create a 3D picture. Assuming a model for the geometry of the CME in 3D as well as a way that it propagates, is the most popular way to recover information about the shape of a CME. When a CME propagates with a speed larger than the local Alfvén speed it creates a shock wave. The shock wave will compress the material in front of it which will appear in a picture from a coronagraph. However, due to low intensity of the brightenings, it is difficult to detect a shock wave that way, so type II radio bursts are a better way for shock detection in front of a CME. On the other hand type II radio bursts do not give any information about the shape of the area where shock waves originate.

When CMEs have their origin near the solar limb, we can categorize them in two different types. The first is a CME that is related with eruptive prominences and isn't accompanied by a flare. They have typical speeds of $\approx$ 400 - 600 km/sec and appear to accelerate in a coronagraph. There are also CMEs that are associated with flares and have speeds larger than 750 km/sec while they seem to decelerate in a coronagraph's optical field. The later type of CME usually has three stages for their speed evolution. Before the beginning of the flare, the CME rises slowly for minutes. Then during the eruptive stage where a CME experiences rapid acceleration, for a maximum of 10 minutes, while it is also at the same time that the flare's flux peaks. This apparent coincident can be explained by the fact that magnetic reconnection that happens in a current sheet behind the CME, can add new flux that will accelerate it. This means that the bigger the magnetic reconnection rate is, the more energy the flare will release, which will also have an impact on the acceleration of the CME. In the end the CME moves with an either steady or slightly decreasing speed.

Since coronagraphs hide the solar disk, the area of origin of the CMEs has to be identified with other instruments. For this reason space telescopes observe the corona in far infrared and soft X-rays, along with telescopes from earth that observe in the chromospheric H_α line and radio telescopes, can provide important information about CMEs. We have already established that flares occur exclusively on active regions (ARs), this however is not the case for CMEs. So CMEs may or may not be related to flares, even though there is a corelation between strong flares such as X-type and CME events. More than half of the CMEs are related with filament eruptions. Filaments are not necessarily in an AR and when they erupt they almost always create a CME. Filament eruptions outside of ARs have characteristics that are similar to those of flares such as loops. However, from an observational point of view filament eruptions outside of ARs do not emit radiation in the soft X-rays regime because those areas have a weaker magnetic field than that of the active region's. Nevertheless, observations at the EUV shows dark regions that are due to the density deficit from the ejected mass. Regardless of which area CMEs originate, the magnetic field must always be twisted.

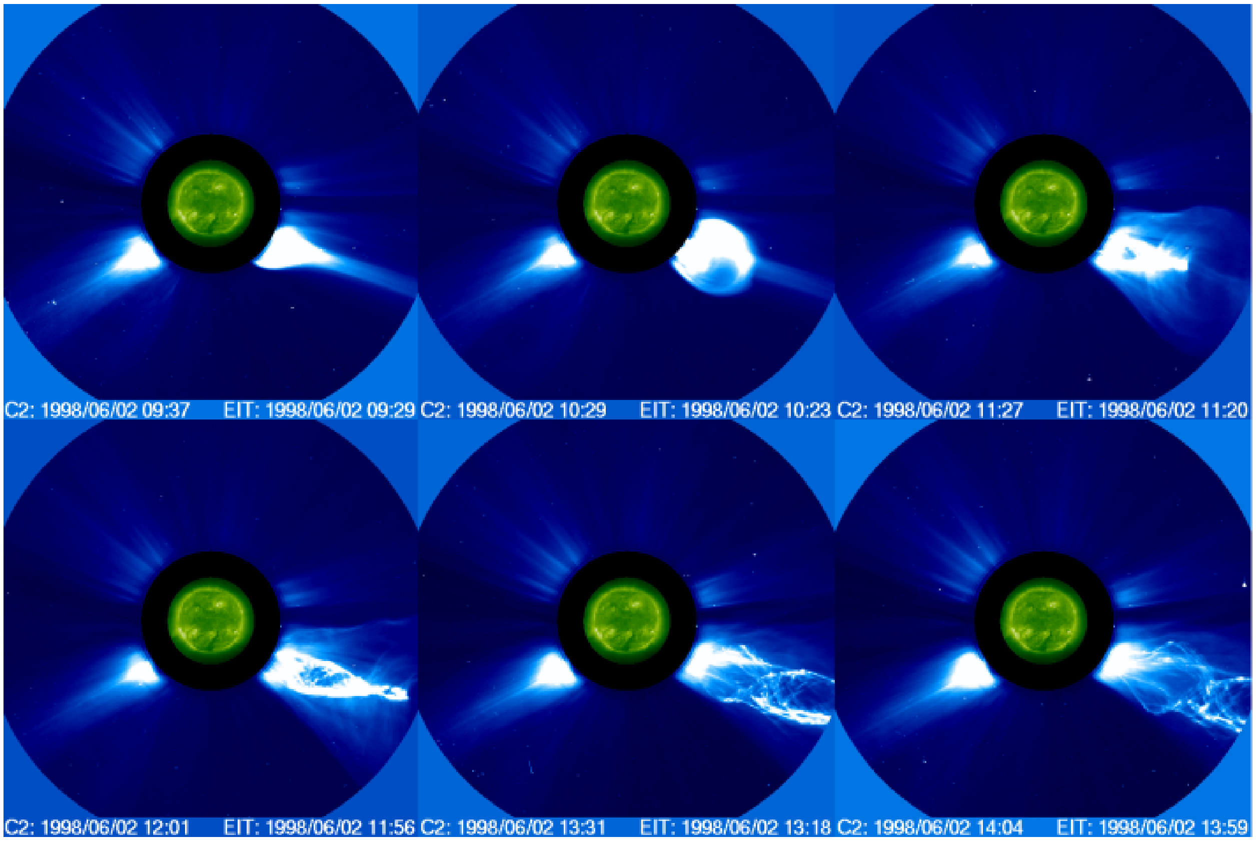

Figure 1.8: CME observation (Αλυσανδράκης, Νίντος, and Πατσουράκος 2016).

This is evident in the case of a CME being accompanied by a flare since flares occur near the polarity inversion line of the magnetic field, where on top of it there is a high concentration of electric currents. On the other hand, along the axis of filaments the orientation of small structures also points towards a twisted magnetic field (Αλυσανδράκης, Νίντος, and Πατσουράκος 2016),(Chen 2011), (Jacobs and Poedts 2011).

1.5.3 Flare - CME standard model

In order to explain the observations of large flares that are accompanied by CMEs, the Flare - CME standard model was developed (Carmichael 1964), (P. Sturrock 1966), (Hirayama 1974), (Kopp and Pneuman 1976). This model assumes a twisted magnetic field such as a magnetic flux rope, which is part of a structure containing arch-like loops. Due to instability, the flux rope ascents causing the surrounding field lines to stretch and become antiparallel to each other. The more the field lines stretch the closer they come eventually creating a current sheet. Instabilities inside the current sheet trigger magnetic reconnection which then creates a flare at the bottom part of the reconnection region. The topology of the magnetic field lines is rearranged which allows the flux rope to escape the main structure. In observations the height increase of the reconnection region is shown by the apparent upward movement of the hot loops. In Figure(1.9) there is a cartoon of that model (Lin and Forbes 2000).

The success of this model is reflected in the fact that it can explain observations of flares with long decay state. It also accounts for the timing between the acceleration of a CME and the flux variations of the accompanied flare. The hard X-ray emission above the hot loops can also be explained by the model. The main downside of this model is the fact that it is two dimensional, which means that its magnetic topology is that of a dipole, while it is known that in the Sun most flare occur in regions with complex magnetic topology.

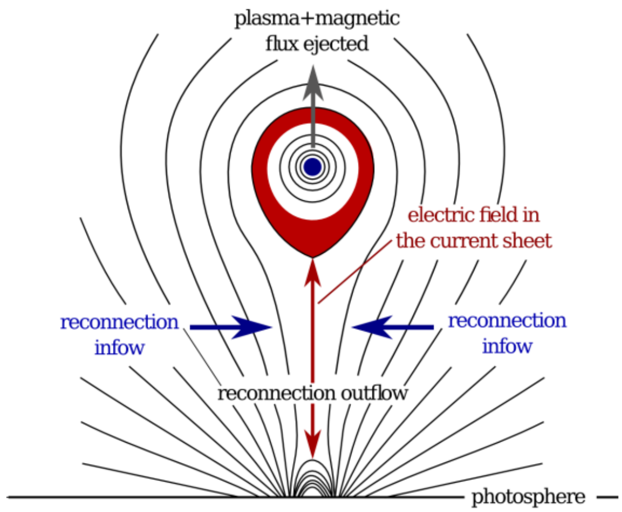

Figure 1.9: Cartoon of the Flare-CME model (Lin and Forbes 2000).

Another important drawback is the size of the current sheet. For the model to be realistic in providing the right amount of accelerated particle, the main dimensions of the current sheet has to be in the orders of magnitude of thousands of Mm and at the same time to be stable for many minutes. It is very to difficult to maintain such a large structure inside an already unstable magnetic topology and it is more likely that the current sheet will be fragmented into smaller structures (Α$\lambda\upsilon\sigma\alpha\nu\delta\rho\acute{\alpha}\kappa\eta\varsigma$, Ν$\acute{\iota}\nu\tau$ος, and Π$\alpha\tau\sigma o\upsilon\rho\acute{\alpha}\kappa$ος 2016).

Magnetohydrodynamics

2.1 Introduction

In this chapter we will make an introduction and description of Magnetohydrodynamics (MHD). This is very important because in the present thesis every calculation and analysis has been done under the assumptions of MHD. Magnetohydrodynamics is a model that treats the plasma as a continuous electrically conducting fluid. As the name suggests a pure hydrodynamical treatment of the fluid is not enough and the electromagnetic interactions between the fluid particles have to be taken into account. That is why we will mention Maxwell's equations as well as fluid mechanics equations in order to adequately describe the dynamics of solar plasma.

2.2 Maxwell's equations

Electromagnetic fields are described by Maxwell's equations which are presented in the following section. Gauss's law,

$$\nabla \cdot E = \frac{\rho}{\epsilon_0} \tag{2.1}$$

Gauss's law of magnetism,

$$\nabla \cdot B = 0 \tag{2.2}$$

Faraday's law,

$$\nabla \times E = -\frac{\partial B}{\partial t} \tag{2.3}$$

Ampére's law,

$$\nabla \times B = \mu_0 j + \epsilon_0 \mu_0 \frac{\partial E}{\partial t}. \tag{2.4}$$

As well as Ohm's law,

$$j = \sigma(\ E + u \times B\ ) \tag{2.5}$$

Here, ρ is the density charge, σ the electrical conductivity and u is the plasma speed. While ϵ_0 and μ_0 are vacuum's permittivity and vacuum's magnetic permeability respectively. Those last two parameter are associated with the speed of light as, $c = \frac{1}{\sqrt{\epsilon_0 \mu_0}}$.
A crucial assumption in MHD is that the plasma fluid moves as a whole with a single velocity u. This speed is considered to be much smaller than the speed of light $u << c$. Hence, Ampére's law takes the simpler form,

$$\nabla \times B = \mu_0 j \tag{2.6}$$

Also, Gauss's law from equation (2.1) has zero density charge because plasma is considered to be quasi-neutral in scales larger than Debye length. Meaning that the number of electrons n_e is approximately equal to the number of ions n_i , and since they have equal charge of opposite signs, charge density is approximately zero $\rho \simeq 0$. Debye length is expressed by the following equation,

$$\lambda_D = \sqrt{\frac{\epsilon_0 k T}{n e^2}} \tag{2.7}$$

For solar plasma Debye length is roughly $\lambda_D \simeq 0,2$ cm.

An assumption that simplifies the analysis would be that the plasma is a perfect conductor with zero resistivity. This is known as ideal MHD where the magnetic field looks like it's "frozen" in the plasma. For ideal MHD to hold, the plasma particles have to be collisional and follow a Maxwellian distribution. Even if the plasma has a finite resistivity we can still apply MHD to describe important astrophysical phenomena such as magnetic reconnection. Under the assumption of ideal MHD where electric conductivity is $\sigma \to \infty$, Ohm's law takes the form of equation (2.8).

$$j = \sigma(\ E + u \times B\ ) \quad \Rightarrow \quad (\ E + u \times B\ ) = \frac{j}{\sigma} = 0$$

$$E = -u \times B \tag{2.8}$$

Electric conductivity σ relates to magnetic resistivity η as,

$$\eta = \frac{1}{\mu_0 \sigma} \tag{2.9}$$

So, for ideal MHD instead of electric conductivity $\sigma \to \infty$ equivalently we can use the magnetic resistivity $\eta = 0$.

2.3 Induction equation

In order to fully plasma motion we combine Maxwell's equations and Ohm's law, and derive the induction equation,

$$\frac{\partial B}{\partial t} = \nabla \times (u \times B) - \nabla \times (\eta \nabla \times B) \tag{2.10}$$

This equation shows that the evolution of the magnetic field is a result of both the fluid motion as well as it's diffusion. The terms of the induction equation (2.10) that are responsible for plasma motion and diffusion are shown as,

$$\nabla \times (u \times B) \qquad [\text{ Kinetic term }]$$

$$\nabla \times (\eta \nabla \times B) \qquad [\text{ Diffusion term }]$$

The ratio of those two terms define the magnetic Reynolds number which is an important dimensionless quantity that indicates whether diffusion or kinetic effects dominate the time evolution of the magnetic field. The definition of the magnetic Reynolds number is,

$$R_m = \frac{L_0 u_0}{\eta} \tag{2.11}$$

where L_0 is the characteristic length scale and u_0 the plasma velocity. We can distinguish two common scenarios for R_m

If $R_m << 1$ then the magnetic resistivity η in the denominator of equation (2.11) is large relative to the length scale and the plasma velocity so the evolution of the magnetic field is dominated by the diffusion of the field. This leads to the induction equation being rewritten as,

$$\frac{\partial B}{\partial t} = -\nabla \times (\eta \nabla \times B) \tag{2.12}$$

we can further simplify this equation by using the vector identity,

$$\nabla \times (\nabla \times B) = \nabla(\nabla \cdot B) - (\nabla \cdot \nabla)B \tag{2.13}$$

At last, the induction equation when the diffusion term dominates ($R_m << 1$) is,

$$\frac{\partial B}{\partial t} = \eta \nabla^2 B \tag{2.14}$$

If $R_m >> 1$ then this means that the length scale is much larger than the value of magnetic diffusion η , so the kinetic term dominates, and the induction equation is simplified as,

$$\frac{\partial B}{\partial t} = \nabla \times (u \times B) \tag{2.15}$$

This is largely the case for plasma at the solar corona where the magnetic Reynolds number has values in the range of $R_m \approx 10^8 - 10^{12}$.

2.4 Magnetic flux

Firstly, we should describe an important quantity for energy transfer in the electromagnetic field which is the Poynting flux. The Poynting flux is defined as the flux of electromagnetic energy that passes through a unit area per unit time,

$$S = \frac{1}{\mu_0} E \times B \tag{2.16}$$

The units are [W/m^2] . If we use Ohm's law from equation (2.5) then the Poynting flux can be written as,

$$S = \eta(j \times B) - \frac{1}{\mu_0}(u \times B) \times B \tag{2.17}$$

The two different terms on this equation express the interaction of currents and plasma with the magnetic field as shown,

$$j \times B \qquad \text{[Interaction of currents with magnetic field]} \tag{2.18}$$

$$(u \times B) \times B \qquad \text{[Interaction of plasma flows with magnetic field]} \tag{2.19}$$

Another important quantity is the magnetic energy density that is defined as,

$$\varepsilon_m = \frac{B^2}{2\mu_0} \tag{2.20}$$

In order to describe how magnetic energy changes form we take the time derivative of the magnetic energy density (2.20)

$$\frac{\partial \varepsilon_m}{\partial t} = \frac{1}{\mu_0} B \cdot \frac{\partial}{\partial t} B \tag{2.21}$$

From that, the term $\partial B/\partial t$ is substituted with the induction equation (2.10),

$$\frac{\partial \varepsilon_m}{\partial t} = \frac{1}{\mu_0} B \left[\nabla \times (u \times B) - \nabla \times (\eta \nabla \times B) \right] \tag{2.22}$$

The definition of Poynting flux (2.16) as well as Ampére's law (2.4) are substituted in equation (2.22) to obtain the final result.

$$\frac{\partial \varepsilon_m}{\partial t} + \nabla \cdot S = -\eta \mu_0 j^2 - u \cdot (j \times B) \tag{2.23}$$

When the right hand side of this equation is zero, it would mean that the magnetic energy is conserved and there is no loss of energy. In the more general case we have two more terms on the right hand side of equation (2.23) that describes the conversion of magnetic energy into other forms of energy as shown,

$$\eta \mu_0 j^2 \qquad \text{[Magnetic energy converts to thermal energy]} \tag{2.24}$$

$$u \cdot (j \times B) \qquad \text{[Magnetic energy converts to kinetic energy]} \tag{2.25}$$

In the case of a large magnetic Reynolds number ($R_m >> 1$) , we can consider a closed loop that encompasses a small fluid element. This loop will move along the fluid while it changes it's shape and size.

Now, the magnetic flux of this loop can be defined as as the total number of field lines that pass through it. So, if we consider the surface α that is enclosed by the loop, the magnetic flux would be,

$$\Phi = \int_{\alpha} B \cdot dA \tag{2.26}$$

where we denote, $dA = n \cdot d\alpha$, with $d\alpha$ an element of surface α and n a vector perpendicular to α. According to Alfvéns theorem for a perfectly conducting fluid where equation (2.15) holds due to a large magnetic Reynolds number, the magnetic flux of equation (2.26) remains constant over time.

$$\frac{d\Phi}{dt} = 0 \tag{2.27}$$

This is called "frozen in" condition. This condition implies that a plasma element that is on a magnetic field line, will remain on that line over time. So, for ($R_m >> 1$) the amount of energy that is transported is much larger than that being diffused meaning that the magnetic field will dominate and plasma will move along the magnetic field lines. This condition is of major significance since it explains why a plasma element that moves along a magnetic loop will stay on that loop. In the case of magnetic reconnection, which is common during eruptions, the "frozen in" condition does not hold and the diffusion term in the induction equation (2.10) dominates.

In the solar corona the magnetic Reynolds number is very large, so we can apply the "frozen in" condition. However if two magnetic structures come very close to each other, then strong current sheets will be created where the magnetic field will diffuse. In that case the induction equation will include the diffusion term $\nabla \times (\eta \nabla \times B)$ as it is shown in equation (2.10).

2.5 Fluid equations

In order to describe the dynamical evolution of the plasma we can use Newton's second law of motion, modified specifically for a conducting fluid that the Lorentz force acts on it. For the general case we have to take into account other forces such as gravity and the viscosity. So we can write the general expression for all the forces that act on a fluid element as,

$$\rho \frac{Du}{Dt} = \sum_i f_i \tag{2.28}$$

where ρ is the plasma density, f_i are all the forces and D/Dt is the Lagrangian derivative,

$$\frac{D}{Dt} \equiv \frac{\partial}{\partial t} + u \cdot \nabla \tag{2.29}$$

More precisely the equation that describes the motion of plasma under forces that are common in the solar atmosphere is:

$$\rho \left(\frac{\partial u}{\partial t} + (u \cdot \nabla) u \right) = -\nabla P + j \times B + \rho \nabla \Phi_g + F_\nu \tag{2.30}$$

Here, the forces are on the right hand side of the equation and. For this study we ignore forces that arise from the rotation of the Sun such as centrifugal and Coriolis forces and we only take into account the following:

$$-\nabla P \tag{2.31}$$

This is the pressure gradient and it describes the force that arises from pressure difference.

$$j \times B \tag{2.32}$$

The Lorentz force. This force can be expanded into two terms that describe the magnetic pressure (2.31) and the magnetic tension (2.32)

$$\nabla \left(\frac{B^2}{2\mu_0} \right) \qquad [\text{ Magnetic pressure }] \tag{2.33}$$

$$\left(B \cdot \nabla\right) B/\mu_0 \qquad [\text{ Magnetic tension }] \tag{2.34}$$

The magnetic pressure on one hand tries to balance the different pressure forces inside the plasma, while the magnetic tension tends to minimize the curvature of the magnetic field lines.

$$\rho \nabla \Phi_g \tag{2.35}$$

This is the gravity force that is described by the gravity potential Φ_g . A common expression used for the potential is $\nabla \Phi_g = g\hat{z}$.

$$F_\nu \tag{2.36}$$

Lastly we have the viscous force. In non ideal fluids, due to friction a fluid element that moves with higher velocity than the element next to it will transfer an amount of its momentum to the area with the smaller velocity fluid. The viscous force has a general expression of,

$$F_\nu = 2\nu S \nabla \rho \tag{2.37}$$

where ν is the viscosity and S the strain tensor.

Another important equation is the continuity equation. For the MHD model plasma is considered to be a quasi-neutral magnetised fluid. So like any fluid the mass density is a conserved quantity that is described by the continuity equation.

$$\frac{\partial \rho}{\partial t} + \nabla \cdot (\rho u) = 0 \tag{2.38}$$

Here ρ is the mass density and u the plasma velocity. An equivalent definition can be obtained using the Lagrangian derivative.

$$\frac{D\rho}{Dt} + \rho \nabla \cdot u = 0 \tag{2.39}$$

From equation (2.37) we can understand that a density increase in a region of space is accompanied by a flow that leads plasma away from that region. Identically a density decrease means that plasma will flow into the region. If we assume an incompressible flow ($\nabla \cdot u = 0$) then

$$\frac{D\rho}{Dt} = 0 \quad \Rightarrow \quad \frac{\partial \rho}{\partial t} + u \nabla \cdot \rho = 0 \tag{2.40}$$

To fully describe plasma, since it's ionized gas, we need an equation of state. For the description of astrophysical plasma with MHD it is common to use the equation of state of ideal an gas.

$$p = \frac{k_B}{\mu_m} \rho T \tag{2.41}$$

In this equation that links pressure (p) with temperature (T) we denote k_B the Boltzmann constant and $\mu_m = \bar{m} m_p$ the reduced mass. m_p is the proton's mass and $\bar{m}$ the degree of ionization. In the solar corona we have a fully ionized hydrogen plasma so there is the same amount of protons and electrons. So we have $\bar{m} = 0.5$. For the density ρ we have

$$\rho = n_p m_p + n_e m_e \approx n_e m_p$$

where

$$n = n_p + n_e = 2n_e$$

Finally, we need one more equation to accurately describe the plasma evolution in MHD. The energy equation. For solar corona plasma, which is fully ionized, the energy equation is,

$$\epsilon = \frac{p}{\rho(\gamma - 1)} \quad = \quad \frac{k_B T}{\mu_m(\gamma - 1)} \tag{2.42}$$

The above equation is adequate for the current work. However if we would like to have a complete description of the energy balance in the solar atmosphere, we can write the energy equation as the change of energy in the system along with energy terms that represents loss or transfer of energy.

$$\rho \frac{D\epsilon}{Dt} + p\nabla \cdot u = Q_{heating} + Q_{viscous} + Q_{conduction} + Q_{radiation} \tag{2.43}$$

The terms on the right hand side of equation (2.42) describe,

$$Q_{heating} = \eta \mu_0 j^2 \qquad \text{[Ohmic heating term]}$$

the Ohmic heating of plasma (Joule heating) which happens due to its electrical resistance.

$$Q_{viscous} = 2\nu \rho S^2 \qquad \text{[Viscous term]}$$

Here, the viscosity of the plasma creates friction which in turn converts kinetic energy into heat.

$$Q_{conduction} = -\nabla \cdot q \qquad \text{[Conduction term]}$$

This term represents the energy loss due to thermal conduction. Heat flux because of thermal conductivity is denoted by $q = -\kappa \nabla T$ where κ is the thermal conduction tensor.

$$Q_{radiation} = n_e n_H Q(T) \qquad \text{[Radiative cooling term]}$$

At last we have losses due to radiative cooling. The above equation hold only for optically thin emissions like in the solar corona. The $Q(T)$ function expresses the plasma emissivity which is the ability of a plasma element to emit radiation due to its temperature. A common choice for the $Q(T)$ function is

$$Q(T) = n_e^2 \; \chi \; T^{\alpha}$$

where χ and α are constants with different values at different temperature ranges. If the solar environment is not optically thin then $Q(T)$ takes a different form and is obtained by solving the equation of radiative transfer. Radiative cooling is of significant importance at the lower and denser parts of the corona and transition region (Goedbloed and Poedts 2004).

2.6 Magnetic reconnection

A very common process in the solar atmosphere is that of magnetic reconnection. By that we refer to a change in the topology of the magnetic field configuration when field lines interact at a small distance. Magnetic reconnection occurs in almost ideal plasma where the magnetic Reynolds number is much larger than unity, $R_m \gg 1$. Plasma elements maintain their configurations under ideal magnetohydrodynamics. However, when diffusion exist in a small region, this can affect the way plasma elements are connected. Magnetic reconnection has many results such as converting magnetic energy into heat by the means of Ohmic dissipation, convert magnetic energy to kinetic energy which results in the acceleration of plasma or create shock waves which are associated with strong electric fields and produce accelerated fast particles. Overall the field configuration changes and the newly formed magnetic field lines redirect plasma at different paths. In the Sun, magnetic reconnection plays an important role in the creation of solar flares and can potentially contribute in the heating of the corona.

Since ideal MHD do not apply during reconnection, the plasma must have a nonzero magnetic resistivity $\eta \neq 0$, which will result in the diffusion of the magnetic field to be considerable. We can provide an adequate description of reconnection in 2D with Figure(2.1) showing how magnetic field lines reconnect and how the topology of the field changes.

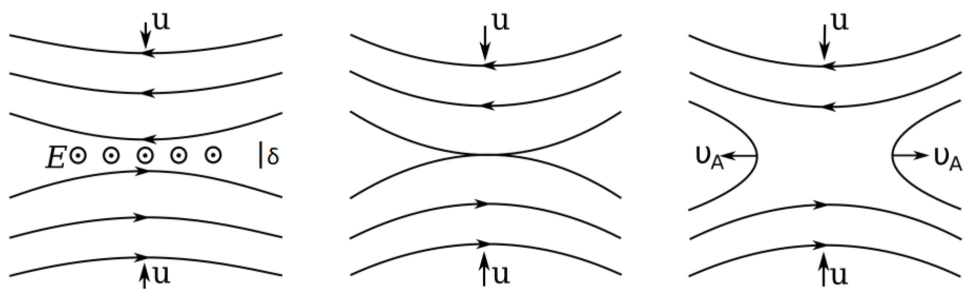

Figure 2.1: Progression of magnetic reconnection as the field lines move closer to each other (Αλυσανδράκης, Νίντος, and Πατσουράκος 2016).

We can see in the picture we have field lines of opposite direction. As plasma flows pushes the field lines towards the neutral line, which divides regions of magnetic fields with opposite polarities, a topology that looks like an $x-$point is formed. The more the field lines move closer to each other, current density increases which makes the resistivity to have a finite value. In that region the field lines are no longer "frozen in" and the plasma diffuses. When the field lines eventually touch, the magnetic tension will pull the newly connected lines away from the diffusion region. In the case of 2D reconnection the only place where the magnetic field lines can be directed is on the sides of the diffusion region as shown in Figure(2.1). So, magnetic energy that flows into the diffusion region is transformed to kinetic energy that flows out of the region.

2.6.1 Sweet-Parker model

We will present two different approaches to magnetic reconnection. The first one is the Sweet-Parker model which describes slow reconnection. An illustration of the diffusion region of this model is shown in Figure(2.2). We see that the region has a length of $2L$ and width of 2δ were $L \gg \delta$.

First, we have to assume that the flow is incompressable, which means that $\rho_{in} = \rho_{out} = \rho$, and by also assuming steady state we get from mass conservation,

$$u_{in}L = u_{out}\delta \tag{2.44}$$

Afterwards, we equate the kinetic energy that plasma gains with the electromagnetic energy that flows into the region, which is the Poynting vector.

$$\frac{1}{2}\rho u_{in}(u_{out}^2 - u_{in}^2) = \frac{u_{in}B_{in}^2}{4\pi} \tag{2.45}$$

Then, since $L \gg \delta$, by using equation (2.44) we have $u_{out} \gg u_{in}$, which in turns gives us the following relation for outflow speed,

$$u_{out}^2 = 2u_{A,in}^2 \tag{2.46}$$

where $u_{A,in}$ is the Alfvén speed in the inflow region.

In order to calculate the inflow speed we first need to obtain a relation for the thickness of the outflow region δ. By combining Ohm's and Amperé's laws we get,

$$\delta = \frac{\eta c^2}{4\pi u_{in}} \tag{2.47}$$

which in turn is used alongside equations (2.44) and (2.46) to get the inflow speed,

$$u_{in}^2 = \frac{\sqrt{2}\eta c^2}{4\pi L}u_{A,in} \tag{2.48}$$

Now, we can see that the magnetic Reynolds number that is associated with the Alfvén speed at the inflow region is,

$$R_{m,A,in} = \frac{4\pi u_{A,in}L}{\eta c^2} \tag{2.49}$$

and we have the inflow speed expressed as,

$$u_{in} = u_{A,in}\sqrt{\frac{\sqrt{2}}{R_{m,A,in}}} \tag{2.50}$$

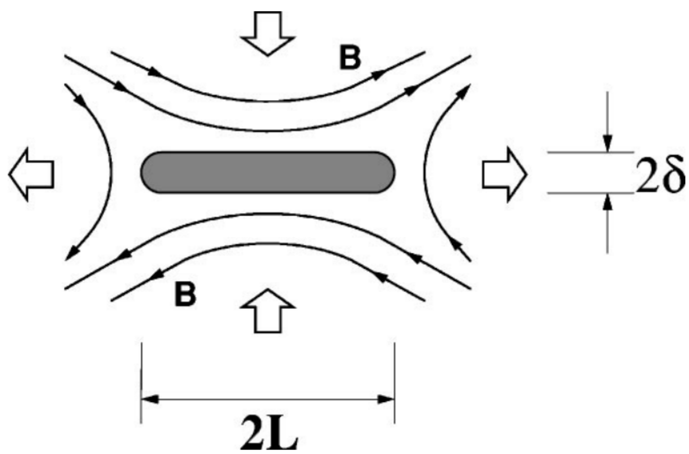

Figure 2.2: Diffusion region at the Sweet-Parker model (Ji et al. 1999).

We can quantify how fast reconnection occurs with reconnection rate r which is generally expressed as,

$$r = \frac{\text{inflow speed}}{\text{outflow speed}} \tag{2.51}$$

for the Sweet-Parker model, equations (2.46) and (2.50) gives as a reconnection rate of,

$$r \sim \frac{1}{\sqrt{R_{m,A,in}}} \tag{2.52}$$

The reason why the Sweet-Parker model describes slow reconnection is because if we use realistic values of the magnetic Reynolds number for the solar corona, which is in a range of $R_m \approx 10^8 - 10^{12}$, we will have a reconnection rate of $r \approx 10^{-4} - 10^{-6}$. This is in fact very slow for phenomena that are due to reconnection. For example solar flares would have a timescale of days while in reality they have a timescale of a few minutes (Αλυσανδράκης, Νίντος, and Πατσουράκος 2016) , (Shibata and Magara 2011).

2.6.2 Petschek model

Since the previously discussed model is not consistent with observations we have to find a way to increase the reconnection rate. In order to achieve that we have to take a closer look at equation (2.49) which the reconnection rate r depends on. To achieve that we can decrease the scale of the reconnection region L which will reduce the magnetic Reynolds number $R_{m,A,in}$. Other solutions are also possible such as increasing the plasma resistivity. This incident is called anomalous resistivity and can occur when there are ion-acoustic waves on the plasma, however we will not discuss it more extensively.

A popular model that reduces the scale of the reconnection region is the Petschek model and its smaller diffusion region is illustrated on Figure(2.3). In reality the decrease of scale L happens due to shock waves that are developed between the inflow and the outflow region. Because of the shock waves, the inflow speed can increase significantly compared to the Sweet-Parker model, allowing for a faster reconnection rate. For the Petschek model the reconnection rate is given by,

$$r \approx \frac{\pi}{8 \ln R_m} \tag{2.53}$$

Using a typical value of the magnetic Reynolds number for the solar corona $R_m \approx 10^8 - 10^{12}$, we get values in the range of $r \approx 0.01 - 0.02$ for the reconnection rate according to the Petschek model. This is a significant improvement regarding observations of dynamic phenomena.

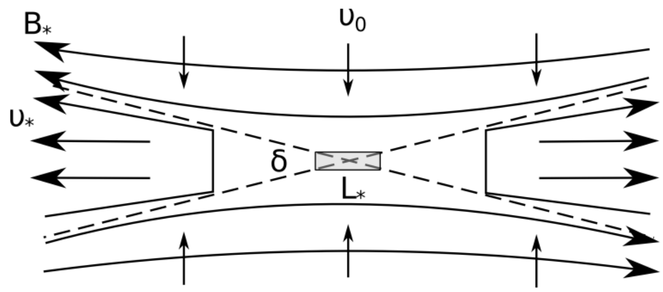

Figure 2.3: Diffusion region at the Petschek model (Αλυσανδράκης, Νίντος, and Πατσουράκος 2016)

2.6.3 3D reconnection

The analysis we presented earlier holds for 3D configurations only under the assumption that the magnetic field is symmetric in the third direction. Since this is not the general case, by adding a third dimension we also introduce certain characteristics that are different from the two dimension case. Some of the most distinctive aspects of the new magnetic configuration are null point, separatrix surfaces and separators. Null points are the points where the magnetic field is zero. Field lines that pierce through an area such as the photosphere enclose a volume. Different volumes may exist since filed lines enter and exit the photosphere at different areas. The boundary that separates those different volumes is called separatrix surface. This means that a separatrix surface connects places where the magnetic field penetrates the photosphere and a null point. Separators are field lines that connect two different null points and are the intersection between two separatrix surfaces.

These characteristics are illustrated in Figure(2.4) where we have the field lines of a quadrupole magnetic field. This is a realistic scenario that can happen when a bipolar region emerges next to an already existing bipolar region.

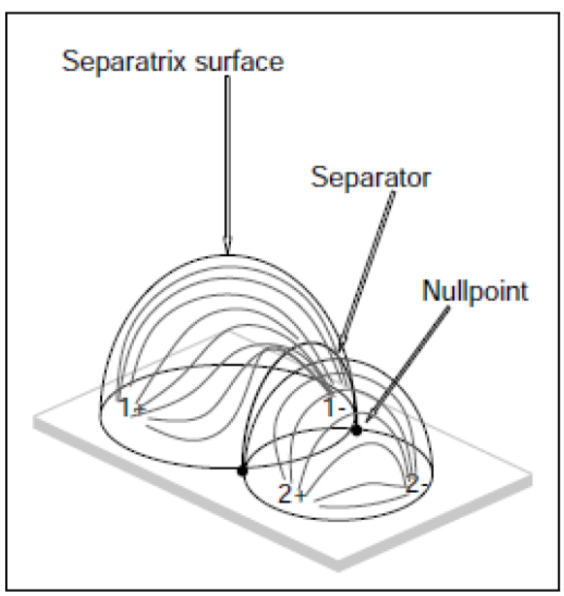

Figure 2.4: Magnetic field topology of a quadrupole region with null points, separators and separatrix surfaces (Αλυσανδράκης, Νίντος, and Πατσουράκος 2016).

Just like in the 2D case, the presence of currents is also necessary for reconnection in 3D. This can be explained by the necessary and sufficient condition for magnetic reconnection which is given by the following equation.

$$\int_{dl} E_{\parallel} \; dl \neq 0 \tag{2.54}$$

where dl is the path through a filed line's length, and $E_{\parallel}$ is the component of the electric field that is parallel to the magnetic field line. In 3-dimensions, reconnection doesn't only occur when the magnetic field develops an x-point as it does in 2D, instead there are several other types of 3D magnetic reconnection.

A convenient example is that of separator reconnection that is the 3D analogue of x-point reconnection in 2D. A section perpendicular to the separator will reveal an x-point type structure, where the main component of the magnetic field is parallel to the separator.

In any case where there is 3D reconnection, magnetic field lines diffuse throughout the whole volume of the diffusion region, so any part of the line that goes through that volume will reconnect with some other field line. Due to that behavior it is difficult to find pairs of field lines that after reconnection form other pairs such as in 2D reconnection. Instead we can have pairs of field line volumes that create new volumes after reconnection. The difference between the lines in 2D and the volumes in 3D can be seen in the left and right side of Figure(2.5) respectively.

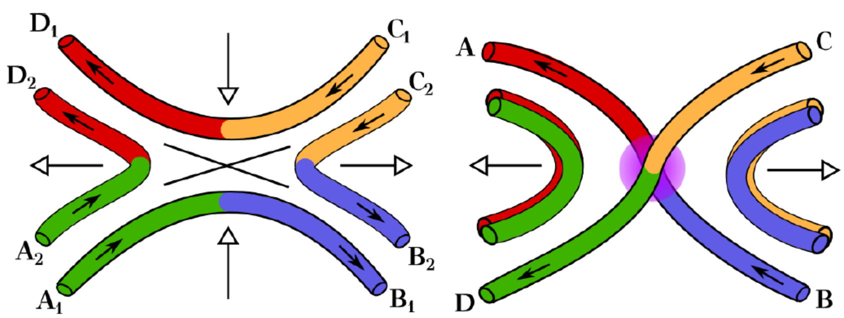

Figure 2.5: Sketches of magnetic reconnection in 2D (left) and 3D (right). Colored tubes correspond to magnetic flux tubes and the purple sphere is the volume of the diffusion region (Α$\lambda\upsilon\sigma\alpha\nu\delta\rho\acute{\alpha}\kappa\eta\varsigma$, Ν$\acute{\iota}\nu\tau$ος, and Π$\alpha\tau\sigma o\upsilon\rho\acute{\alpha}\kappa$ος 2016).

Lare3D Code

3.1 Introduction

The analysis we present in the current work is done by using numerical simulations. To do so we use LareXd which are Lagrangian remap codes for solving MHD equations in 3 dimensions ($3D$). This LareXd code solves the nonlinear MHD equations for know known viscosity and resistivity. Extensions may include gravity term, a partially ionized hydrogen equation of state, Cowling resistivity, parallel thermal conductivity and optically thin radiative losses.

To solve the set of equations it splits each time step into a Lagrangian step followed by a remap onto the original grid. This is the reason why adding additional physical properties is very convenient since it allows all properties into a single Lagrangian step. The remap step has gradient limiters for the correct inclusion of shocks.

The code uses an evenly spaced grid to built conservation laws into the finite difference scheme. The program can be implemented to execute in parallel and it can scale linearly. A more detailed explanation about the equation that it solves and how it solves them will be expanded in the following sections (TD Arber, Longbottom, et al. 2001).

3.2 MHD Equations

Here we concentrate on the standard resistive MHD equations in S.I. units.

$$\frac{\partial \rho}{\partial t} = -\nabla \cdot (\rho u) \tag{3.1}$$

$$\frac{Du}{Dt} = \frac{1}{\rho} j \times B - \frac{1}{\rho} - \nabla p \tag{3.2}$$

$$\frac{\partial B}{\partial t} = -\nabla \times E \tag{3.3}$$

$$\frac{\partial \varepsilon}{\partial t} = -\frac{p}{\rho} \nabla u + \frac{\eta}{\rho} j^2 \tag{3.4}$$

$$E + u \times B = \eta j \tag{3.5}$$

$$\nabla \times B = \mu_0 j \tag{3.6}$$

The symbols in the above equations have the following meaning. E and B are the electric and magnetic field respectively. ρ the plasma density, p the pressure, j the current density and u the plasma velocity. We also note the meaning of η which is the resistivity, which is linked with the conductivity as, $\eta = \frac{1}{\sigma}$. By setting the resistivity to zero, $\eta = 0$, we have ideal MHD. Equation (3.4) is expressed in terms of the specific internal energy density ε. Even though in numerical calculations this is a more useful definition, it might be easier to understand the physical properties of the system if instead of ε we use the temperature (T) and pressure (p). Those quantities are connected with the following equations.

$$\varepsilon = \frac{p}{\rho(\gamma - 1)} = \frac{k_B T}{\mu_m(\gamma - 1)} \tag{3.7}$$

$$p = \frac{\rho k_B T}{\mu_m} \tag{3.8}$$

Since μ_m is the reduced mass, for neutral hydrogen atoms we have $\mu_m = m_p$ and for fully ionized hydrogen $\mu_m = \frac{1}{2}m_p$, with m_p being the proton mass (Brown 1973), (TD Arber, Haynes, and Leake 2007).

3.3 Normalization

When we input the variables of the code we do so in dimensionless form. Of course, this can be done by choosing the most convenient normalization. When the numerical simulation includes additional physics like thermal conduction, partial ionization or optically thin radiative losses, we must specify the numerical values of the normalized length, magnetic field and density. This however is not needed when we run resistive MHD. The three basic quantities that we normalize are the length, magnetic field and density, so we end up with the following normalized ones.

$$x = L_0 \hat{x} \tag{3.9}$$

$$B = B_0 \hat{B} \tag{3.10}$$

$$\rho = \rho_0 \hat{\rho} \tag{3.11}$$

From these basic normalized quantities the rest of important quantities in MHD can arise. They are defined by the symbols we have used throughout this work.

$$u_0 = \frac{B_0}{\sqrt{\mu_0 \rho_0}} \tag{3.12}$$

$$t = \frac{L_0}{u_0} \tag{3.13}$$

$$p_0 = \frac{B_0^2}{\mu_0} \tag{3.14}$$

$$j_0 = \frac{B_0}{L_0 \mu_0} \tag{3.15}$$

$$E_0 = u_0 B_0 \tag{3.16}$$

$$\varepsilon_0 = u_0^2 \tag{3.17}$$

$$T_0 = \frac{\varepsilon_0 \bar{m}}{k_B} \tag{3.18}$$

$$\mu_{m0} = \bar{m} \tag{3.19}$$

From these we get,

$$u = u_0 \hat{u} \tag{3.20}$$

$$j = j_0 \hat{j} \tag{3.21}$$

$$p = p_0 \hat{p} \tag{3.22}$$

Like before, $\bar{m}$ is the average mass of ions so for example if we plasma with pure hydrogen it would be $\bar{m} = m_p$. For the solar corona the typical value is $\bar{m} = 1.2 m_p$. If we use the previous normalization to ideal MHD it would remove the vacuum permeability μ_0. For resistive MHD all we have to do is combine equations (3.3) and (3.5) and use the normalization to get,

$$\frac{\partial \hat{B}}{\partial \hat{t}} = \hat{\nabla} \times (\hat{u} \times \hat{B}) \; - \frac{1}{\mu_0 L_0 u_0} \hat{\nabla} \times (\eta \hat{\nabla} \times \hat{B}) \tag{3.23}$$

The normalization of resistivity is shown below since in the LareXd code resistivity is not assumed to be spatially uniform.

$$\hat{\eta} = \frac{\eta}{\mu_0 L_0 u_0} \tag{3.24}$$

The resistivity can however be uniformly applied or programmed to work only when the current density exceeds some value. Whether or not resistive diffusion takes place it can be controlled by the Lundquist number (S) so $\hat{\eta}$ is,

$$\hat{\eta} = \frac{1}{S} \tag{3.25}$$

Dropping the hats from the normalized variables using the Lagrangian derivative the normalized resistive MHD equations are,

$$\frac{D\rho}{Dt} = -\rho \nabla \cdot u \tag{3.26}$$

$$\frac{Du}{Dt} = \frac{1}{\rho}\Big[(\nabla \times B) \times B - \nabla p\Big] \tag{3.27}$$

$$\frac{DB}{Dt} = (B \cdot \nabla)u - B(\nabla \cdot u) - \nabla \times (\eta \nabla \times B) \tag{3.28}$$

$$\frac{D\epsilon}{Dt} = \frac{1}{\rho}\big[-p\nabla \cdot u + \eta j^2\big] \tag{3.29}$$

$$p = \epsilon\rho(\gamma - 1) \tag{3.30}$$

This code makes no reference to the plasma β parameter since plasma pressure is normalized to the magnetic pressure. It is possible to set the initial conditions of the magnetic field to zero $B = 0$ as this fixes $\hat{B}$ and does not affect B_0 which is the normalizing field. The LareXd code, when in $3D$, assumes that gravity is in the z direction. So after normalization the momentum equation (3.27) for the z component is given by,

$$\frac{Du}{Dt} = \frac{1}{\rho}\Big[(\nabla \times B) \times B - \nabla p\Big] - \hat{g} \tag{3.31}$$

where $\hat{g}$ is defined by,

$$\hat{g} = \frac{L_0 g}{u_0^2} \tag{3.32}$$

3.4 Uniform viscosity

Under normal circumstances the code includes shock viscosity. However for practical purposes we can either increase dumping effects near the boundaries or apply a uniform non-shock viscosity. This is done by adding the following incompressible viscosity term to the momentum equation.

$$\frac{\partial u}{\partial t} = \nu \nabla^2 u \tag{3.33}$$

We can choose the function ν which represents the spatially dependent viscosity function $\nu = \nu(r)$. The form of ν is specified as an initial condition whether it adds dumping to boundary conditions or as background viscosity and it does not affect heating.

3.5 Open boundaries

The different processes of the code have to be able to swap information so this is done by each process having ghost cells. Ghost cells are defined around the real cells in order to create a buffer for the exchange of boundary information. Because we want to limit the number of times that processes have to communicate, we implement two ghost cells in the buffer zone and this is how the real boundary conditions are applied.

Open boundaries are applied in LareXd using far-field Riemann characteristics. This is done so the Alfvén speed can be calculated and then use the result to project 1D Riemann invariants into ghost cells. In the case that the wave is outgoing the values are propagating from inside the domain into the ghost cells. In the opposite case where the waves are propagated inwards, values are carried in from the far-field. This of course demands a fixed far-field which means we have to specify the values of density ρ, internal energy ϵ, velocity and magnetic field components u_x, u_y, B_x, B_y, B_z . To avoid the open boundary conditions affecting the initial equilibrium these are set to the ghost cell values. In fact this puts a constrain on the magnetic field forcing it to not change a lot from the initial field so it would keep the open boundaries as accurate as possible. In order to avoid having the far-field problem for MHD ill posed, the far-field of the initial conditions at $t = 0$ must remain valid throughout the later stages of the simulation.

Reflection in the the boundaries is typically a few percent but can be as large as 10% in extreme cases. To cure that a stretched grid with a damping layer can be used. Most of the problems have to do with the fact that the open boundary problem for MHD might not be well posed which can significantly alter the result of the simulation.

3.6 The grid

In this section we will explain the way the computational grid correlates with the output arrays in physical space. Let's first examine the easiest case for 1D. We would have nx computational cells that are labeled from $ix = 1$ to $ix = nx$. However, the variables used in the code are not defined at the same point in a cell. Therefore, xb_i is the position of the right hand boundary of a cell and xc_i the position of the cell centre. This means that the left hand boundary of the computational domain is at xb_0. Each cell has a width of dxb_i and the distance between cell centres is dxc_i. In this coordinate system all quantities such as density ρ, pressure p, specific internal energy density ε are defined at cell centres, while velocities u are all defined at the cell boundaries. This is shown in Figure(3.1). Each component of the magnetic field is defined at different location. B_x is defined at cell boundary xb_i, while B_y and B_z at the cell center xc_i. A disadvantage of this is that in order to define the initial conditions inside the computational domain more points are needed for velocities u and B_x than for other quantities and the other magnetic field components. For example we would have to define u_x from $ix = 1$ to $ix = nx$.

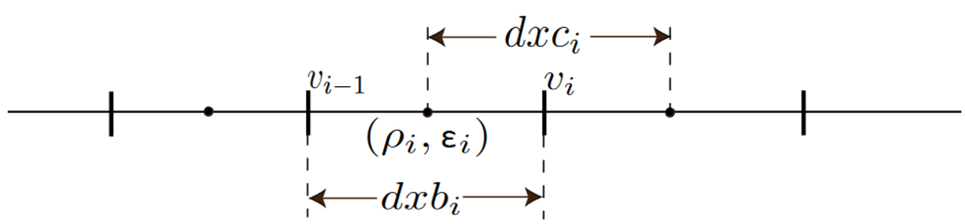

Figure 3.1: 1D staggered grid and the place each quantity is defined (Tony Arber, Brady, and Haynes 2018).

Moving on to a 2D grid where the velocities are defined at cell corners, other quantities and one direction of the magnetic field at cell centres. The other two magnetic field components are defined at cell edges as shown in Figure(3.2). In Figure(3.2) the mass density at the vertex ρ^u_{ij} is also shown, and if we define the kinetic energy density at $0.5\rho_{ij}u^2_{ij}$, we have $0.5\rho^u_{ij}u^2_{ij}$. After that, to obtain the vertex density we must average the densities in the cells that surround it. A more careful way to calculate these averages, which is the way it is frequently performed in the code, is by adding the total mass in the surrounding four cells and then dividing by the total area.

Finally, the realistic 3D grid which we use for this work is a simple extension of the 2D case. All quantities such as density ρ, pressure p, specific internal energy density ε are defined in the center of the cells, while velocities at the cell vertices. Since it's a function of z, gravity is also defined at cell vertices. On the other hand all magnetic field components are defined at the center of each surface of the volume. An illustration of the 3D case is shown in Figure(3.3).

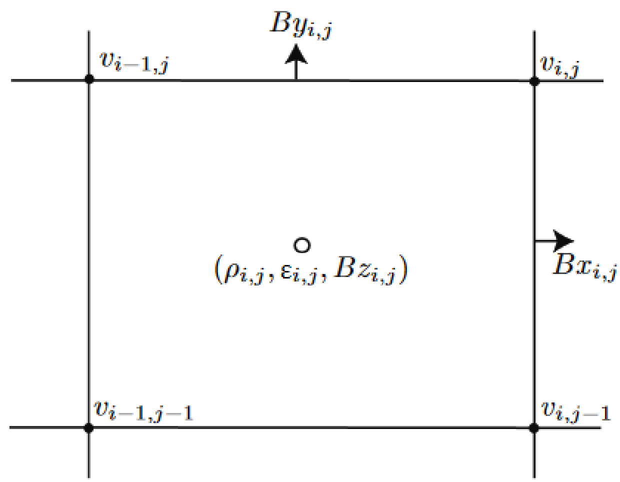

Figure 3.2: 2D staggered grid and the place each quantity is defined (Tony Arber, Brady, and Haynes 2018).

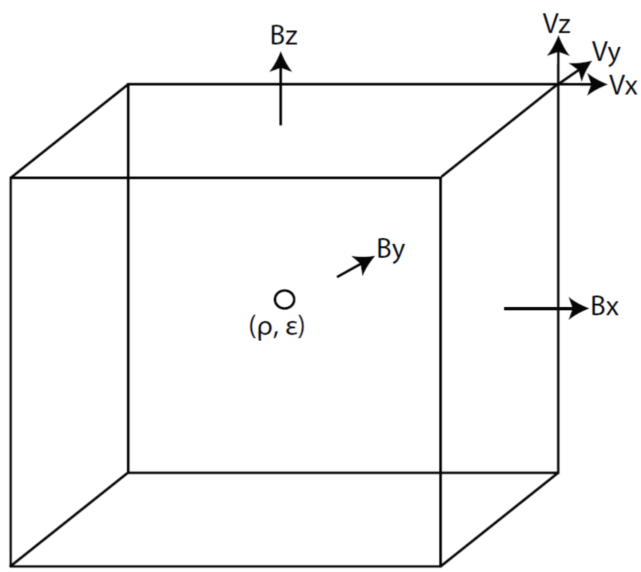

Figure 3.3: 3D staggered grid and the place each quantity is defined (Tony Arber, Brady, and Haynes 2018).

Model Setup

4.1 Initial Conditions

In this study, we used the Lare3D code to simulate the flux emergence process of a magnetic flux tube from the convection zone to the upper solar atmosphere. We set up the initial conditions using a plane parallel stratification and there is no convection in our code.

We use a computational domain of 420×420×420 uniform grid. This means that the computational box describes a physical space of 64.6 × 64.6 × 64.6 Mm. In the z-direction, the solar interior extends from -4.8 Mm to 0 Mm, the photosphere from 0 to 1.8 Mm, the chromosphere/transition region from 1.8 to 3.2 Mm and the corona from 3.2 to 59.8 Mm. Both the x and y axis extend from -32.3 Mm to 32.3 Mm. Below, we present the initial profiles of important quantities that describe the physical characteristics of the plasma throughout each layer of the stratified environment. Those plots are temperature, density, pressure and magnetic pressure over height. To obtain them we focus on the center of the computational box at $x = 0$ and $y = 0$, and then plot each quantity through height z in the beginning of the simulation at $t = 0$.

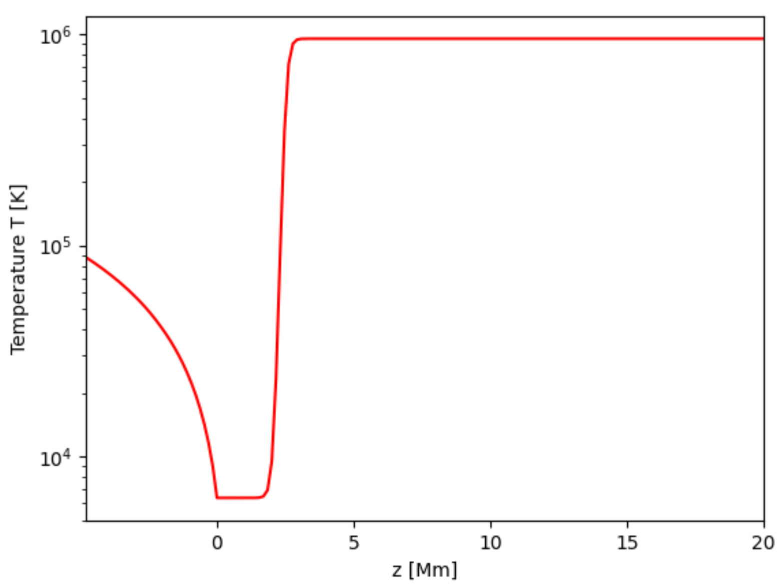

Figure 4.1: Temperature T profile for both horizontal and toroidal flux tubes, as it is imposed for the initial conditions.

Figure(4.1) show the temperature profile of the atmosphere, which is set up in a way that it resembles the temperature throughout the solar atmospheric layers. As we approach the photosphere from the interior the temperature decreases, then it reaches a minimum at the photosphere until it rapidly increases in the transition region, to reach a maximum plateau in the isothermal corona. The photosphere starts from $z = 0$ Mm up to $z = 1.4$ Mm. Then, the small and steep area where the temperature rises about two orders of magnitude is the transition region which extends from 1.4 to 3.2 Mm. From there and all the way up to $z = 59.8$ Mm we have the corona. Collectively all those layers are considered to be the solar atmosphere that incorporates heights of $z > 0$ Mm.

In order to set up the stratification below the atmosphere at $z < 0$, we first have to calculate the specific internal energy. We start by using the ideal gas law,

$$p = \frac{\rho k_B T}{\mu_m} \tag{4.1}$$

where μ_m the reduced mass $\mu_m = \frac{\bar{m}}{2-\xi_n}$ and $\bar{m}$ the average mass of ions.

To fully describe the specific internal energy we take into account ionization energy and we obtain the following expression,

$$\epsilon = \frac{p}{\rho(\gamma - 1)} + (1 - \xi_n)\frac{X_i}{\bar{m}} \tag{4.2}$$

with the adiabatic index being $\gamma = 5/3$ and the first ionization energy of hydrogen $X_i = 13.6$ eV. Since we don't include effects of partial ionization we set $\xi_n = 0$ and simplify the energy equation even further by completely disregarding the second term of equation(4.2). Afterwards, we choose this specific temperature profile so we can have a convectively stable interior. The temperature profile of the flux tube is given by equation,

$$\left(\frac{dT}{dz}\right)_{adiabatic} = -\frac{\mu_m g}{k_B}\frac{\gamma - 1}{\gamma} \tag{4.3}$$

In the atmosphere, $z > 0$, the temperature profile is due to a tangential function that takes the form of,

$$T(z) = T_{ph} + \frac{T_c - T_{ph}}{2}\left(\tanh\frac{z - z_c}{w_{tr}} + 1\right) \tag{4.4}$$

where z_c is the height of the base of the corona and T_c the temperature at that height. Also, T_{ph} is the temperature at the base of the photosphere which is $T_{ph} = 6300$ K. w_{tr} is the width of the transition region which we set up at $w_{tr} = 0.18$ Mm (Nozawa et al. 1992).

We assume that the plasma in the computational box is in hydrostatic equilibrium. So in order to find the initial profiles of pressure and density, we numerically solve the hydrostatic equation,

$$\frac{dp}{dz} = -gz \tag{4.5}$$

Figure(4.2) shows the pressure and the density against height in the same plot. In accordance with the observed stratification of the solar atmosphere, we have set up the gas pressure and density to decrease slowly as we move outwards in the solar interior, and drop by many orders of magnitude as we approach the photosphere. Above the photosphere pressure and density are relatively constant.

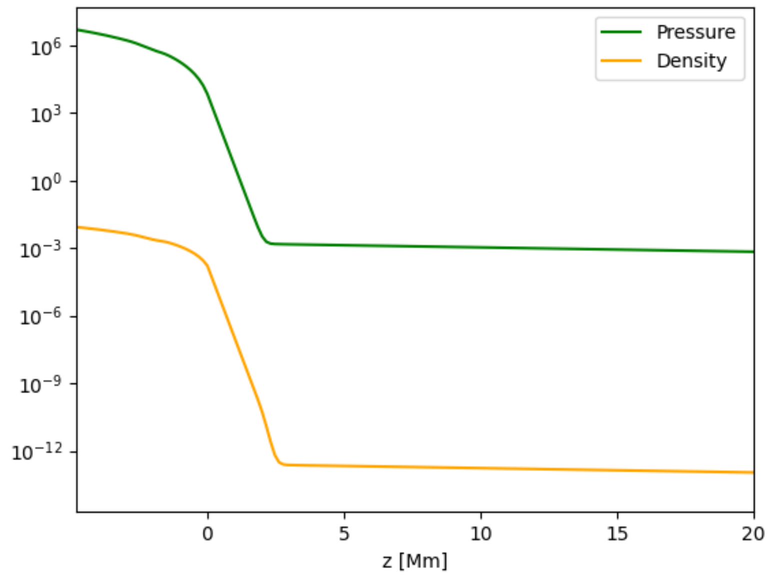

Figure 4.2: Profile of pressure P and density ρ.

Since there is an initial pressure profile in the interior even in the absence of the flux tube, by adding it we introduce additional pressure because of its magnetic field. Later on when we place the tube we will impose an axial magnetic field B_y that decreases from the tube's axis, so the surplus pressure should be in accordance to that. We use the following form to calculate the additional pressure (M. Murray et al. 2006) (Chouliaras, Petros Syntelis, and Vasileios Archontis 2023).

$$p_{add} = \frac{B_y^2}{2\mu}\left(\alpha^2\left(\frac{R^2}{2} - r^2\right) - 1\right) \tag{4.6}$$

Now, the pressure in the solar interior becomes,

$$p_i + p_{add} = p_0 \tag{4.7}$$

which describes the new pressure equilibrium.

If the tube was completely uniform it would mean that it is in an environment of thermodynamic equilibrium, therefore it wouldn't be able to rise. For that reason we will introduce a density deficit in the middle of the tube's length. This density deficit in the initial conditions acts as a perturbation that will make the tube buoyant and allow it to emerge. We also assume that in the solar interior the plasma would be in thermal equilibrium with the already existing environment. This is given by, $T_i = T_0$. It also suggests that the density deficit inside the flux tube is,

$$\Delta\rho = -\rho_0 \frac{p_{add}}{p_0} \tag{4.8}$$

However, we expect the emergence of the tube to create an Ω-loop shape, so in order to avoid the uniform emergence of the whole tube, we enforce the density deficit to have a higher value at the center of the tube and to reduce drastically towards its edges. The density deficit is then modified and given as a function of the tube's axis by the following expression (Chouliaras, Petros Syntelis, and Vasileios Archontis 2023) (Syntelis, Archontis, and Tsinganos 2017).

$$\Delta\rho = -\rho_0 \frac{p_{add}}{p_0} e^{-y^2/\lambda^2} \tag{4.9}$$

Here, the parameter λ measures the length of only the buoyant part of the tube. Our choice for the length scale is $\lambda = 5$ that incorporates a physical space of $z = 0.9$ Mm.

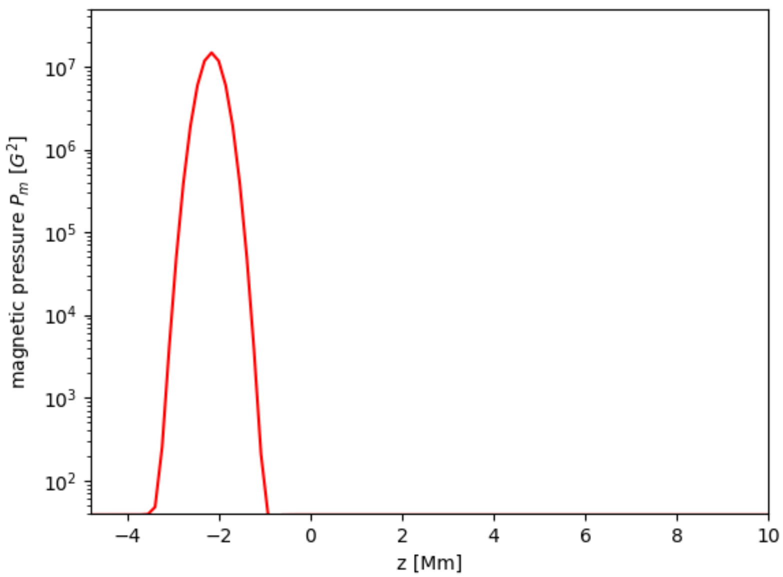

Figure 4.3: Magnetic pressure P_m indicating the location of the flux tube beneath the photosphere.

In Figure(4.3) we have plotted the magnetic pressure P_m. Specifically we focused on the center of the x-axis. Then, we plotted the magnetic pressure throughout all heights at $t = 0$ before any buoyant force acts on the tube. Since the flux tube we use, is placed at $-2.1\ Mm$ below the photosphere, evidently we see large values of magnetic pressure gathered around the center of the flux tube. Magnetic pressure is calculated using the following equation.

$$p_m = \frac{1}{8\pi}(B_x^2 + B_y^2 + B_z^2) \tag{4.10}$$

In all simulations, the flux tube is oriented along the y-axis, and the magnetic field for the horizontal tube is defined by (Fan 2001), (MacTaggart and Alan W Hood 2009) and given in cylindrical coordinates as,

$$B = B_y \hat{y} + B_\phi \hat{\phi} \tag{4.11}$$

where,

$$B_y = B_0 e^{-r^2/R^2} \tag{4.12}$$

$$B_\phi = \alpha r B_y \tag{4.13}$$

where ϕ is the azimuthal direction in the tube cross-section, R is the tube's radius set at $R = 0.45$ Mm and r the radial distance from the tube's axis for both horizontal and toroidal flux tubes.

After introducing the initial stratification, we use the Lare3D code to numerically solve the following MHD equations in Cartesian geometry (TD Arber, Longbottom, et al. 2001). Those equations have been presented in Chapter 3 and are repeated here in dimensionless form.

$$\frac{\partial \rho}{\partial t} + \nabla \cdot (\rho u) = 0 \tag{4.14}$$

$$\frac{\partial (\rho u)}{\partial t} = -\nabla \cdot (\rho\ uu) + (\nabla \times B) \times B - \nabla p + \rho g + \nabla \cdot S \tag{4.15}$$

$$\frac{\partial(\rho\epsilon)}{\partial t} = -\nabla \cdot (u\rho\epsilon) - p\nabla \cdot u + Q_{joule} + Q_{visc} \tag{4.16}$$

$$\frac{\partial B}{\partial t} = \nabla \times (u \times B) + \eta\nabla^2 B \tag{4.17}$$

$$\epsilon = \frac{p}{\rho(\gamma - 1)} \tag{4.18}$$

where all the symbols have their usual meaning and in the perfect gas assumption the specific heat is set at $\gamma = 5/3$.

4.2 Emergence above the photosphere

We start by explaining the emergence process of the flux tube. In Figure(4.4) we illustrate the contour lines of the axial magnetic field B_y. The background represents the density distribution of plasma in the interior. We focus on the early stages of the simulation as well as at heights beneath the photosphere, to illustrate how a cylindrical tube expands due to the pressure difference of itself and the environment while rising at the photosphere. As the tube moves upwards the pressure inside the tube increases, while the pressure on the surrounding environment decreases. This lead to the expansion of the tube in the radial direction due to pressure difference. The four snapshots of Figure(4.4) cover a time frame of the first 11 minutes of the simulation and during that period the tube's axis has traveled upwards at a distance of 2 Mm.

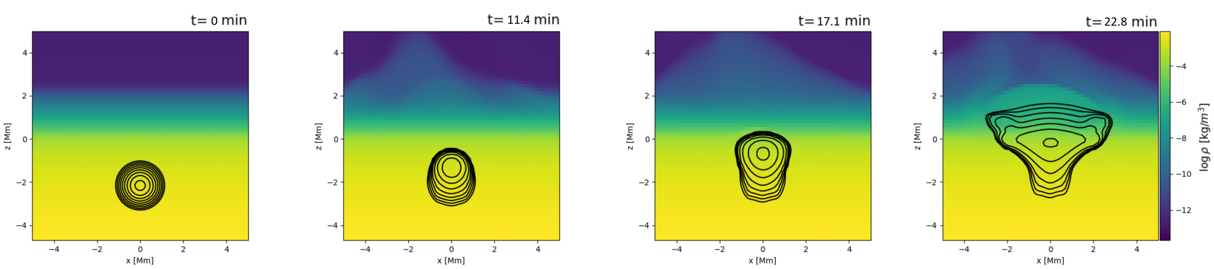

Figure 4.4: Contour lines of the B_y of the highly twisted ($\alpha = 0.4$) horizontal tube as it expands when it reaches the photosphere. $t = 0$, 11.4, 17.1, 22.8 minutes respectively. On the background we have the logarithm of the density.

The photosphere is isothermal and stable against the convective instability. This means that when dense plasma reaches the photosphere, in order for it to rise even further, it would have to overcome the force of gravity. A way for this to happen is if the buoyancy instability acts upon the plasma in the area above the photosphere. Above $z > 0$, the stratification is sub-adiabatic, so for the plasma to eventually emerge above the photosphere, the buoyancy instability criterion given bellow has to be satisfied (Newcomb 1961)(Acheson 1979)(Archontis, Moreno-Insertis, et al. 2004)(Moreno-Insertis 2006).

$$-H_p \frac{\partial}{\partial z}(\log B) > -\frac{\gamma}{2}\ \beta\delta + k_{\parallel}^2\Big(1 + \frac{k_{\perp}^2}{k_z^2}\Big) \tag{4.19}$$

The variables expressed are, δ the super-adiabatic excess $\delta = \nabla - \nabla_{adiabatic}$ where ∇ the logarithmic temperature gradient and $\nabla_{adiabatic}$ its adiabatic value. For an isothermal stratification like ours the super-adiabatic excess is $\delta = -0.4$ $k_{\parallel}$ and $k_{\perp}$ the wave numbers of the perturbations in the direction parallel and vertical to the magnetic field, while k_z in the $z-$ direction. H_p the pressure scale and β the plasma beta parameter.

The second term on the right hand side of equation(4.19) can be neglected because it has an order of magnitude around $\sim 10^{-15}$ which is much smaller than the minimum value of $\beta \approx 10^{-12}$ on the first term on the right. Equation(4.19) can be rearranged as,

$$\frac{2H_p}{\gamma\delta\beta}\frac{\partial}{\partial z}(\log B) > 1 \tag{4.20}$$

This equation gives a clear picture of the instability, and when it is satisfied the buoyancy force will allow the plasma of the flux tube to penetrate beyond the photosphere.

As the flux tube crosses the photosphere the magnetic pressure increases an surpasses the local gas pressure which means that their ratio will also increase. However since their ratio β is on the denominator of equation(4.20), the fraction as a whole will increase. As a consequence of the field compressing on the sides of the tube in the $y-$ direction, the gradient of the magnetic field also decreases. At some point the decrease of β will surpass the decline of B which will increase the value of the fraction of equation(4.20), and when it is greater than one the criterion will be satisfied, allowing for the flux tube to penetrate the whole photosphere.

The expansion of the emerging field forms an envelope that surrounds the flux tube (Moore, Alphonse C Sterling, Hudson, et al. 2001), (Vasilis Archontis and Alan William Hood 2012). The envelope field can be seen in our own simulations in Figure(4.5) where the flux tube has penetrated the photosphere and expands as it rises. Figure(4.5) shows the contour lines of the magnetic field in the y direction with plasma density on the background. For the moment the envelope field expands and presses the surrounding plasma, until later when the an ejective explosion will blow out the envelope with the twisted flux tube inside it.

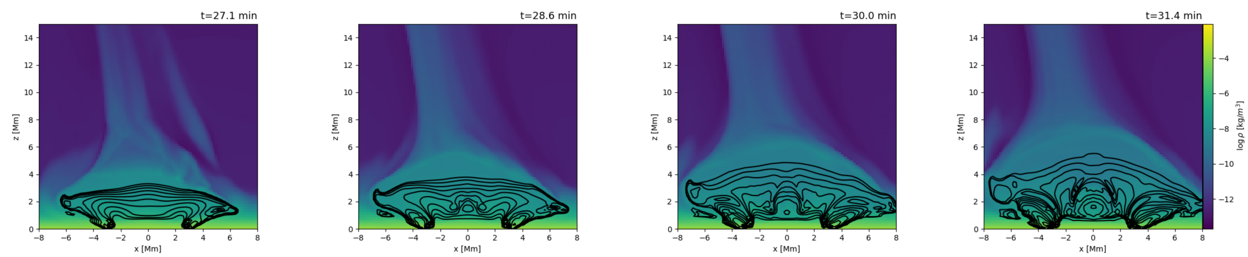

Figure 4.5: Envelop field expansion in the early stages of the highly twisted ($\alpha = 0.4$) horizontal flux tube emergence. The background colors correspond to the density logarithm.

4.3 Standard jet

The emergence phase is an important process for bringing magnetic field from the convection zone to the upper atmosphere. However it is not enough to produce the eruptive events observed in the Sun. In this study we focus on the interaction between the emergent field and an external ambient field that results in jet formation and eruption-driven jets.

The ambient field has a strength of 10 G in a direction that points upwards, but not entirely perpendicular to the surface. It forms an $\theta = 11°$ degree angle with the $z-$axis, and a $\phi = 183°$ with the $y-$axis. This setup ensures that the ambient magnetic field lines and the emerging field lines are antiparallel, which will trigger reconnection once they converge (Galsgaard et al. 2007). This creates a current sheet where free magnetic energy is released and converted, via Joule heating, into thermal energy heating the plasma. A portion of this magnetic energy is also converted into kinetic energy that accelerates the plasma through the outflow regions. Evidence of this is the standard jet formation that is visible after the flux tube emerges in the corona and throughout the whole simulation (Heyvaerts, Eric R Priest, and Rust 1977), (Forbes and Priest 1984), (Isobe et al. 2005).

A schematic representation of jet formation is illustrated in Figure(4.6). We see that magnetic fields emerge from beneath the photosphere due to buoyancy. Afterwards it expands further creating the $\Omega-$like loop, and when the magnetic field lines of the loop come close enough with the coronal field to create a current sheet, they reconnect at the neutral point. On both sides of the reconnection we see the formation of two jets at opposite directions. The upwards reconnection jet is the main mechanism with which energy leaves the main structure and is transported to higher altitudes, while the downwards jet ejects the plasma on the base of the newly formed smaller arcade in the lower right side of the third panel of Figure(4.6), (Shibata, Ishido, et al. 1993).

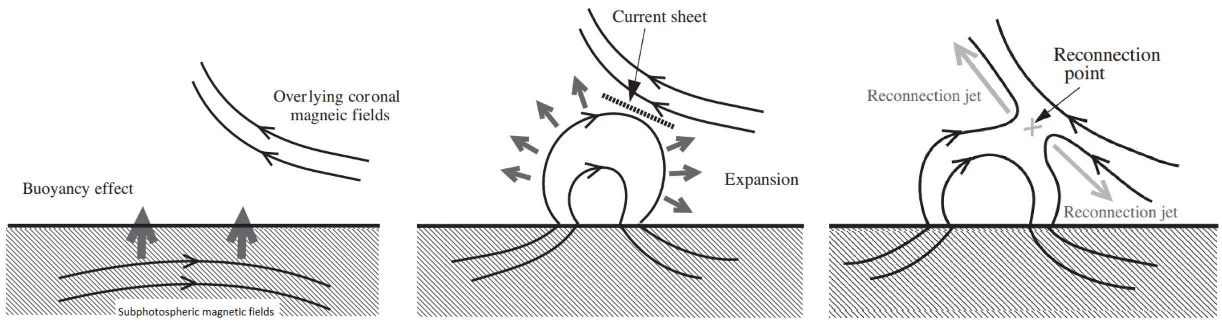

Figure 4.6: From panel left to right we have a schematic representation of how the structure of the flux tube interacts with the ambient coronal magnetic field. On the right side panel we have the neutral point marked with "X" where reconnection takes place, as well as the jets that are subsequently created (Shibata and Magara 2011).

This cartoon of the standard jet bares a close resemblance to actual jets formed in the solar atmosphere, with many observations revealing that similarity (Patsourakos et al. 2008), (Shen 2021), (Schmieder 2022), (Li et al. 2012). Figure(4.7) shows a jet observed with IRIS, taken from the work of (Joshi et al. 2020). In panel(a) we can see the structure resembling the standard jet formation, along with a cool bright dome in the northern side of the null point. Panel(b) shows a similar picture of the jet, this time with the arrow covering the width of the cool jet. In panel(c) we have the collimated narrow hot jet. In this panel, the southern loop is shown to be a bright and hot structure, and the same is true for the point at the base of the jet. Panel(d) is obtained through differential emission measure (DEM) analysis, and the null point along with the long bright current sheet is also shown with a white arrow. The black points in all panels are produced by extreme saturation and are not part of the observed structures (Joshi et al. 2020).

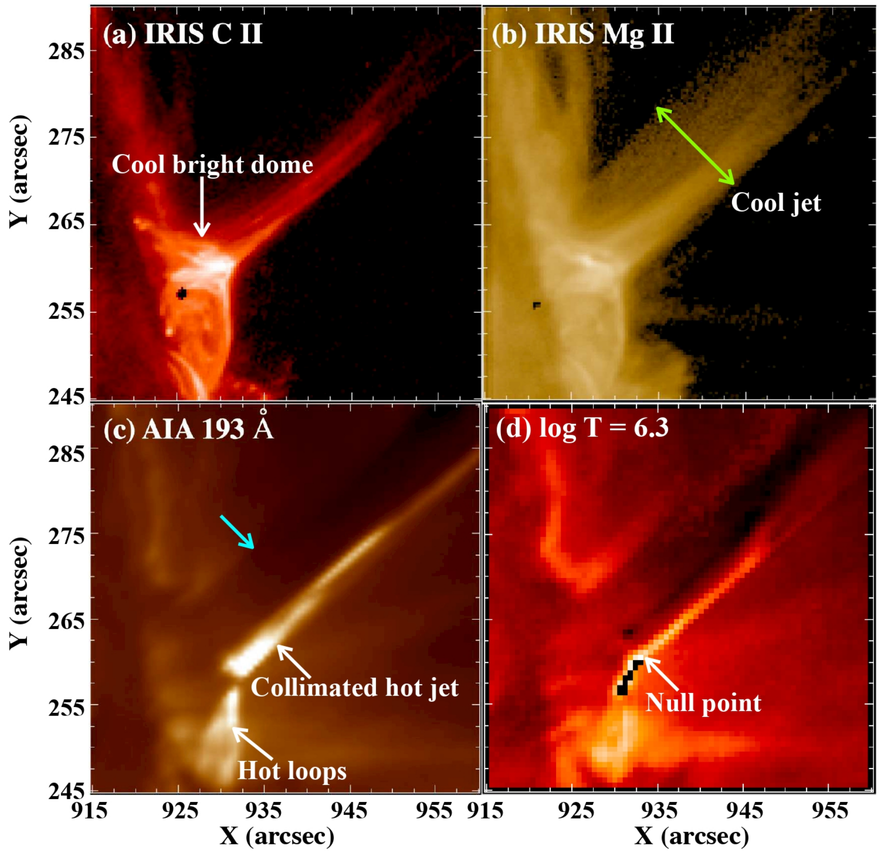

Figure 4.7: Solar jet observed with IRIS at 11:45 UT in panel (a) and (b). In panel(c) there is the same jet observed with AIA at 193 Å, while in panel(d) a DEM map at a fixed temperature $\log T = 6.3$. Image reproduced from (Joshi et al. 2020).

A similar behavior is observed in our own simulations. Figure(4.8) has three panels in sequence showing the temperature logarithm during the formation of the standard jet from a horizontal flux tube. We can see that when reconnection takes place as the flux tube compresses along the ambient magnetic field. The two jets that formed from the reconnection, eject hot plasma which is reflected in the temperature increase at the spine of the jet well into the corona.

On Figure(4.9) we have the same sequence, but this time with the logarithm of the density on the background. We can clearly see the difference in density between the emerging flux tube, which is denser than the corona. As the magnetic field of the flux tube reconnects with the ambient field, we can also expect dense plasma to be ejected from the outflow regions. An increase in the density can be seen both in the spine of the standard jet, where the plasma moves upwards following the "open" field lines, as well as in the opposite jet that moves downwards towards the base of the corona.

On Figure(4.10), we plotted the $z-$component of the velocity at the same time as the other quantities which is right after the formation of the standard jet. Once again the reconnection process ejects material that are subsequently accelerated out of the main structure. The signature of this process is very clearly shown in the plot where there is an increase in the vertical speed of plasma as it leaves the area of reconnection and moves upward. A similar behavior can be observed at the jet that flows downwards where we have the vertical component of velocity take negative values as the plasma moves downwards. All these plots only help to further establish the similarity of the phenomena observed in our own simulations with pre existing theoretical work (Shibata, Ishido, et al. 1993), (Yokoyama and Shibata 1996), (Shibata and Magara 2011).

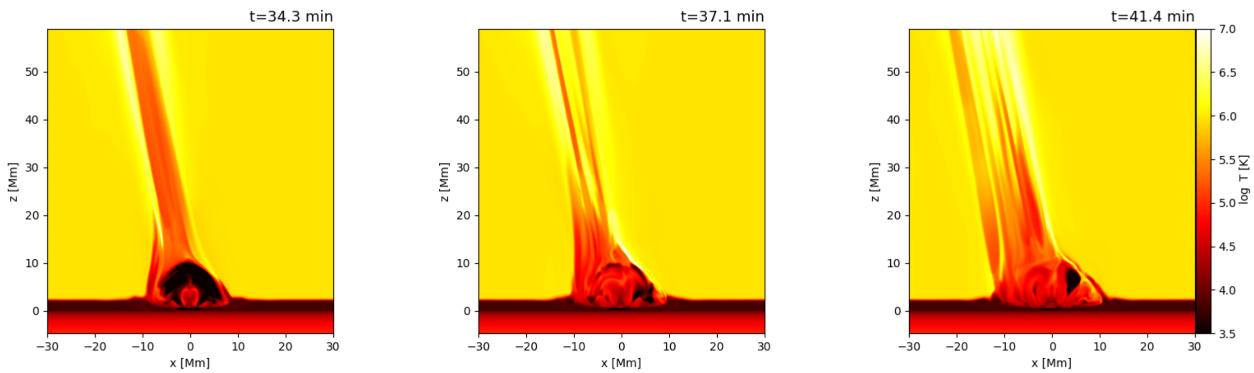

Figure 4.8: Temperature distribution during the formation of the standard jet.

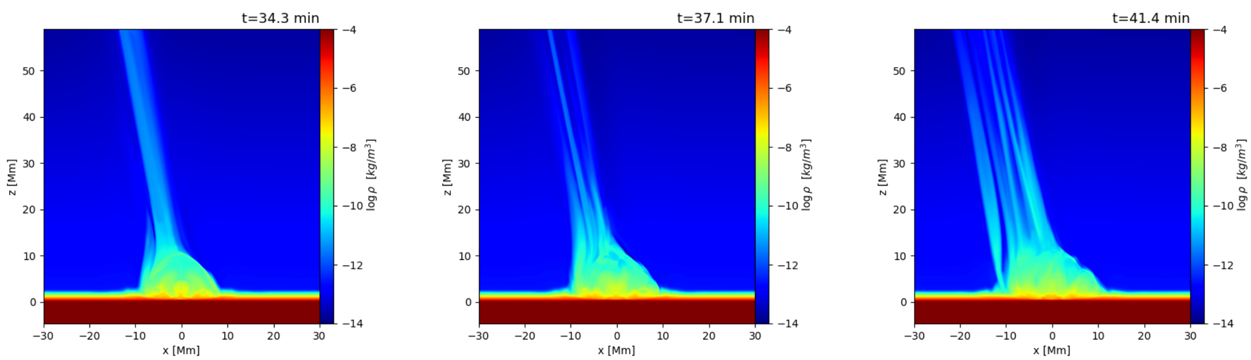

Figure 4.9: Density distribution during the formation of the standard jet.

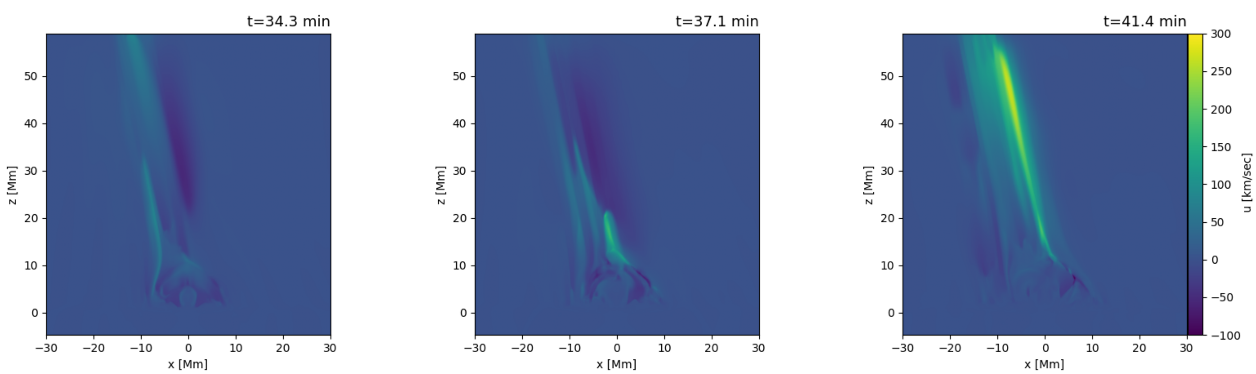

Figure 4.10: z-component of the velocity during the formation of the standard jet.

4.4 Blowout jet

The standard jet, as we discussed before, is formed from the reconnection of the emerging field with an external ambient field. This process will eject plasma upwards along the open ambient magnetic field lines but also downwards forming the post-flare hot coronal loop. However, this is not the only way to have ejection of plasma. Plasma can be also ejected in an eruptive manner in a process known as an eruption-driven jets or "blowout jets". Unlike the standard jet, cooler plasma is ejected from a blowout jet where this cool plasma most likely comes from the jet's base arch. So, the main difference between a standard and a blowout jet is whether the base arch remains closed, as in standard jets, or erupts open like in blowout jets (Moore, Cirtain, et al. 2010).

As the standard jet phase evolves, there is a definite formation of a sigmoid shaped bipolar region. The opposite polarity feet of the field lines in the sheared arcade get close to each other, so fast reconnection can start (Ballegooijen and Martens 1989), (Archontis and Török 2008), (Adams et al. 2014). This reconnection leads to new field lines at the two ends of the current sheet which is created at the feet of the sheared arcade. The arcade field lines on one of the sides of the current sheet become fully reconnected, while there is still flux residue on the other side. This imbalance results in reconnection between field lines of the original hot loop of the standard jet with the remnant field lines from the arcade. The new emerging field is strongly sheared and twisted with enough free energy to drive an ejective eruption (S. Antiochos, C. DeVore, and Klimchuk 1999), (C Richard DeVore and Spiro K Antiochos 2008), (Wyper, Spiro K Antiochos, and C Richard DeVore 2017). The erupting material is ejected onto the overlying open field with high velocity. Therefore the eruption is guided along the field lines where the original jet was propagating. The eruption will be seen not only to disturb a large part of the emerged structure but also, to propagate as a temporary impulsive jet with a complex structure roughly in the same direction as the standard jet, eventually reaching the top of the computational box (Moreno-Insertis, Galsgaard, and Ugarte-Urra 2008; Fernando Moreno-Insertis and Klaus Galsgaard 2013), (C. Liu et al. 2011), (Micheal J Murray, Driel-Gesztelyi, and Baker 2009).

A schematic representation of a blowout jet can be seen in the four cartoons of Figure(4.11). In panel (a) we have the initial set up which is similar to that of the standard jet case. The emergent bipolar field which creates a loop, along with the ambient coronal magnetic field which is the open vertical lines. The current sheet is shown as a black line. The structure evolves into that of panel (b) where magnetic reconnection occurs at the location of the neutral point ("X"), and a narrow jet spire forms along the new open field lines. The bipolar field is then destabilized which leads to a full eruption as shown in panel (c) with various reconnection points (Manchester IV et al. 2004). Since this bipole originally contained cold material, the eruption forces them upwards and we have a mixture of heated field lines from the reconnection along with cooler ones from the blowout eruption. In the end panel (d) shows the late stages of the eruption where the newly reconnection-produced loops sustain a standard jet formation (Raouafi et al. 2016), (Moore, Cirtain, et al. 2010), (Moore, Alphonse C Sterling, Falconer, et al. 2013), (Shen et al. 2012).

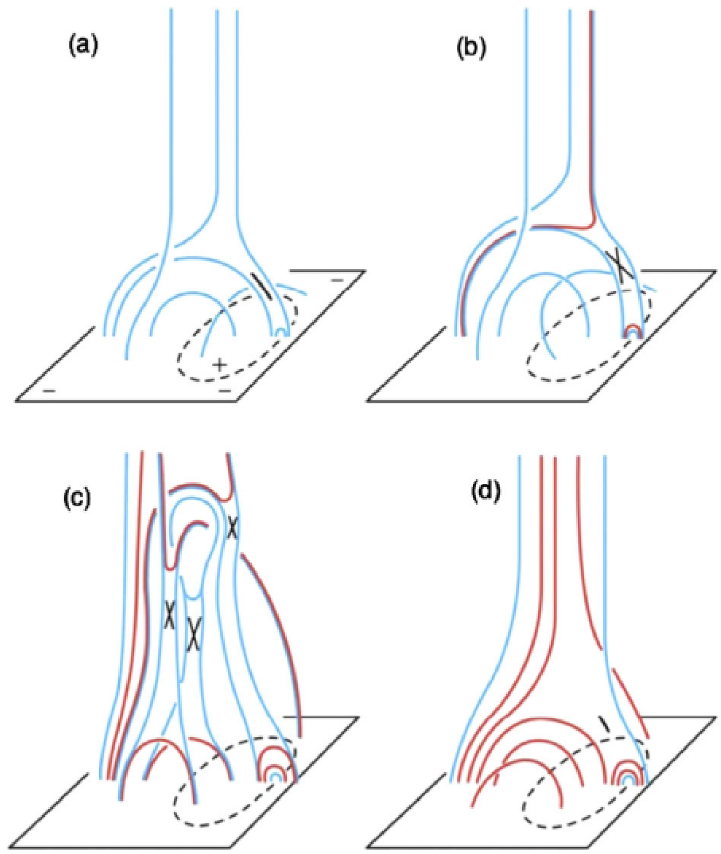

Figure 4.11: Blowout jet cartoon (Moore, Cirtain, et al. 2010)

The above sketch provides a picture that is very similar to observations of blowout jets in the Sun, along with many other observations (Peter R Young and Muglach 2014), (Gou et al. 2024), (Tang et al. 2021), (Chandra et al. 2017). On Figure(4.12) we see the progression of a blowout jet observed in coronal X-ray images from Hinode/XRT. The sequence of those pictures starts just before the outbreak of the jet and continues up until its decay. The jet is viewed mainly from the side, while its length scale is in the order of tens of thousands of kilometers. The downwards white arrows point to the lower leg of the jet's spine which shows as a bright point in the arcade. The upwards white arrows on the other hand point to the brightening in the interior of the base arch. In the third frame, the brightening in the interior of the base arch has spread towards the other end of the arch, and the jet spire is visible. The spire has an additional strand that begins from the bright point end of the base arch. Since the foot of the strand is in front of the bright point, it means that that the strand's field lines have not been heated by the reconnection yet. So, because in X-ray observations the the interior of the base arch brightens at the same time the jet appears, we understand that in this type of jet the interior of the base arch is involved in the eruption unlike the standard jet where it remains static. In the later stages, the the non-standard strand and the bright interior of the base arch starts to disappear. During the last frames, the front strand has faded away with only a single-strand spire rooted at the end of the base arch opposite to the bright point, which is the standard jet structure remaining.

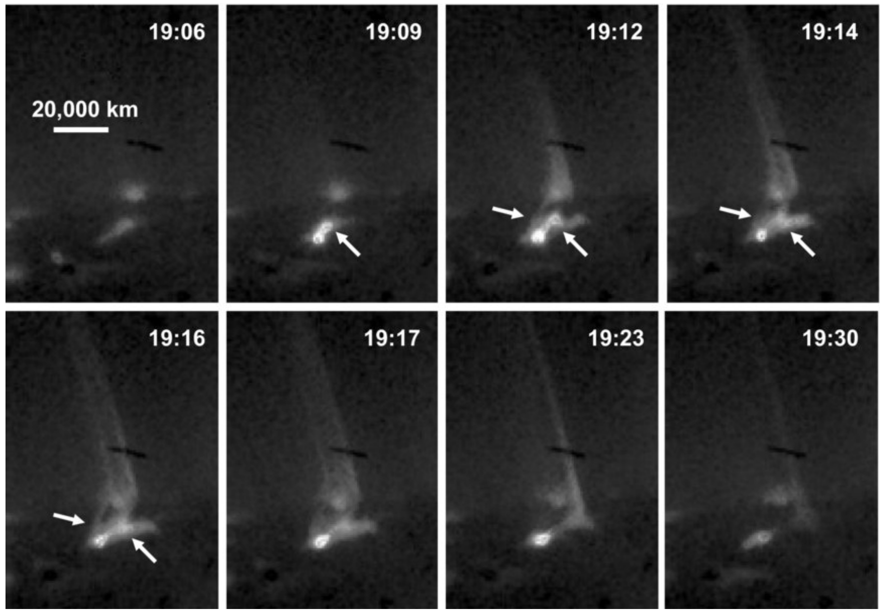

Figure 4.12: Observation of a blowout jet (Moore, Cirtain, et al. 2010)

Just like in the case of the standard jet, our own simulation is in agreement with blowout jets observations. Figure(4.13), (4.14) and (4.15) show the morphology of a blowout jet created by a horizontal flux tube. On Figure(4.13) we have the temperature logarithm during the eruption. As expected from theoretical investigations (Moore, Cirtain, et al. 2010) it starts with a picture very similar to that of the standard jet, and magnetic reconnection between the loop and the ambient magnetic field takes place at the current sheet where the temperature increases.

The eruption of cool material from a destabilized bipolar field can be seen better in Figure(4.14) where a series of plots of the density logarithm are shown. The cooler material is ejected from the main structure and follows the path of the new field lines created from the reconnection.

Furthermore, Figure(4.15) shows the increase in vertical velocity in the reconnection region which is consistent with the ejection of material. Particularly in the forth panel, we have a significant increase in the upwards speed through the jet spine and not so much in the loop which suggests that a big portion of material is separated, accelerated and leave the main structure.

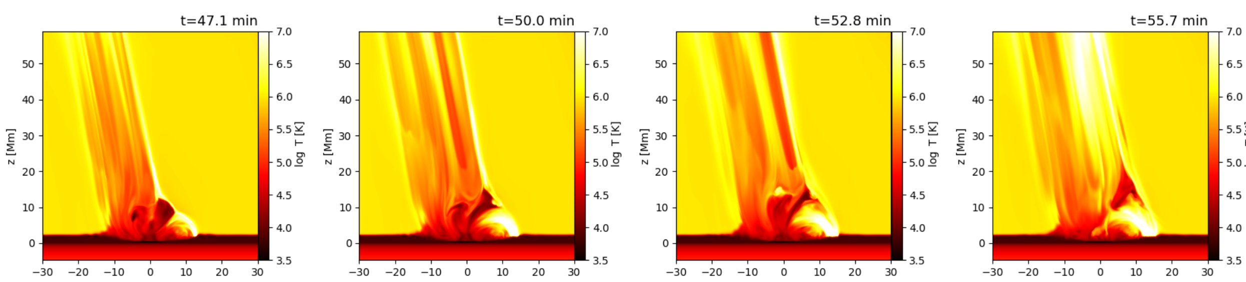

Figure 4.13: Temperature distribution during the blowout jet phase.

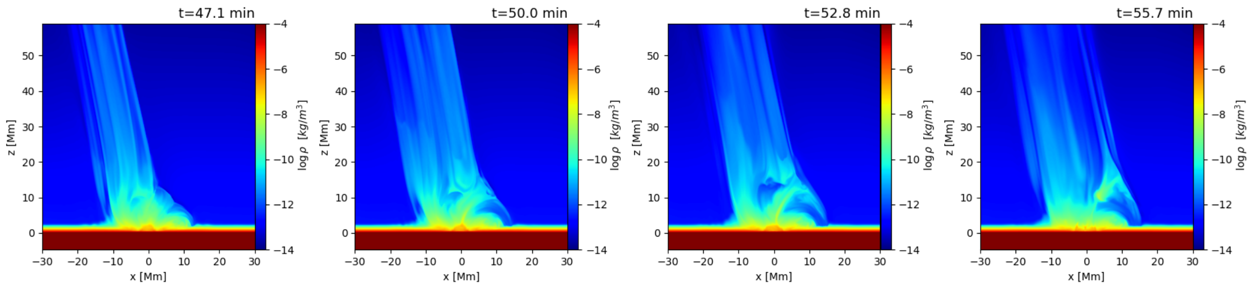

Figure 4.14: Density distribution during the blowout jet phase.

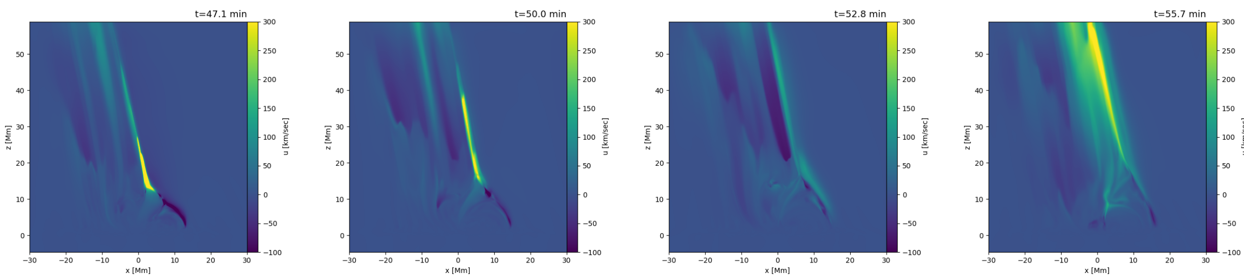

Figure 4.15: Distribution of the z-component of the velocity during the blowout jet phase.

4.5 Toroidal tube setup

Since we have described the way we implement a horizontal flux tube for our simulations, we should also present an alternative to that which is a toroidal flux tube. The reason behind this is that a different geometry of the flux tube, having distinct characteristics, may prove to be more accurate to describe the emergence process as we observe it in the Sun. The equations that govern a toroidal flux tube and how it is set up in our experiments are derived in this segment.

To set up a toroidal magnetic field, we transform our original cartesian coordinate to cylindrical $(R, \phi, -x)$. The transformation used is,

$$R^2 = y^2 + (z - z_0)^2 \tag{4.21}$$

$$y = R \cos \phi \tag{4.22}$$

$$z - z_0 = R \sin \phi \tag{4.23}$$

where the tube is placed in the $y-$direction, z being the height and z_0 the value of the base of the computational box, in our own experiment it is -4.7 Mm.

Afterwards, we express the magnetic field in terms of a flux function $A = A(R, x)$ as,

$$B_R = -\frac{1}{R}\frac{\partial A}{\partial x} \tag{4.24}$$

$$RB_\phi = R_0 F(A) \tag{4.25}$$

$$B_x = \frac{1}{R}\frac{\partial A}{\partial R} \tag{4.26}$$

where R_0 is the major radius of the torus. The Grad-Shafranov equation takes the form,

$$R\frac{\partial}{\partial R}\left(\frac{1}{R}\frac{\partial A}{\partial R}\right) + \frac{\partial^2 A}{\partial x^2} + R_0^2 F\frac{dF}{dA} + R^2\frac{dP}{dA} = 0 \tag{4.27}$$

where $RB_\phi = R_0F(A)$ and $\mu p = P(A)$ are expressed in terms of the flux function A. In the above equation(4.27) we define a local toroidal coordinate system that transforms the equation to,

$$\frac{\partial^2 A}{\partial r^2} + \frac{1}{r}\frac{\partial A}{\partial r} + \frac{1}{r^2}\frac{\partial A}{\partial \theta} - \frac{1}{R_0 + r\cos\theta}\left(\cos\theta\frac{\partial A}{\partial r} - \frac{\sin\theta}{r}\frac{\partial A}{\partial \theta}\right) + R_0^2 F\frac{dF}{dA} + \left(R_0 + r\cos\theta\right)^2\frac{dP}{dA} = 0 \quad (4.28)$$

where the transformations are,

$$r^2 = x^2 + (R - R_0)^2 \quad (4.29)$$

$$R - R_0 = r\cos\theta \quad (4.30)$$

$$x = r\sin\theta \quad (4.31)$$

Assuming that the minor radius of the flux tube a is significantly smaller than the radius of the torus, $a \gg R_0$ as well as that $P(A) = \tilde{P}(A)/R_0^2$ we can expand the solution in powers of a/R_0.

$$A = R_0\left(A_0(r) + \frac{a}{R_0}A_1(r,\theta) + \left(\frac{a}{R_0}\right)^2 A_2(r,\theta) + ...\right) \quad (4.32)$$

By keeping terms of zero-order we get a cylindrically symmetric solution that satisfies,

$$\frac{1}{r}\frac{\partial}{\partial r}\left(r\frac{\partial A_0}{\partial r}\right) + \frac{1}{2}\frac{dF^2}{dA_0} + \frac{dP}{dA_0} = 0 \quad (4.33)$$

Multiplying the above equation with $B_\theta = \frac{\partial A_0}{\partial r}$ nd switching derivatives to dr we get,

$$\frac{B_\theta}{r}\frac{d}{dr}\left(rB_\theta\right) + \frac{1}{2}\frac{dB_\phi^2}{dr} + \frac{dP}{dr} = 0 \quad (4.34)$$

From this standard cylindrical equation we can choose the same solution as in the case of a horizontal flux tube which is,

$$B_\phi = B_0 e^{-r^2/a^2} \quad (4.35)$$

$$B_\theta = \frac{\partial A}{\partial r} = arB_\phi = arB_0 e^{-r^2/a^2} \quad (4.36)$$

Finally those solutions will be expressed in terms of cartesian coordinates. To do that we give B_θ in terms of cylindrical components B_R and B_X,

$$B_R = -B_\theta(r)\sin\theta = -B_\theta(r)\frac{x}{r} \quad (4.37)$$

$$B_x = B_\theta(r)\cos\theta = B_\theta(r)\frac{R - R_0}{r} \quad (4.38)$$

Afterwards we express B_R and B_ϕ in terms of B_y and B_z as,

$$B_x = B_\theta(r)\frac{R - R_0}{r} \quad (4.39)$$

$$B_y = -B_\phi(r)\frac{z - z_0}{R} + B_R\frac{y}{R} \quad (4.40)$$

$$B_z = B_\phi(r)\frac{y}{R} + B_R\frac{z - z_0}{R} \quad (4.41)$$

At last we have the full expression of each component of the toroidal tube's magnetic field in cartesian coordinates (Alan William Hood et al. 2009), (MacTaggart and Alan W Hood 2009).

$$B_x = B_\theta(r)\frac{R - R_0}{r} \quad (4.42)$$

$$B_y = -B_\phi(r)\frac{z - z_0}{R} - B_\theta(r)\frac{x}{r}\frac{y}{R} \quad (4.43)$$

$$B_z = B_\phi(r)\frac{y}{R} - B_\theta(r)\frac{x}{r}\frac{z - z_0}{R} \quad (4.44)$$

4.6 Characteristics of the flux tubes

The main purpose of this work is to compare the two different tube setups. So, the environment in which the flux tubes are placed must be the same in order to draw reliable conclusions. However, the tubes have some small differences that are consequences of their geometry. The main difference is the length of each tube. In the case of the horizontal flux tube, we have a cylindrical tube with infinite length, obviously with only a small portion of it contributing to the emergence process. The toroidal tube on the other hand, has a fixed length with its feet anchored at the bottom of the computational domain. This of course puts a constraint on the tube's length which is $L_{tor} = 2.7$ Mm. Both tubes have a radius of $R = 0.45$ Mm and a magnetic field of $B_{tube} = 6300$ G.

The normalization we use is based on the values of density, length and magnetic field at the photosphere. So we have $\rho = 1.67 \cdot 10^{-4}\ kg/m^3$, $L_0 = 0.18$ Mm and $B_{ph} = 300$ G respectively. From those we can calculate, the pressure $p_0 = 713.2$ Pa, the temperature $T_0 = 5100$ K, the velocity $u = 2.1$ km/sec and the time of each step of the simulation at $t_0 = 85.7$ sec.

An overall picture of the flux tubes before the simulation starts, is given at Figure (4.16) where we see the $y-$component of the magnetic field from the front. This means that we see the $y - z$ surface at $t = 0$. Since the magnetic field is constructed in a way that it is contained inside the tube, we can still use that to distinguish each tube's scale and shape. Even though the plot for the horizontal tube on the right side is zoomed in and does not include the box's boundaries, we can see how the tube is placed as a straight cylinder with no footpoints on the solar surface.

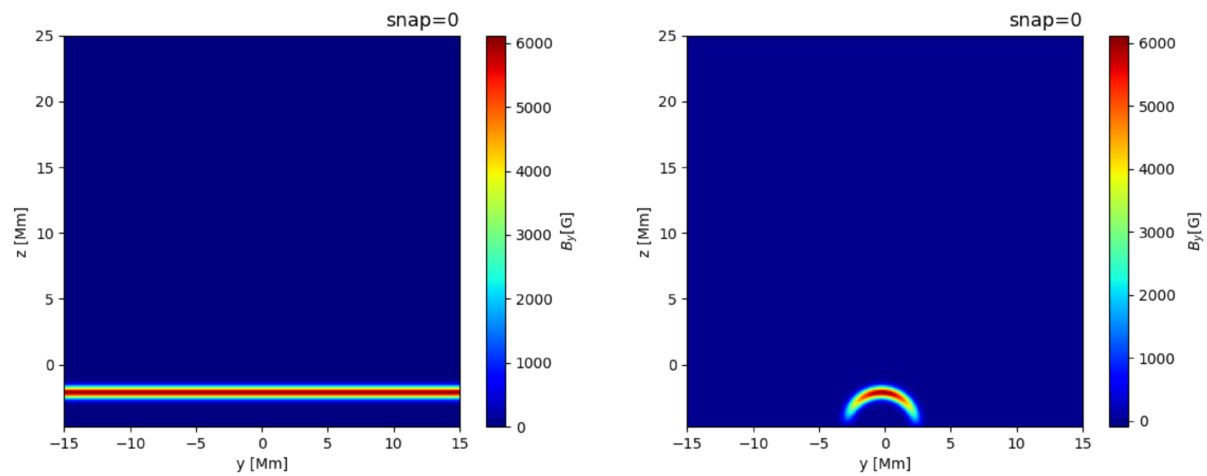

Figure 4.16: On the left side we see the B_y of the horizontal flux tube at $t = 0$, while on the right side the B_y of the toroidal at the same time. These two plots show how the flux tubes's magnetic field looks like when we first place them on the computational box.

Another important difference, which is also a subject we examine in this work, is the twist parameter α. We chose to examine only two different values of the α parameter to capture the cases of highly twisted ($\alpha = 0.4$) and weakly twisted ($\alpha = 0.1$) field lines. This parameter is inputted as an initial condition in each simulation.

In the next chapter we make a comparison between the two different flux tube geometries, to further investigate whether a horizontal or a toroidal flux tube carries more axial flux in the solar atmosphere. At the same time we also distinguish two cases with different amount of field line twist, highly twisted ($\alpha = 0.4$) and weakly twisted ($\alpha = 0.1$), and we contrast the amount of axial flux they are able to transport upwards.

Results for $\alpha = 0.4$

5.1 Introduction

In this chapter we present the results from the horizontal and the toroidal flux tube experiments. The initial conditions are the same for both experiments and the twist is set to $\alpha = 0.4$. The weakly twisted case (i.e. $\alpha = 0.1$) will be presented in the next chapter.

5.2 Twist $\alpha = 0.4$

The emergence phase was extensively discussed in the previous chapter. In this chapter we analyze the results when the magnetic flux has already emerged in both experiments. We first show a top view of the z component of the magnetic field at the photospheric level. Similar observations of the Sun's photospheric magnetic field are made using magnetograms, such as those produced by HMI instrument onboard of the Solar Dynamics Observatory (SDO) (Jørgen Schou et al. 2012), (Wachter et al. 2012), (P H Scherrer, Jesper Schou, et al. 2012; P H Scherrer, R S Bogart, et al. 1995). During the flux emergence for both simulations a bipolar region is formed as shown in Figure(5.1) and (5.2) respectively. The black and white areas shown in those plots are regions of opposite polarity where magnetic flux either penetrates the surface upwards or downwards allowing for plasma to flow. This make the simulation pictures very similar to those of real sunspots in the solar surface. Those plots have a series of snapshots that are taken throughout the whole simulation. This is deliberate to illustrate the dynamics of the footpoints of each tube. As we can see comparing the two figures, in the case of the horizontal flux tube, its footpoints seem to drift apart as time goes on and they continue to do so even towards the end. This however is not the case for the toroidal flux tube. In the beginning, the footpoints drift apart at the same rate as the ones of the horizontal tube. When the footpoints reach a maximum distance, they maintain that distance through the rest of the simulation. This apparent difference between horizontal and toroidal flux tubes is due to the fact that we set up the toroidal tube in a way that its footpoints are anchored at the bottom boundary, contrary to the horizontal tube which is parallel to the surface and its length is infinite. As we can also see through the simulation each sunspot exhibits a rotating motion which forms a sigmoid shape along the polarity inversion line (PIL). The sigmoid that is created here is common feature of observations (McKenzie and Canfield 2008). This structure maintains roughly its shape even during the later stages of the simulation.

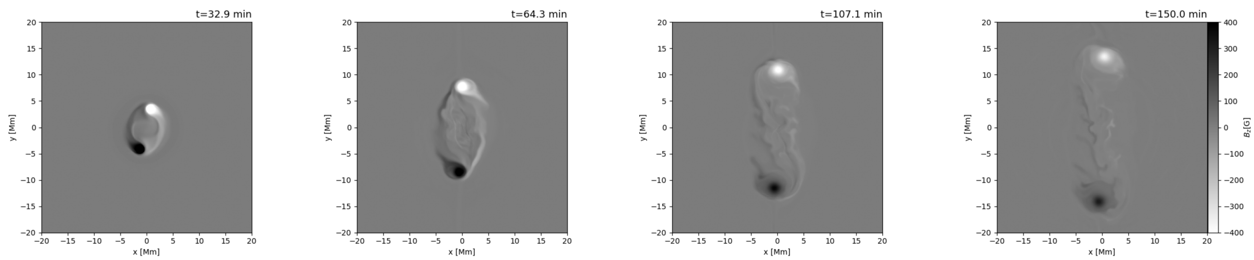

Figure 5.1: Sunspot formation from the horizontal flux tube with twist $\alpha = 0.4$. B_z viewed from the top of the computational box. We can see that the sunspots drift apart indefinitely.

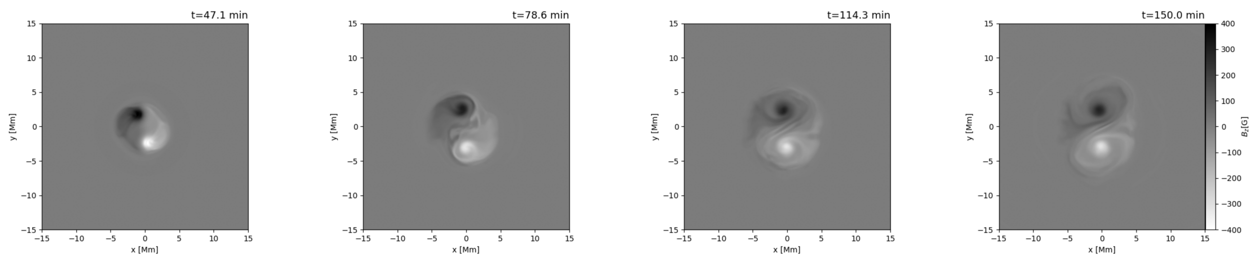

Figure 5.2: Sunspot formation from the toroidal flux tube with twist $\alpha = 0.4$. B_z viewed from the top of the computational box. The sunspots start drifting apart at the beginning of the emergence, but they later stop at a fixed distance.

To illustrate better the footpoint separation we plot in Figure(5.3) the footpoint distance with time. By observing the behavior of the footpoint separation distance we see the that in the horizontal case the footpoints get separated indefinitely while in the toroidal tube case the footpoint separation distance reaches a plateau. The red dashed vertical line on the second plot of Figure(5.3) signifies the maximum distance between the footpoints. As we expect this distance is twice the tube's length $d = 2L$ (Alan William Hood et al. 2009). At each point in time the footpoint distance is calculated with equation,

$$d = \sqrt{(x_2 - x_1)^2 + (y_2 - y_1)^2} \tag{5.1}$$

where the two footpoints of opposite polarity are at coordinates (x_1, y_1) and (x_2, y_2).

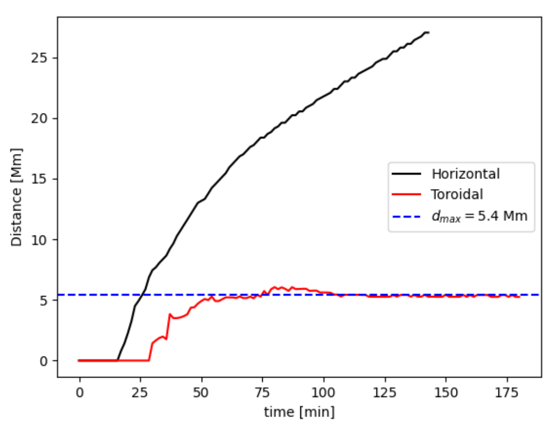

Figure 5.3: Footpoint separation for both horizontal and toroidal flux tubes. The maximum separation distance for the toroidal is shown in the dashed blue line at $d_{max} = 5.4$ Mm.

As we described in chapter 4 the inclusion of an ambient field will cause a jet formation for both experiments. Therefore we now focus on the thermodynamic properties of the jets. More specifically we take a 2D cut at the x and z directions and zoomed in a surface that spans for 60 Mm in the x-axis and more than 60 Mm in the z-axis, which represents the vertical height. What is shown in the both Figure(5.4) and (5.5) is the temperature before and throughout an eruption-driven jet known as blowout jet. In both horizontal and toroidal case we distinguish the formation of a flux-rope structure which is blown away during the eruptive phase. This is also clearly indicated by the magnetic field lines surrounding the plasma. The jet that can be seen is formed in the early stages of flux emergence and is present throughout the simulation. After both tubes emerge and create a standard jet, the horizontal tube experiences two blowout eruptions while the toroidal five. Here we only show one from each since it is indicative of all the eruptions that occur after the blowout jet is formed. This apparent difference in the quantity of eruptions however is important in understanding the amount of flux that each tube is able to transport upwards.

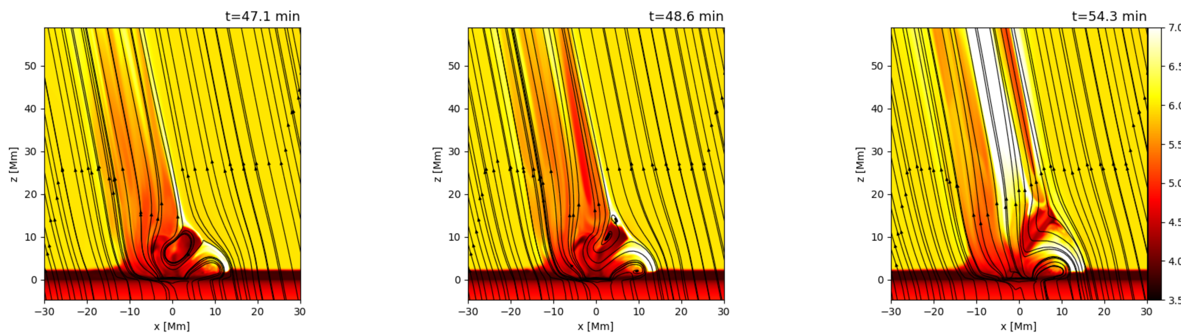

Figure 5.4: Logarithm of temperature viewed from the side of the computational box in a cut at the $x - z$ sub-plane. This sequence is taken during the first eruption of the horizontal tube with $\alpha = 0.4$ twist. The black streamlines show the magnetic field lines at the same time as the temperature in the background. We can see that during the eruption there is an increase in the temperature at the jet's spire due to the violent eruption of hot plasma, as well as a distinct structure that leaves from the top of the flare loop.

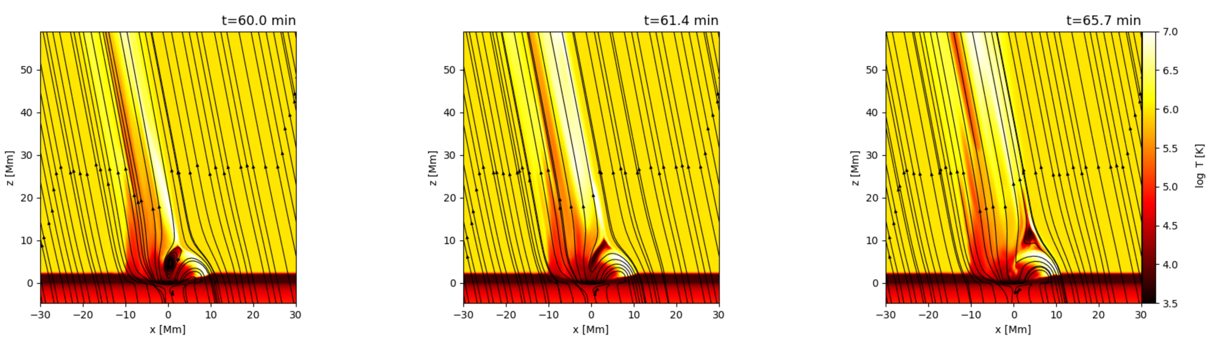

Figure 5.5: Logarithm of temperature viewed from the side of the computational box in a cut at the $x - z$ sub-plane. This sequence is taken during the first eruption of the toroidal tube with $\alpha = 0.4$ twist. The black streamlines show the magnetic field lines at the same time as the temperature in the background. We can see that during the eruption there is an increase in the temperature at the jet's spire due to the violent eruption of hot plasma, accompanied by a distinct structure leaving from the flare loop.

Using similar techniques we present the same plots (i.e. $x - z$ cut, same axis limits) in Figure(5.6) and (5.7) that show the density as it evolves during an eruption. In comparison with the plots for the temperature, the density seems to be higher in the same areas that the plasma is hot, as well as the areas where plasma is ejected from the main structure. Once the eruption is finished plasma continuous to move upwards this time however along the spine of the standard jet. Then, a new flux rope is formed which explodes leading to a second blowout. Of course the plasma density that the standard jet is able to transport is much smaller than that of an eruptive event. This process stops for the horizontal after two eruptions while for the toroidal after five.

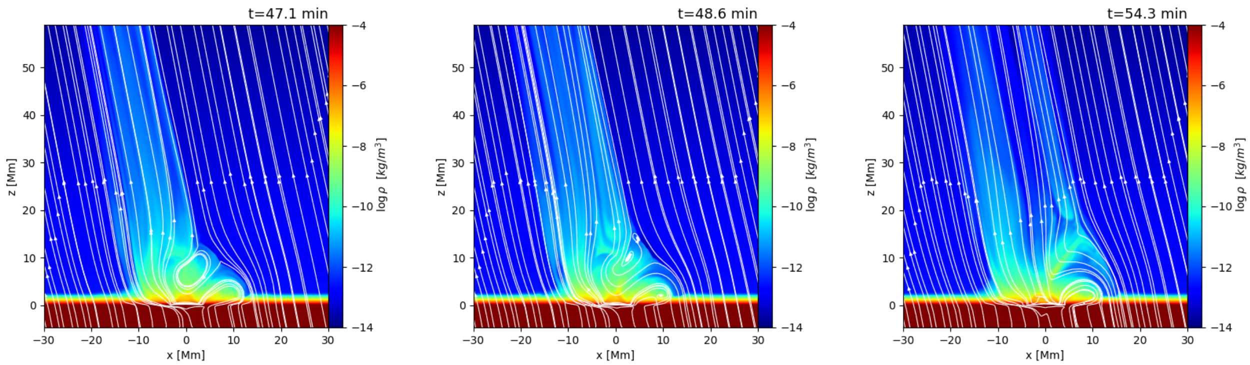

Figure 5.6: Logarithm of density viewed from the side of the computational box in a cut at the $x - z$ sub-plane. This sequence is taken during the first eruption of the horizontal tube with $\alpha = 0.4$ twist. The white streamlines show the magnetic field lines at the same time as the density in the background. We can see that during the eruption there is an increase in the density at the jet's spire due to the violent eruption of dense plasma, along with an increase of density above the flare loop which is the plasma that leaves the main structure.

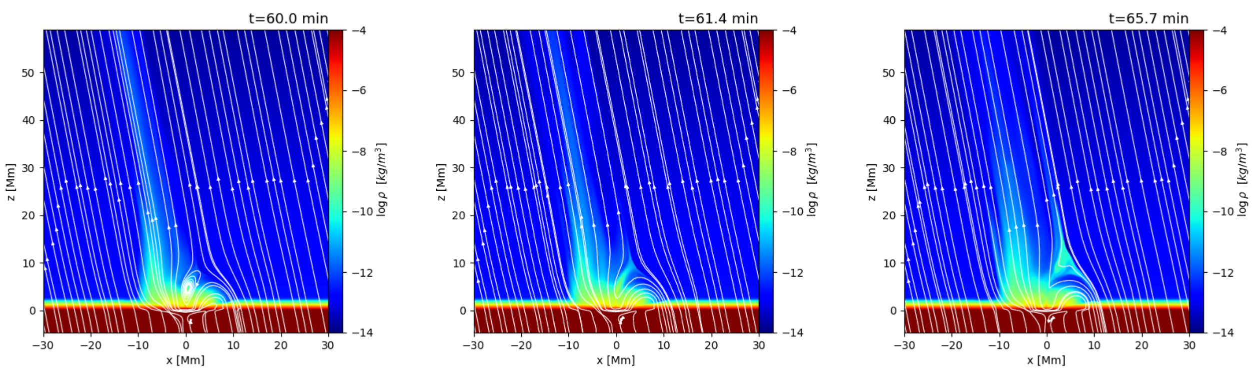

Figure 5.7: Logarithm of density viewed from the side of the computational box in a cut at the $x - z$ sub-plane. This sequence is taken during the first eruption of the toroidal tube with $\alpha = 0.4$ twist. The white streamlines show the magnetic field lines at the same time as the density in the background. We can see that during the eruption there is an increase in the density at the jet's spire due to the violent eruption of dense plasma, along with an increase of density above the flare loop which is the plasma that leaves the main structure.

Finally, in Figure(5.8) and (5.9) we plot the vertical velocity at the $x-z$ mid-plane to illustrate the violent ejection of plasma during eruptions. Both the plots for the horizontal and the toroidal tubes are centered around the time of a blow out. Before the eruptive-driven jet a standard jet is formed as we explained in chapter 4. During the interaction between the emerging field and the ambient field a current sheet is formed leading to reconnection which accelerate particles upwards along the open field lines of the ambient field with velocities on the order of 100 km/s. During the blowout phase plasma is expelled along the whole body of the jet increasing the width of the jet. These series of plots might be even more helpful in showcasing an eruption since during a blowout particles are accelerated and their much larger speed can be compared more clearly with the surrounding plasma velocity. We can clearly see an increase in the velocity at the tube areas that erupt as well as throughout the whole length of the jet as plasma travels trough the corona.

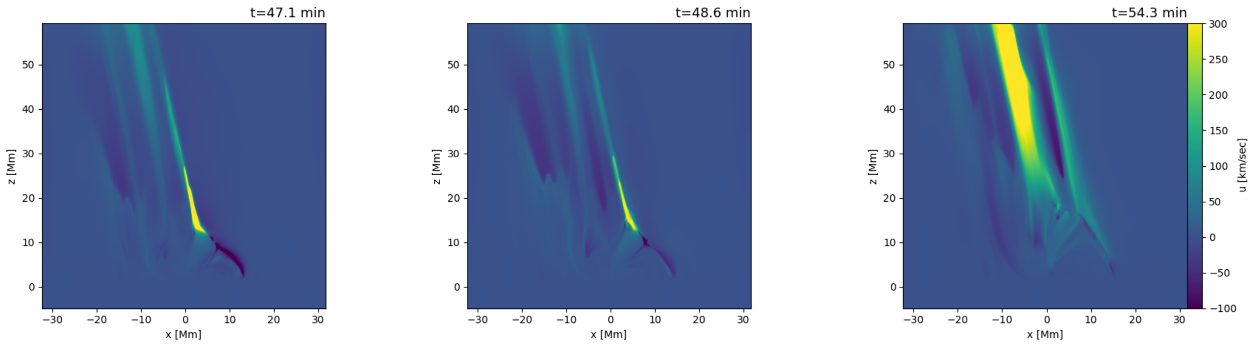

Figure 5.8: V_z viewed from the side of the computational box at a $x - z$ sub-plane cut. This sequence is taken during the first eruption of the horizontal flux tube with $\alpha = 0.4$ twist. We can see that during the eruption there is an increase in the velocity throughout the jet's spire since material is accelerated while leaving the main structure.

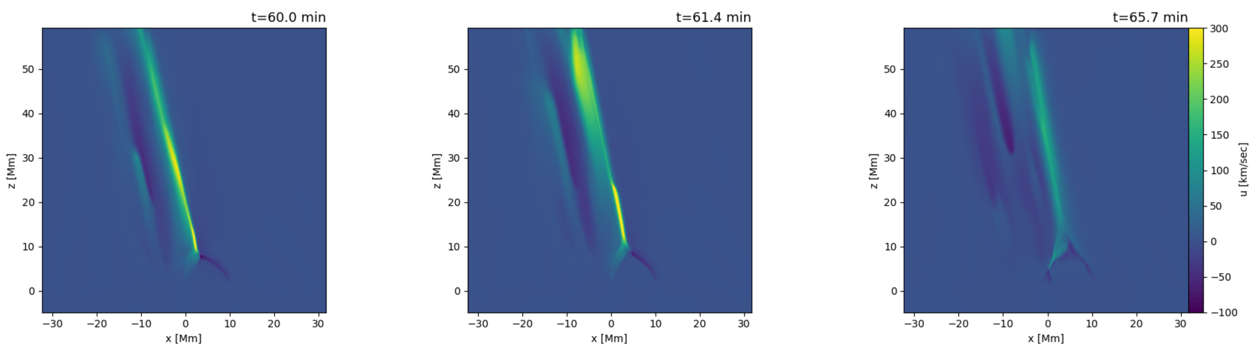

Figure 5.9: V_z viewed from the side of the computational box at a $x - z$ sub-plane cut. This sequence is taken during the first eruption of the toroidal flux tube with $\alpha = 0.4$ twist. We can see that during the eruption there is an increase in the velocity throughout the jet's spire since material is accelerated while leaving the main structure.

To showcase the number of eruptive events in our experiments we calculate the total kinetic energy above the corona using the expression below,

$$E_{kinetic} = \int \frac{1}{2}\rho u^2 \; dxdydz \tag{5.2}$$

with limits for the z component from $z = 3$ Mm until the end of the box at $z = 60$ Mm. In Figure(5.10) we plot the total kinetic energy on the left side and maximum V_z for $z > 0$ on the right side for both cases.

We start by analyzing the kinetic energy. We see that the horizontal flux tube releases a higher amount of kinetic energy by an order of magnitude as compared to the toroidal flux tube. In addition, the horizontal case results in only two major eruptive events as indicated by the two peaks in the kinetic energy while the toroidal tube results in five major eruptive events as indicated by the five peaks in the kinetic energy.

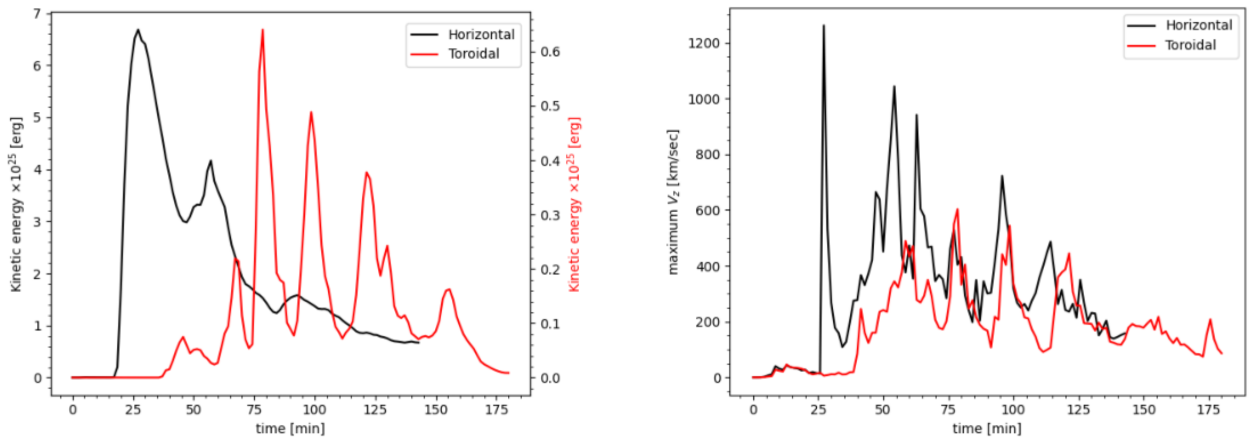

Figure 5.10: On the left panel kinetic energy for horizontal and toroidal flux tubes, where the y axis for the horizontal flux tube is at the left of the plot, while for the toroidal on the right, indicating an order of magnitude difference between their kinetic energy. Right panel shows the maximum V_z through time with peaks corresponding with eruptions where plasma is accelerated upwards.

If we integrate the kinetic energy with time we calculate that the horizontal tube releases is $E_{kinetic} = 1.74 \cdot 10^{29}$ ergs for the whole simulations while the toroidal tube releases $E_{kinetic} = 1.22 \cdot 10^{28}$ ergs. Regardless of the fact that the toroidal has three more eruptions, the total kinetic energy released by the horizontal is an order of magnitude higher. Both those values are comparable to that of an observed solar flare (Kontar et al. 2017), (Benz 2017), (A. Emslie et al. 2012).

Even though the kinetic energy identifies which case releases more energy its not very effective to clearly identify the eruptions for the horizontal case. For that reason we also depict the maximum vertical velocity in Figure(5.10). For the horizontal case we see more clearly a variety of events. The first peak at a time of $t = 25$ minutes reaching velocity of 1200 km/s is associated with the creation and acceleration of plasmoids that are being violently ejected from the current sheet created between the emerging field and the ambient field. This particular phenomena and its mechanism is outside the scope of this thesis. The second peak at roughly $t = 55$ minutes corresponds to the standard jet formation and the next two distinct peaks at $t = 60$ minutes and $t = 95$ minutes correspond to the two eruptive driven jets. The toroidal tube case exhibit a behavior similar to the kinetic energy with all major peaks in the maximum velocity corresponding with peaks of the kinetic energy.

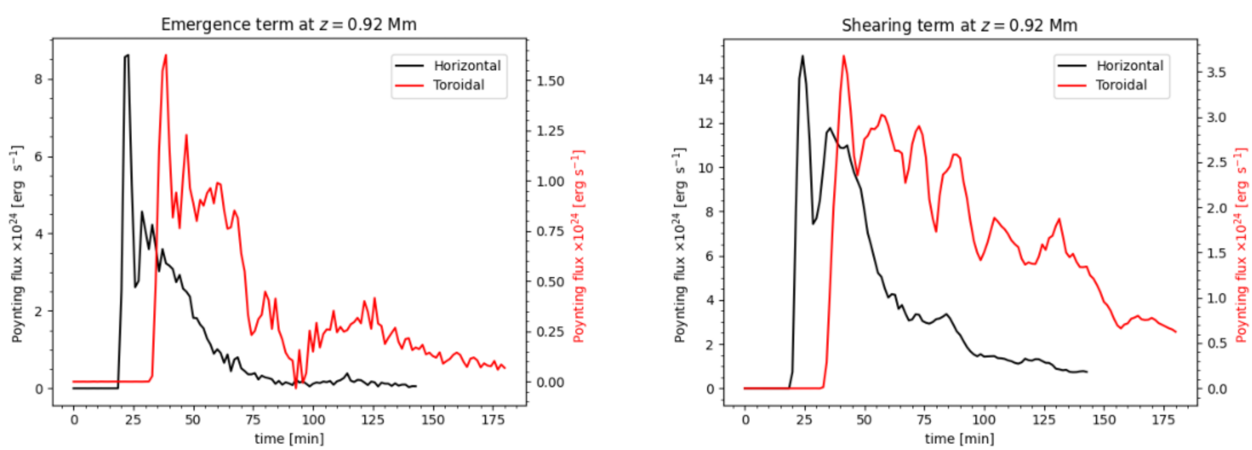

Figure 5.11: Temporal evolution of the emergence and Shearing terms of the Poynting flux for horizontal and toroidal flux tubes at a height of $z = 0.92$ Mm, deep in the photosphere.

Poynting flux is the amount of electromagnetic flux that passes through a surface. In flux emergence experiments it can be used also to identify eruptive events. A way we can visualize that is by isolating the emergence and shearing terms of the Poynting flux and plot the against time. The emergence term can be written as follows,

$$S_{em} = \frac{1}{4\pi} \iint u_z (B_x^2 + B_y^2)\ dxdy \tag{5.3}$$

and the shearing term expressed as,

$$S_{sh} = -\frac{1}{4\pi} \iint B_z (u_x B_x + u_y B_y)\ dxdy \tag{5.4}$$

Figure(5.11) shows time series of the emergence and shearing terms for both horizontal and toroidal flux tubes deep in the photosphere at a height of $z = 0.92$ Mm. On the left side we have the emergence term which is the part of flux representing the direct emergence of the magnetic field. As the emergence process begins we see that for both flux tubes the term increases. Then for the rest of the simulation, flux is no longer transported as a result of the magnetic field's emergence and so the term slowly diminishes. The emergence term of both tubes have the same order of magnitude, however in the horizontal case the term has higher values. On the right side of Figure(5.11) we have the shearing term which represents the flux due to horizontal motions. Again there is an increase at the beginning of the simulation of both tubes which is expected since the emerging flux tube also expands in the direction the polarity inversion line (PIL), so part of the flux is redirected towards the shearing motion since plasma is pushed sideways along the PIL and towards the x-direction. Afterwards the term for both tubes start to decrease due to the fact that the expansion of the field becomes less prominent at the later stage of the simulation. Once again the values the shearing term takes are larger for the horizontal case than the toroidal.

If we focus on the right panel of Figure(5.11) we can that the shearing term, especially in the toroidal case, has some spikes. This rise and fall of the shearing term can be associated with the eruptions of the flux tube. Specifically, at the term's local minima is when an eruption takes place because Poynting flux is no longer used for the tube's shearing motion, instead it takes part in the eruption. So in the beginning, after the shearing term has increased it drops as a result of the standard jet formation. For the toroidal tube the next five local minima coincide with an eruption. The horizontal case has only two local minima on the shearing term, corresponding to both eruptions. Eruptions can also be pinpointed at the plot of the emergence term. Unlike the shearing term, during an eruption the emergence term peaks momentarily since the upwards movement of plasma reflects on the emergence term. On the left side of Figure(5.11) we see that the toroidal again has five local maxima while the horizontal has two faint surges at the time of its eruptions.

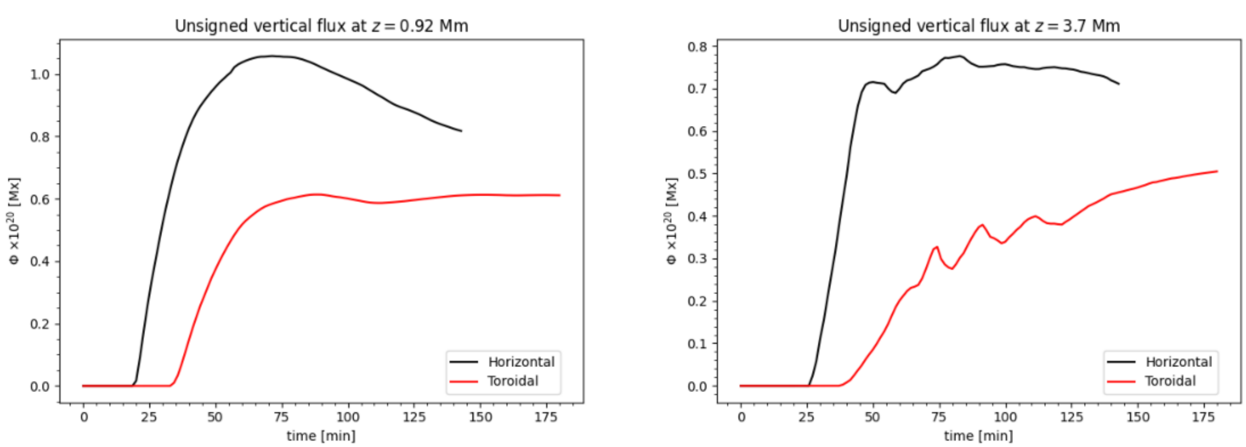

Figure 5.12: Unsigned vertical magnetic flux Φ at the photosphere in 0.92 Mm and at the corona in 3.7 Mm respectively.

In this Figure(5.12) we can see the total vertical flux that runs through a specific height (i.e. 0.92 Mm and 3.7 Mm) throughout the whole simulation. In order to calculate the unsigned magnetic flux that passes through a specific $x - y$ surface we evaluate the following integral and plot it against time for two different heights.

$$\Phi_{z=0.92,3.7Mm} = \iint |B_z| dxdy \tag{5.5}$$

Inside the photosphere the vertical flux increases rapidly for both tubes until it reaches a maximum around $t = 65$ minutes and $t = 85$ minutes for horizontal and toroidal case respectively. For the horizontal tube the flux starts to drop afterwards possibly due to the eruptions. However other proposals explain the decrease due to flux cancellation on the photospheric level (Petros Syntelis et al. 2015). The toroidal tube on the other hand is able to maintain its flux throughout its evolution. Nevertheless it doesn't transport as much flux as the horizontal in the photosphere. Obviously as we examine higher altitudes the total flux that runs through a surface decreases, since the flux that emerges does not exclusively move upwards but also diffuses at different directions. This can be seen in the right side of Figure(5.12) where it shows the vertical flux that runs through a surface in the lower corona at $z = 3.7$ Mm. In comparison to the left picture both tubes have a smaller maximum of vertical flux as well as the toroidal transporting less flux in the corona than the horizontal.

Magnetic flux emergence is commonly associated with strong magnetic field concentrations at the photosphere, particularly in regions known as active regions (ARs). These regions, depending on the characteristics of the magnetic field lines, can give rise to flaring events or even more violent eruptions, such as coronal mass ejections (CMEs). A key feature of these eruptive phenomena is their dependence on twisted magnetic field lines. Twist is a crucial precondition for many of these events, as it facilitates magnetic reconnection, a process that converts magnetic energy into kinetic and thermal energy. One way to quantify the flux of the twisted magnetic field is by measuring the axial flux (Φ_y) in the upper atmosphere using the following expression.

$$\Phi_y = \iint B_y \; dx \; dz \tag{5.6}$$

The axial flux represents the amount of the y-component of the magnetic field passing through a plane perpendicular to the solar surface. Since not all of the initial axial flux will emerge, determining the percentage that does emerge can help identify which of the two cases under study exhibits a higher degree of twisted field lines. This, in turn, provides insight into the connection between magnetic twist and the observed eruptions.

To analyze this, we first plot the axial flux (Φ_y) as a function of time. Two distinct curves are generated: one representing the flux that emerges through the photosphere ("atm"), and the other representing the flux that remains below the surface ("int"). This process is applied to both a horizontal and a toroidal flux tube. In Figure(5.13), the black lines correspond to the horizontal flux tube, while the red lines correspond to the toroidal flux tube.

More specifically, for the flux that remains beneath the photosphere, denoted as "int" for both the horizontal and toroidal flux tubes, we calculate the relative flux over time. At each time step, the flux value is normalized by dividing it by the initial flux value at time $t = 0$. This normalization explains why the flux values for both tubes start at 100% on the y-axis, since no flux has emerged at the beginning of the simulation.

In the case of the flux that successfully emerges beyond the photosphere, denoted by "atm", we calculated it in a similar way but also subtracted from each value the flux at the photospheric level at time $t = 0$ and then divide it with the value of the flux at the beginning of the simulation. Of course all those values are normalized at 100%.

As shown in Figure(5.13), the black solid line represents the flux that emerges through the photosphere into the solar atmosphere for the horizontal flux tube. The flux peaks early in the simulation, after which the rate of emergence slows down. Over time, the emergence stabilizes, reaching approximately 60% of the initial axial flux.

In contrast, the toroidal flux tube begins to emerge at a slower rate and peaks much later than the horizontal tube. However, while the flux emergence rate for the horizontal tube decreases, the toroidal tube continues to increase its axial flux budget into the upper atmosphere. By the end of the simulation, the toroidal flux tube reaches a plateau at approximately 80% of the initial axial flux.

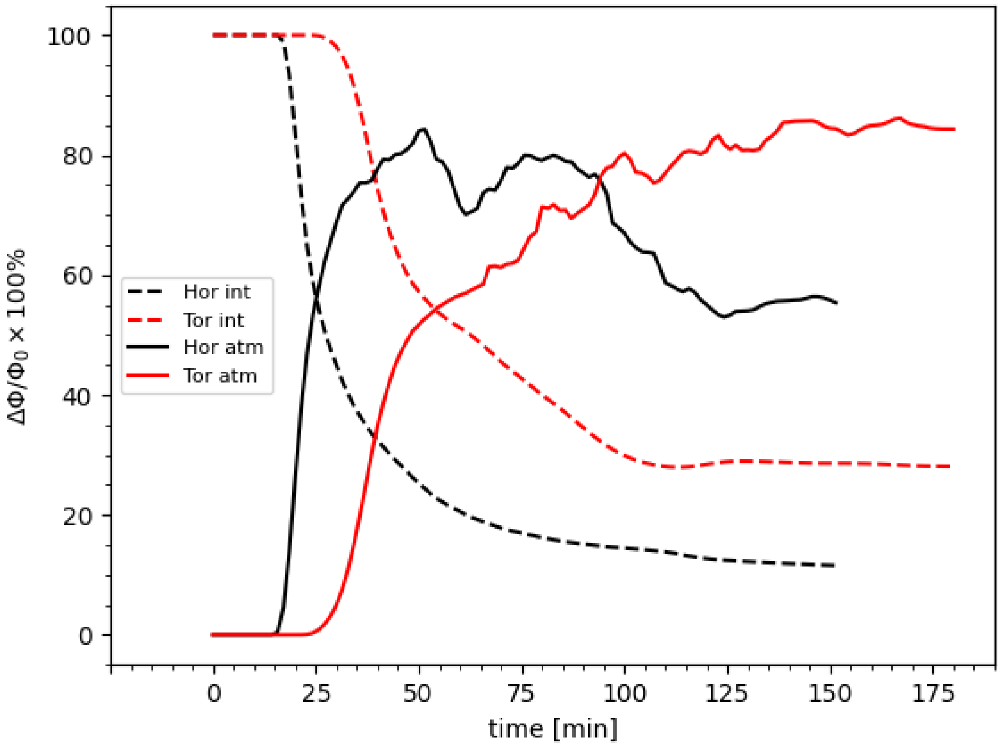

Figure 5.13: Percentage of axial flux Φ_y , that passes through the $x - z$ surface for horizontal and toroidal flux tubes with $\alpha = 0.4$ twists. Denoted by "int" is the total axial flux calculated beneath the photosphere through time, while "atm" refers to the total axial flux above the photosphere.

Now, we focus on the two dashed lines of Figure(5.13). Both dashed lines represent the flux that remains beneath the photosphere. Initially, both lines start at 100% of the flux, as this is where the flux tubes are located at the beginning of the simulation. As time progresses and both the horizontal and toroidal flux tubes emerge through the photosphere, the percentage of flux beneath the surface decreases. The horizontal tube ends with only about 10% of its original flux remaining below the photosphere, while the toroidal tube retains approximately 30%.

By looking at Figure(5.13) one would naively expect the total flux beneath and above the photosphere to add up to 100% for both cases. This however is not the case since the percentage of flux we measure is merely the flux that goes through the surface created along the y axis and not the total flux Φ. So during the emergence process part of Φ might be transported through a different surface which will eventually show up in the total percentage. Equivalently, flux from a different surface can be injected into our calculation creating the illusion that more flux is carried through the photosphere than what it was originally beneath it.

Overall the importance of axial flux emerging in the solar atmosphere is a prerequisite for eruptive events. The percentage of axial flux that does emerge, impacts the ability of the flux tube to create erupting flux ropes. For the horizontal flux tube the axial flux decreases after each eruption and without further flux emergence and no other mechanism to twist the field lines any further, no more eruption-driven jets can be produced. The toroidal flux tube on the other hand creates axial flux with a different mechanism even after the end of its emergence. The reason behind this could be the rotational motion of the sunspots. The toroidal tube's footpoints rotate causing the magnetic field to untwist which in turn forces part of the azimuthal flux to be redirected in the axial direction (Z. Sturrock et al. 2015). This could also explain why we were able to observe three more eruptions from the toroidal while at the same time it maintains a high percentage of axial flux even at the end of the simulation.

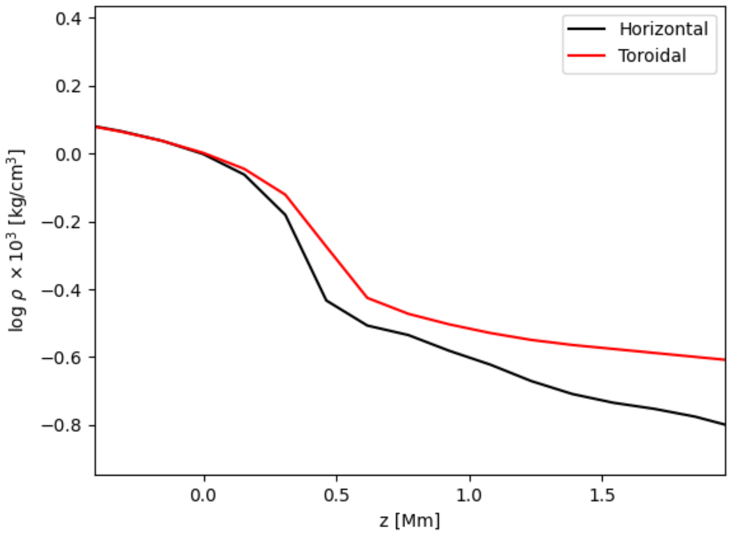

Figure 5.14: The logarithm of density plotted over height, at , which shows that the horizontal tube is less dense than the toroidal in the early stages of emergence, at a time of $t = 28$ minutes.

The horizontal tube transports overall more energy in the solar atmosphere, even with fewer energetic phenomena than the toroidal. This difference has its roots in the geometry of each tube and the subsequent forces that act upon the plasma that they enclose. Regarding the rates at which each tube emerges, the left panel of Figure(5.14) can provide an answer. We have plotted the logarithm of the density at the center of each flux tube over height. What we see is that even though both flux tubes start with the same density deficit, the horizontal soon becomes lighter as it moves upwards. So when the buoyancy force acts upon it, the tube rises faster than the toroidal which has denser plasma.

Another important point is the discrepancy regarding the transported axial flux which can be explained by considering the magnetic tension of each tube's field lines. The expression of the Lorentz force in equation (5.7) can be split into two terms, one being the magnetic pressure (5.8) and the other the tension force (5.9).

$$F_L = -\nabla\left(\frac{B^2}{2\mu_0}\right) + \frac{(B \cdot \nabla)}{\mu_0}\ B \tag{5.7}$$

$$P_m = \nabla\left(\frac{B^2}{2\mu_0}\right) \tag{5.8}$$

$$T_m = \frac{(B \cdot \nabla)}{\mu_0}\ B \tag{5.9}$$

$$T_{m,z} = \frac{1}{\mu_0}\big(B_x\partial_x + B_y\partial_y + B_z\partial_z\big)\ B_z \tag{5.10}$$

Since for our analysis we want the upward force we focus on the z component of the magnetic tension force. We can calculate it using the equation(5.10) and plot it over height in the beginning of the simulation at $t = 4$ minutes, as shown at the left side of Figure(5.15). However, these forces evolve through time, so we also calculated the difference between the maximum and minimum values of the z component at every point in time. Right panel of Figure(5.15) shows that difference through time for both cases. Magnetic tension is the force that tries to straighten curved field lines. Below the center of the tube the force points upwards, thus it is positive, and above the center it is negative. Initially the negative part is stronger not allowing the tube to rise easily. However as it rises the magnetic field expands making the upper part less curved which decreases the negative component of the tension.

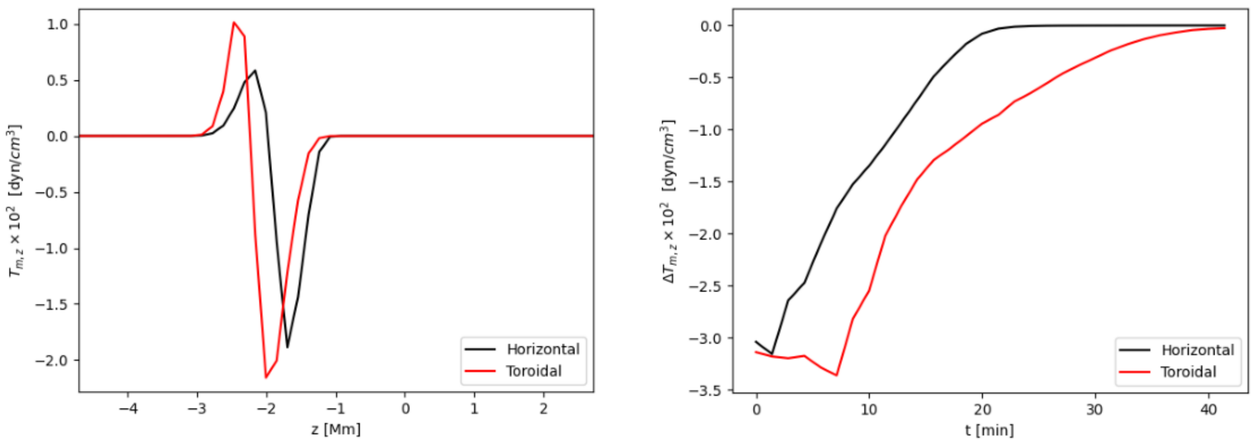

Figure 5.15: Left panel shows the magnetic tension on the z-axis through height for both tubes, in the beginning of the simulation at around $t = 4$ minutes. The negative values are due to the tension force on the top of the flux tube pointing downwards, while the positive values represent the tension that supports the bottom part of the flux tube. Right panel shows the net magnetic tension of the field lines of each tube as it evolves through time. The fact that magnetic tension difference is higher in the horizontal case, illustrates the horizontal tube's ability to hold more plasma and transport it upwards.

So over time the net tension approaches zero and making the tube easier to rise. As shown in the plot, for the horizontal case magnetic tension approaches and reaches zero much faster than the toroidal, which explains why the horizontal tube carries more axial flux in the upper atmosphere. The different magnetic tension of each flux tube is a consequence of its geometry. In the toroidal case, the tube will be heavily curved, and so will the field lines that wrap around it. These twisted field lines put more tension on the tube than the field lines in the horizontal case.

In conclusion, it seems that the multitude eruptions exhibited by the toroidal flux tube cannot overshadow the less frequent, yet more energetic eruptions of the horizontal tube. This means that since eruptive events such as flares and CMEs require huge amounts of energy, a geometry of a horizontal flux tube is more able to provide that energy than a toroidal geometry.

Results for $\alpha = 0.1$

6.1 Twist $\alpha = 0.1$

As we mentioned in Chapter 4, this work will be repeated for a different value of the twist parameter α. This time we assign the value of $\alpha = 0.1$ while maintaining the same values for the magnetic field, the atmosphere stratification and every other parameter for both the horizontal and the toroidal flux tubes. It is known in the bibliography that a weakly twisted flux tube ($\alpha = 0.1$) will not emerge as efficiently as a strongly twisted one ($\alpha = 0.4$). This is mainly due to the fact that high twist helps the emergence process by making the flux tube more coherent (M. Murray et al. 2006), (P. Syntelis, V. Archontis, and A. Hood 2019), (Martínez-Sykora, Hansteen, and Carlsson 2008). This is confirmed in the following results of this chapter.

In contrast to the highly twisted flux tubes, where we had two and five eruptions for the horizontal and the toroidal respectively, in the case of the weakly twisted tubes we observe one eruption for the horizontal while the toroidal flux tube does not erupt. This is expected since the flux tube is deformed as it tries to penetrate the lower photosphere and is flattened out without being able to create twisted flux ropes that can lead to efficient eruption-driven jets as in the high twisted case.

First, we begin by showing the evolution of the emergence process as viewed from the top of the computational box. This is done by plotting a series of snapshots of the z component of the magnetic field and focusing on the $x - y$ plane vertically from above. Figure(6.1) has three pictures of the B_z from the top throughout a part of the simulation. Even though the simulation has run for a little longer, we chose to not show any plots from later times since the flux tube effectively breaks down, and the emergence process no longer has any significance. Nevertheless, in Figure(6.1) we can see the separation of the tubes footpoints and the bipolar region that is created.

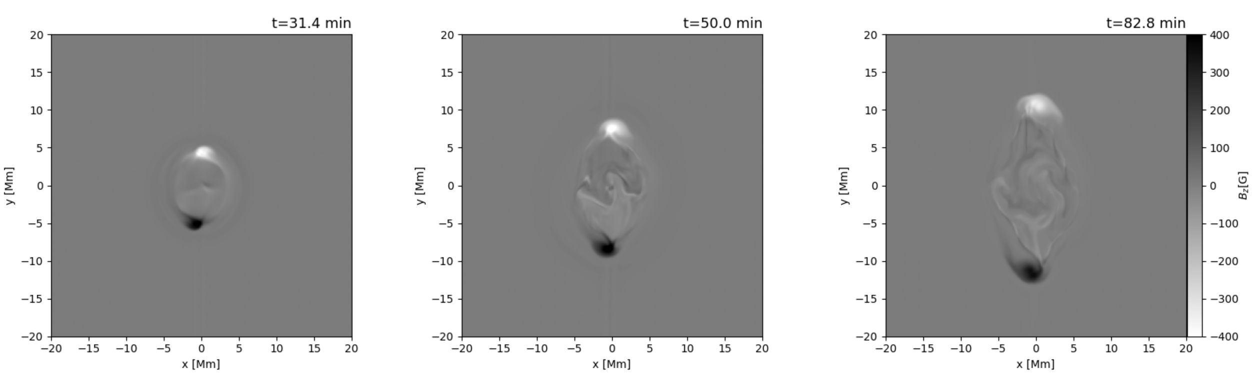

Figure 6.1: z component of the magnetic field viewed from the top that shows the evolution of the horizontal flux tube with $\alpha = 0.1$ twist, throughout the simulation. We can see that as time passes the sunspots drift apart indefinitely.

The evolution of the emergence process of those two tube geometries also differ significantly from each other. As we saw in the previous figure, the footpoints of the horizontal tube spread indefinitely since the tube is placed parallel to the solar surface with both of its ends extending on either side of the computational box. On the contrary, the toroidal tube is initially placed with its two footpoints anchored in the solar interior. This means that the footpoints cannot spread at all and throughout the simulation they do not move from the two points where they were initially placed. This is shown very clearly in Figure(6.2) where after the emergence in the early stages of the simulation, the bipolar region seems to remain unchanged as time goes by. Just like in the case of the flux tube with twist $\alpha = 0.4$, we also have the maximum distance of the footpoints at two times the length of the flux tube, $d = 2L$.

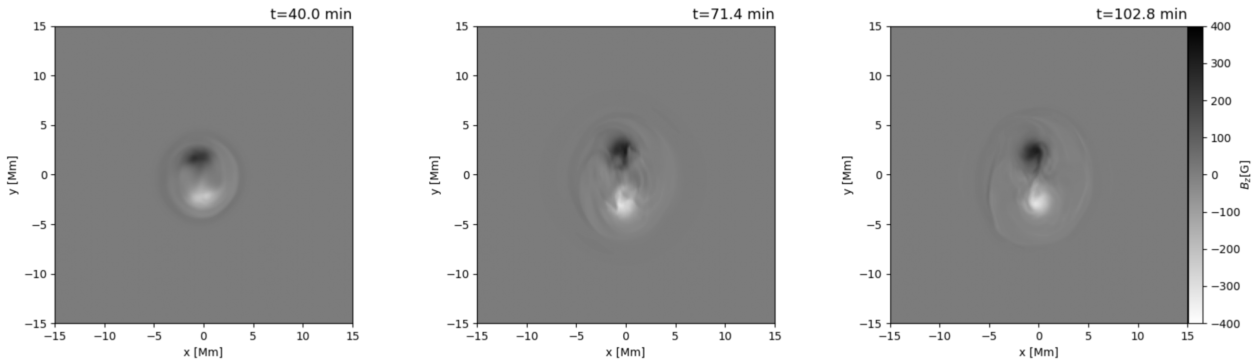

Figure 6.2: z component of the magnetic field viewed from the top that shows the evolution of the toroidal flux tube with $\alpha = 0.1$ twist, throughout the simulation. In this case the sunspots drift apart in the beginning of the emergence and then stop at a fixed point for the rest of the magnetic structure's evolution.

Then, we show four snapshots throughout the only eruption of the horizontal flux tube in Figure(6.3). These plots show the temperature gradient as we view it from the side of the computational box. This means that we see the $x - z$ surface. These four consecutive snapshots show the eruption process as hot plasma seems to depart from the main structure and follows the path of the blowout jet into the corona.

On the other hand, since there is no eruption in the toroidal tube, we can only show a series of snapshots in Figure(6.4) on the late stages of the simulation where the jet has already formed and the flux tube maintains its structure without erupting. What we see in those snapshots is that after the standard jet is formed due to the original emergence of the tube in the corona, no twisted flux rope can be formed which explains the lack of eruptions in the system.

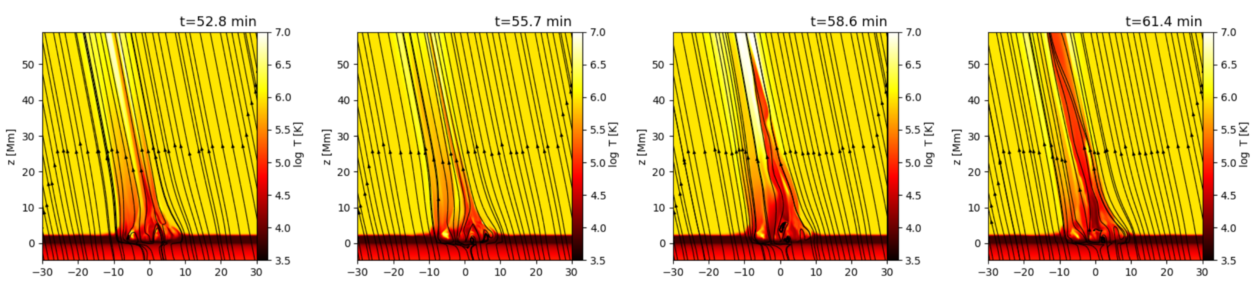

Figure 6.3: Logarithm of temperature viewed from the side of the computational box in a cut at the $x - z$ sub-plane. This sequence is taken during the horizontal tube's only eruption with $\alpha = 0.1$ twist. The black streamlines show the magnetic field lines at the same time as the temperature in the background. We can see that during the eruption there is an increase in the temperature at the jet's spire due to the violent eruption of hot plasma.

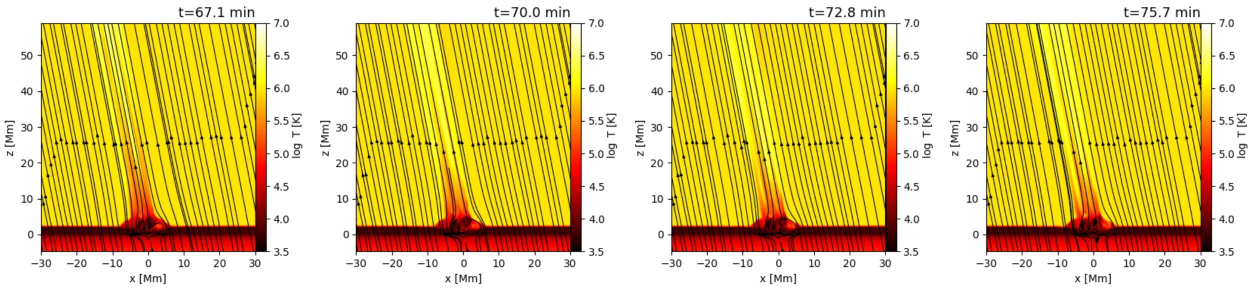

Figure 6.4: Logarithm of temperature viewed from the side of the computational box in a cut at the $x-z$ sub-plane. This sequence is taken in the middle of the simulation and it shows that after the original emergence of the weakly twisted ($\alpha = 0.1$) toroidal tube, it remains inactive without an increase in the temperature at the jet's spire, which would signify an eruption. The black streamlines show the magnetic field lines at the same time as the temperature in the background.

This is done first for the temperature and then in Figure(6.5) and (6.6) for the plasma density. In those figures, we have plotted the logarithm of the values to highlight the difference in magnitude between the surrounding plasma and the flux tube. Similar to the temperature, we view the side of the computational box which is the $x - z$ surface. We can observe a change in the density above the main flux tube structure at the middle picture of Figure(6.5) which is the plasma that blows out of the tube. However when it comes to the toroidal, since there is no eruption, the structure seems to remain unchanged through the whole simulation, and there is no density increase above the tube.

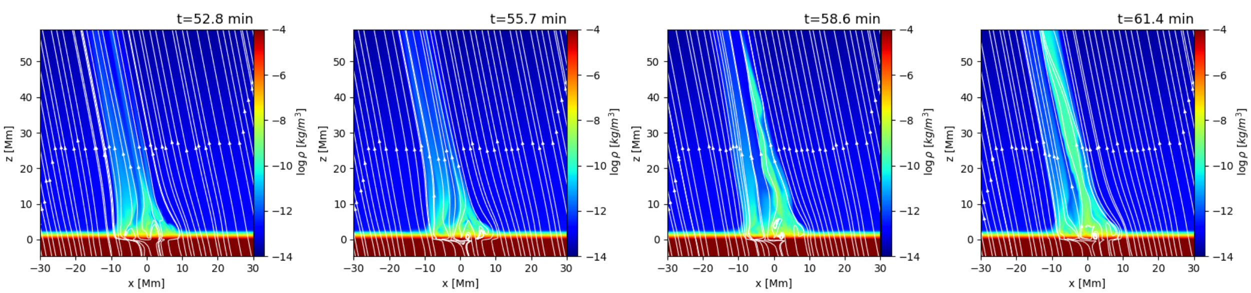

Figure 6.5: Logarithm of density viewed from the side of the computational box in a cut at the $x - z$ sub-plane. This sequence is taken during the horizontal tube's only eruption with $\alpha = 0.1$ twist. The white streamlines show the magnetic field lines at the same time as the density in the background. We can see that during the eruption there is an increase in the density at the jet's spire due to the violent eruption of dense plasma.

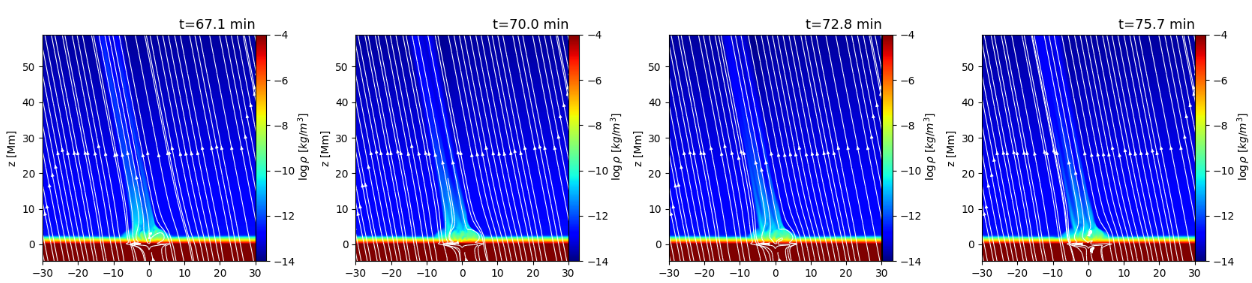

Figure 6.6: Logarithm of density viewed from the side of the computational box in a cut at the $x - z$ sub-plane. This sequence is taken in the middle of the simulation and it shows that after the original emergence of the weakly twisted $\alpha = 0.1$ toroidal tube, it remains inactive without a substantial increase of the density, which would have been evidence for an eruption.

When we look at the $z-$component of velocity in the $x-z$ plane we can see the same features as in the 2D plots of temperature and density. That is the fact that in the case of the horizontal flux tube Figure(6.7) shows how the vertical velocity increases during the tube's only eruption. In Figure(6.8), which shows the emergence of the toroidal flux tube, the standard jet forms the exact way we expect it to by an increase in the vertical velocity around the area of the reconnection with the ambient field. Also the velocity increases through the jet's spire and maintains that formation throughout the simulation without being able to produce a blowout jet.

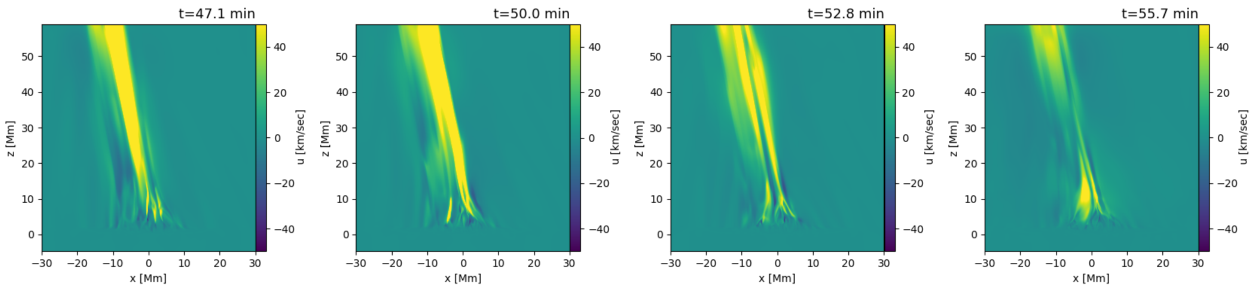

Figure 6.7: V_z viewed from te side of the computational box at a $x-z$ sub-plane cut. The sequence is taken during the only eruption of the horizontal tube with $\alpha = 0.1$ twist. We can see an increase at the velocity through the length of the jet's spire.

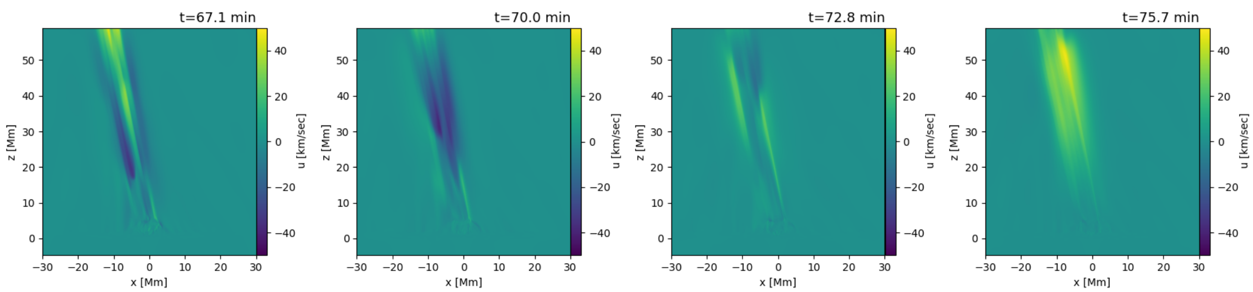

Figure 6.8: V_z viewed from te side of the computational box at a $x-z$ sub-plane cut. This sequence is taken in the middle of the simulation and it shows that after the original emergence of the weakly twisted ($\alpha = 0.1$) toroidal tube, it remains inactive without an increase in the velocity at the jet's spire, which would indicate an eruption.

When we take a closer look at the emergence of the horizontal tube, we see that in the convectively unstable sub-photospheric environment, the magnetic field develops a number of undulations, due to Parker instability, and takes a serpentine-like shape (Strous, Scharmer, and Tarbell 1996), (Etienne Pariat, Masson, and Aulanier 2009). Because of that the flux tube is unstable and rises. The magnetic field then meets the photosphere forming an Ω-loop shape that rises into the corona. Since the flux tube does not emerge as a rigid structure but breaks into smaller parts that emerge independently as separate magnetic lobes, we see the creation of serpentine-like structure. Those smaller structures can come into contact leading to reconnection and eruption. From the contour lines of Figure(6.9) we see how the undulation of the magnetic field creates two distinct lobes that will eventually reconnect and produce the only eruption tha we observe in this case. This however is different to the previous cases where a twisted flux rope created by shearing erupts due to tether cutting or other mechanisms. This behavior of the magnetic field developing undulation is a characteristic of the emergence of a weakly twisted flux tube. In this case, a twist of $\alpha = 0.1$ is small enough to allow the flux tube to develop a serpentine-like shape (Vasilis Archontis and Alan William Hood 2010; Vasilis Archontis and Alan William Hood 2009), (K. Harvey and J. Harvey 1973), (Knizhnik et al. 2021), (Toriumi, Katsukawa, and M. C. Cheung 2017), (Watanabe et al. 2008).

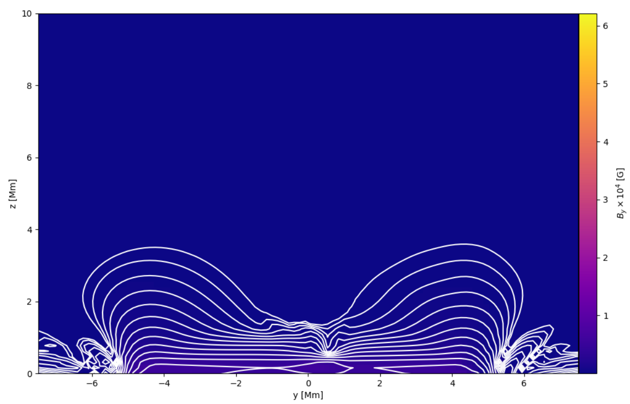

Figure 6.9: Contour lines show the undulation of the magnetic field that creates two opposite magnetic lobes that emerge and reconnect with each other producing an eruption.

Even though the simulation visualizes the whole emergence process along with any possible eruptions, there are still other ways to distinguish eruptive phenomena from unrelated processes that the flux tube may undergo. By calculating the Poynting flux that the magnetic field carries above the photosphere we can capture the ability of each tube to transport energy much clearly. The unsigned vertical flux is the magnetic flux that runs through a horizontal cut of the computational box. In this case we have calculated, using the following equation, the total flux that runs through the $x - y$ plane at the height of the photosphere in $z = 0$ Mm.

$$\Phi_{z=0.92} = \iint |B_z| \, dxdy \tag{6.1}$$

As we see on the left panel of Figure(6.10), we have the plot of the unsigned magnetic flux through the photosphere. The most striking difference is the dominance of the horizontal tube in the total amount of unsigned vertical flux that transports. Of course the emergence of the toroidal tube comes later, and even though the magnitude of vertical flux is the same, it is approximately half of the horizontal at any time. This difference in total amount of vertical flux can provide further evidence as to the toroidal's inactivity.

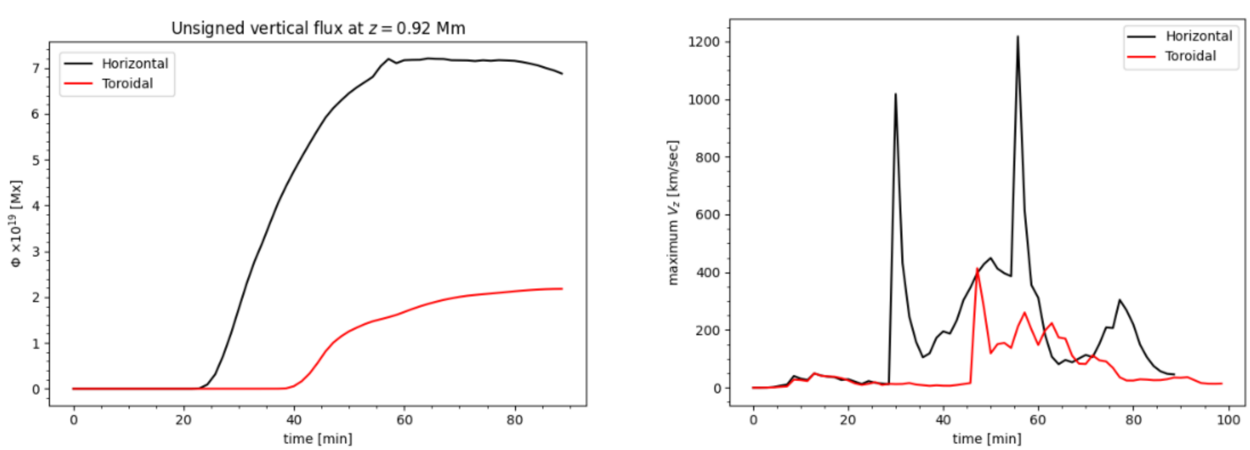

Figure 6.10: Left side of the figure is the unsigned vertical flux for horizontal and toroidal flux tubes, calculated from the middle of the photosphere and above, which means from a height of $z = 0.92$ Mm. On the right side is the temporal evolution of the maximum V_z above the photosphere for both horizontal and toroidal flux tubes

A way to pinpoint eruptions is to show the maximum velocity in the $z-$ axis through time. This is done on the right side of Figure(6.10) for both flux tubes. Starting by focusing on the horizontal tube we see an increase in the maximum V_z at around $t = 30$ minutes into the simulation. This increase corresponds to the plasmoids being violently ejected from the current sheet during reconnection, reaching speeds up to 1200 km/sec. At around $t = 55$ minutes the second spike is due to the only eruption that violently ejects plasma upwards. On the other hand the toroidal case has a relatively stable maximum velocity profile were the values of the speed of the material which moves upwards don't exceed a few hundred kilometers per second. These velocities are nowhere near those of the horizontal and are not fast enough to be in the regime of an eruption.

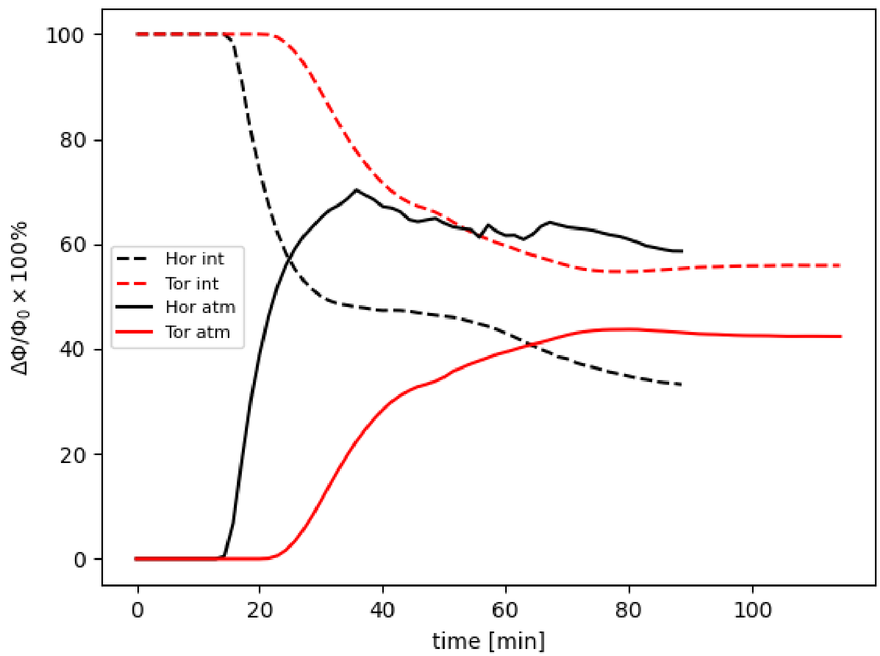

Figure 6.11: Percentage of flux Φ_y that goes through the y surface for horizontal and toroidal flux tubes with $\alpha = 0.1$ twists. Denoted by "int" is the total flux calculated beneath the photosphere through time, while "atm" refers to the total flux above the photosphere.

Figure(6.11) is of significant importance to this work. Much like the equivalent plot for the case of the highly twisted ($\alpha = 0.4$) flux tube, this plot also tells us about the relative percentage of flux that successfully emerges through the photosphere, this time for a weakly twisted ($\alpha = 0.1$) flux tube.

In the same Figure(6.11), we plot two sets of lines. Denoted with black color we have the flux that is due to the y component of the horizontal tube's magnetic field, Φ_y. We calculated Φ_y using the following integral,

$$\Phi_y = \iint B_y \, dxdz \tag{6.2}$$

In order to differentiate between the areas of interest, we calculated the integral of equation(6.2) for two different surfaces, one above the photosphere and one below. The photosphere starts at $z = 0$ Mm. Those two results of Φ_y are plotted and denoted by "int" which corresponds to the flux that exists below the photosphere and by "atm" the flux that rises above it.

The same process is repeated for the toroidal flux tube and this time the quantities plotted in Figure(6.11) are illustrated with black color.

To be more precise we should mention that the dashed black and red lines, that correspond to the flux that stays beneath the photosphere, are created by taking every time of the simulation and dividing its value with the initial value at $t = 0$. A similar procedure is followed for the solid lines that correspond to the flux that emerges above the photosphere. To express the quantities at different time as a percentage of the total flux throughout the whole simulation, we normalize all the values at 100%.

From Figure(6.11) we understand some major differences between the horizontal and the toroidal tube's geometry. Just like in the case of highly twisted flux tubes, the weakly twisted ($\alpha = 0.1$) the horizontal tube also starts the emergence process faster than the toroidal. The flux that emerges above the photosphere reaches a peak of about 70% of the whole flux and it decreases at a slow rate as time goes by, until the end of the simulation where it reaches around 60%.

The weakly twisted toroidal tube has a completely different behavior that the highly twisted. Though it does start emerging at much later than the horizontal, the rate with which flux appears in the photosphere is very slow. Furthermore, after 45 minutes in the simulation the rate of flux emergence decreases even further. Eventually it reaches a peak of around 40% of the total flux and maintains a plateau through the end of the simulation. This behavior is expected since we know that a small twist does not allow the structure to emerge in a uniform and rigid way that will produce eruptive phenomena.

For the emergence of the flux tube it's not only important the flux that is in the photosphere, but also we want to have as little flux as possible to stay behind. If we observe the dashed lines, particularly the black one that describes the magnetic flux that is beneath the photosphere for the horizontal flux tube, we see a few important things. First, the dashed line starts from the highest point in the y-axis. This means that in the beginning the solar interior contains all of the magnetic flux which is reasonable since this is where we initially placed the flux tube. As the horizontal tube emerges, the flux leaving the interior is reflected in the black dashed line that tells us that the percentage of flux decreases beneath the photosphere. At 25 minutes in the simulation, the decrease of the percentage of flux in the interior slows down until reaches around 35% of the original flux by the end of the simulation.

If we now focus on the toroidal flux tube, we observe that the dashed red line starts from 100% of the total flux and the as the toroidal tube emerges, the flux beneath the photosphere decreases. However, since a weakly twisted toroidal tube is unable to fully emerge, as we see from the solid red line it only reaches 40%, we don't expect the flux on the interior to diminished substantially. This is indeed the case as the percentage of total flux that is in beneath the photosphere by the end of the simulation is around 60%. This inadequate emergence of a weakly twisted toroidal tube doesn't allow any further shearing motion of it, and as a consequence there are no eruptions.

Conclusions

In this work we studied the emergence process in the solar atmosphere, as well as the evolution of that flux related to eruptions. Flux emergence is one of the ways that plasma can be transported from the deeper layers of the Sun to its atmosphere. Flux concentration in areas around the Sun is an important part of the mechanism that describes various eruptive phenomena we observe, such as flares and CMEs. This is why effective transport of magnetic flux is of vital importance in our understanding of the dynamics that shape the Sun.

We investigated the emergence process using numerical simulations, and in particular the Lare3D code, which allowed us to model the stratified solar atmosphere. In particular we used two different geometries for the magnetic flux tubes that are initially placed inside the convection zone, one being horizontal and the other toroidal. Also given the fact that a realistic emerging field is twisted we experimented with different twists. In one case the the field lines wrap around the flux tube by a ratio of $\alpha = 0.4$ and the other by $\alpha = 0.1$.

Among the transient and energetic phenomena observed on the Sun, we focus on studying solar jets. To model this, our numerical simulations include an oblique ambient magnetic field. As the emerging magnetic flux interacts with this ambient field reconnection occurs at their interface, resulting in a standard jet formation, similar to the work of (Yokoyama and Shibata 1996). Additionally, converging and shearing motions along the polarity inversion line lead to the formation of pre-eruptive flux ropes, which can be destabilized and erupt, generating eruption-driven jets. Both of these processes were analyzed in detail for the horizontal and toroidal flux tube configurations. It is worth noting that standard jets were observed in both horizontal and toroidal flux tubes as well as in highly and low twisted field lines, $\alpha = 0.4$ and $\alpha = 0.1$ respectively. However, even though the blowout jet was observed extensively in highly twisted case, when the twist parameter was small, neither flux tube was unable to exhibit an abundance of eruptive blowout jets. In particular the horizontal tube's with $\alpha = 0.1$ only eruption was due to the undulation of the flux tube and serpentine-like emergence, while the toroidal did not erupt at all.

The most important result of this work is the percentage of axial flux of each tube that manages to emerge in comparison to to the percentage that stays beneath the photosphere. In the case of the flux tubes being highly twisted ($\alpha = 0.4$) we see that the horizontal flux tube emerges before the toroidal with its rate of flux transport above the photosphere also reaching a peak faster. This is due to the fact that the horizontal tube becomes lighter faster in the beginning and the buoyancy force allows it to emerge quicker than the toroidal. After the eruptions, the rate with which the horizontal tube transports magnetic flux in the atmosphere is steadily decreasing until eventually it reaches a plateau at around 60% of the total flux. The toroidal emerges later, and the percentage of its axial flux grows slower. However it reaches a higher peak, more than 80% , in comparison with the horizontal that peaks just below that, and it maintains that amount of relative axial flux that is above the photosphere even after its eruptions. A possible explanation for this could be the fact that the toroidal tube's footpoint rotate while simultaneously untwisting its magnetic field line, which produces more axial flux. This kind of untwisting is not observed in the horizontal case so that tube decreases its axial flux after each eruption. Nevertheless, the full mechanism that compensates the toroidal tube's axial flux remains unknown. On the other hand, the percentage of axial flux that stays beneath the photosphere starts to decrease at the same time the emergence begins for each tube. The decrease continuous steadily for both flux tubes with the horizontal one experiencing a much faster loss. Furthermore, after some time the axial flux of the horizontal tube that stays behind doesn't decrease any further and has around 10% of the total flux beneath the photosphere. The toroidal flux tube has a slower decrease rate, and it also has a bigger percentage of axial flux that stays behind even during the later stages of the simulation. The toroidal flux tube's emergence ends with 30% of the total flux staying at the photosphere. The fact that at any given point in time for both flux tubes the sum of the axial flux percentage that stays behind with the one that emerges in the atmosphere doesn't add to 100% is because flux along the y axis may be redirected towards other spacial dimensions and vice versa.

Regarding the low twisted ($\alpha = 0.1$) flux tubes, the difficulty of the horizontal tube and the inability of the toroidal tube to emerge are key points in understanding the amount of axial flux they were able to carry into the atmosphere. More specifically, the horizontal tube started its emergence process before the toroidal and while the rate of axial flux above the photosphere grew fast, it eventually reached a maximum at around 70% of the total flux and dropped slightly at 60% during the late stage of the simulation. The toroidal tube on the other hand not only started emerging much later but also the rate of axial flux that is transported grew much slower than the horizontal and reached a steady rate later on, managing to transport only 40% of the total flux upwards. Concerning the percentage of axial flux that stays behind the photosphere, both flux tubes have loses that appear to increase steadily with the horizontal tube having its percentage of axial flux decrease much more rapidly. Eventually the simulation of the horizontal tube ends with around 35% of the total axial flux at that moment staying beneath the photosphere. On the contrary, 60% of the toroidal's total axial flux didn't emerge. So throughout the simulation at no time did the flux that was transported to the atmosphere exceed the amount of that which stayed behind. In conclusion, when comparing the two different twists, it is clear that the highly twisted flux tube of any kind would be more efficient in transporting magnetic flux in the solar atmosphere as well as exhibiting the kind of eruptive phenomena we observe in the Sun.

Bibliography

Αλυσανδράκης, Κωνσταντίνος, Αλέξανδρος Νίντος, and Σπύρος Πατσουράκος (2016). “*Φυσική του ήλιου και του διαστήματος*”. In.

Acheson, DJ (1979). “Instability by magnetic buoyancy”. In: *Solar Physics* 62, pp. 23–50.

Adams, Mitzi et al. (2014). “A small-scale eruption leading to a blowout macrospicule jet in an on-disk coronal hole”. In: *The Astrophysical Journal* 783.1, p. 11.

Antiochos, SK, CR DeVore, and JA Klimchuk (1999). “A model for solar coronal mass ejections”. In: *The Astrophysical Journal* 510.1, p. 485.

Arber, TD, Martin Haynes, and James E Leake (2007). “Emergence of a flux tube through a partially ionized solar atmosphere”. In: *The Astrophysical Journal* 666.1, p. 541.

Arber, TD, AW Longbottom, et al. (2001). “A staggered grid, Lagrangian–Eulerian remap code for 3-D MHD simulations”. In: *Journal of Computational Physics* 171.1, pp. 151–181.

Arber, Tony, Chris Brady, and Martin Haynes (2018). “Larexd user guide”. In.

Archontis, V, F Moreno-Insertis, et al. (2004). “Emergence of magnetic flux from the convection zone into the corona”. In: *Astronomy & Astrophysics* 426.3, pp. 1047–1063.

Archontis, V and Tibor Török (2008). “Eruption of magnetic flux ropes during flux emergence”. In: *Astronomy & Astrophysics* 492.2, pp. L35–L38.

Archontis, Vasilis and Alan William Hood (2009). “Formation of Ellerman bombs due to 3D flux emergence”. In: *Astronomy & Astrophysics* 508.3, pp. 1469–1483.

— (2010). “Flux emergence and coronal eruption”. In: *Astronomy & Astrophysics* 514, A56.

— (2012). “Magnetic flux emergence: a precursor of solar plasma expulsion”. In: *Astronomy & Astrophysics* 537, A62.

Archontis, Vasilis and Loukas Vlahos (2019). *Introduction to the physics of solar eruptions and their space weather impact.*

Aschwanden, Markus (2006). *Physics of the solar corona: an introduction with problems and solutions.* Springer Science & Business Media.

Ballegooijen, Adrian A van and PCH Martens (1989). “Formation and eruption of solar prominences”. In: *Astrophysical Journal, Part 1 (ISSN 0004-637X), vol. 343, Aug. 15, 1989, p. 971-984.* 343, pp. 971–984.

Benz, Arnold O (2017). “Flare observations”. In: *Living reviews in solar physics* 14, pp. 1–59.

Brown, John C (1973). “On the ionisation of hydrogen in optical flares”. In: *Solar Physics* 29, pp. 421–427.

Carmichael, HUGH (1964). “54 A PROCESS FOR FLARES”. In: *NASA SP.* 50, p. 451.

Chandra, R et al. (2017). “Blowout jets and impulsive eruptive flares in a bald-patch topology”. In: *Astronomy & Astrophysics* 598, A41.

Chandrasekhar, Subrahmanyan and Subrahmanyan Chandrasekhar (1957). *An introduction to the study of stellar structure.* Vol. 2. Courier Corporation.

Chen, PF (2011). “Coronal mass ejections: models and their observational basis”. In: *Living Reviews in Solar Physics* 8.1, pp. 1–92.

Cheung, Mark and Hiroaki Isobe (2014). “Flux emergence (theory)”. In: *Living Reviews in Solar Physics* 11.1, pp. 1–128.

Chouliaras, Georgios, Petros Syntelis, and Vasileios Archontis (2023). “Effects of partial ionization on magnetic flux emergence in the Sun”. In: *The Astrophysical Journal* 952.1, p. 21.

Curto, Juan José (2020). “Geomagnetic solar flare effects: A review”. In: *Journal of Space Weather and Space Climate* 10, p. 27.

DeVore, C Richard and Spiro K Antiochos (2008). "Homologous confined filament eruptions via magnetic breakout". In: *The Astrophysical Journal* 680.1, p. 740.
Emslie, AG et al. (2012). "Global energetics of thirty-eight large solar eruptive events". In: *The Astrophysical Journal* 759.1, p. 71.
Fan, Y (2001). "The emergence of a twisted Ω-tube into the solar atmosphere". In: *The Astrophysical Journal* 554.1, p. L111.
Forbes, TG and ER Priest (1984). "Numerical simulation of reconnection in an emerging magnetic flux region". In: *Solar physics* 94, pp. 315–340.
Galsgaard, K et al. (2007). "The effect of the relative orientation between the coronal field and new emerging flux. I. Global properties". In: *The Astrophysical Journal* 666.1, p. 516.
Gary, G Allen (2001). "Plasma beta above a solar active region: rethinking the paradigm". In: *Solar Physics* 203, pp. 71–86.
Goedbloed, JP Hans and Stefaan Poedts (2004). *Principles of magnetohydrodynamics: with applications to laboratory and astrophysical plasmas.* Cambridge university press.
Gou, Tingyu et al. (2024). "High-Resolution Observation of Blowout Jets Regulated by Sunspot Rotation". In: *Solar Physics* 299.7, p. 99.
Harvey, K and J Harvey (1973). "Observations of moving magnetic features near sunspots". In: *Solar Physics* 28, pp. 61–71.
Heyvaerts, Jean, Eric R Priest, and David M Rust (1977). "An emerging flux model for the solar flare phenomenon". In: *Astrophysical Journal, Part 1, vol. 216, Aug. 15, 1977, p. 123-137.* 216, pp. 123–137.
Hirayama, T (1974). "Theoretical model of flares and prominences: I: Evaporating flare model". In: *Solar Physics* 34, pp. 323–338.
Hood, Alan William et al. (2009). "The emergence of toroidal flux tubes from beneath the solar photosphere". In: *Astronomy & Astrophysics* 503.3, pp. 999–1011.
Isobe, Hiroaki et al. (2005). "Filamentary structure on the Sun from the magnetic Rayleigh–Taylor instability". In: *Nature* 434.7032, pp. 478–481.
Jacobs, Carla and Stefaan Poedts (2011). "Models for coronal mass ejections". In: *Journal of atmospheric and solar-terrestrial physics* 73.10, pp. 1148–1155.
Ji, Hantao et al. (1999). "Magnetic reconnection with Sweet-Parker characteristics in two-dimensional laboratory plasmas". In: *Physics of Plasmas* 6.5, pp. 1743–1750.
Joshi, Reetika et al. (2020). "Case study of multi-temperature coronal jets for emerging flux MHD models". In: *Astronomy & Astrophysics* 639, A22.
Knizhnik, Kalman J et al. (2021). "The Rise and Emergence of Untwisted Toroidal Flux Ropes on the Sun". In: *The Astrophysical Journal* 907.1, p. 19.
Kontar, EP et al. (2017). "Turbulent kinetic energy in the energy balance of a solar flare". In: *Physical Review Letters* 118.15, p. 155101.
Kopp, RA and GW Pneuman (1976). "Magnetic reconnection in the corona and the loop prominence phenomenon". In: *Solar Physics* 50, pp. 85–98.
Li, LP et al. (2012). "Study of the first productive active region in solar cycle 24". In: *Astronomy & Astrophysics* 539, A7.
Lin, J and TG Forbes (2000). "Effects of reconnection on the coronal mass ejection process". In: *Journal of Geophysical Research: Space Physics* 105.A2, pp. 2375–2392.
Liu, Chang et al. (2011). "A standard-to-blowout jet". In: *The Astrophysical Journal Letters* 735.1, p. L18.
MacTaggart, David and Alan W Hood (2009). "On the emergence of toroidal flux tubes: general dynamics and comparisons with the cylinder model". In: *Astronomy & Astrophysics* 507.2, pp. 995–1004.
Manchester IV, W et al. (2004). "Eruption of a buoyantly emerging magnetic flux rope". In: *The Astrophysical Journal* 610.1, p. 588.
Martínez-Sykora, Juan, Viggo Hansteen, and Mats Carlsson (2008). "Twisted flux tube emergence from the convection zone to the corona". In: *The Astrophysical Journal* 679.1, p. 871.
Matsumoto, R et al. (1993). "Three-dimensional magnetohydrodynamics of the emerging magnetic flux in the solar atmosphere". In: *Astrophysical Journal, Part 1 (ISSN 0004-637X), vol. 414, no. 1, p. 357-371.* 414, pp. 357–371.
McKenzie, David E and Richard C Canfield (2008). "Hinode XRT observations of a long-lasting coronal sigmoid". In: *Astronomy & Astrophysics* 481.1, pp. L65–L68.

Moore, Ronald L, Jonathan W Cirtain, et al. (2010). "Dichotomy of solar coronal jets: standard jets and blowout jets". In: *The Astrophysical Journal* 720.1, p. 757.

Moore, Ronald L, Alphonse C Sterling, David A Falconer, et al. (2013). "The cool component and the dichotomy, lateral expansion, and axial rotation of solar X-ray jets". In: *The Astrophysical Journal* 769.2, p. 134.

Moore, Ronald L, Alphonse C Sterling, Hugh S Hudson, et al. (2001). "Onset of the magnetic explosion in solar flares and coronal mass ejections". In: *The Astrophysical Journal* 552.2, p. 833.

Moreno-Insertis, F (2006). "Flux Emergence from the Solar Interior to the Atmosphere: the Passage through the Photosphere". In: *Solar MHD Theory and Observations: A High Spatial Resolution Perspective.* Vol. 354, p. 183.

Moreno-Insertis, F, K Galsgaard, and I Ugarte-Urra (2008). "Jets in coronal holes: Hinode observations and three-dimensional computer modeling". In: *The Astrophysical Journal* 673.2, p. L211.

Moreno-Insertis, Fernando and Klaus Galsgaard (2013). "Plasma jets and eruptions in solar coronal holes: a three-dimensional flux emergence experiment". In: *The Astrophysical Journal* 771.1, p. 20.

Murray, Micheal J, Lidia van Driel-Gesztelyi, and Deborah Baker (2009). "Simulations of emerging flux in a coronal hole: oscillatory reconnection". In: *Astronomy & Astrophysics* 494.1, pp. 329–337.

Murray, MJ et al. (2006). "3D simulations identifying the effects of varying the twist and field strength of an emerging flux tube". In: *Astronomy & Astrophysics* 460.3, pp. 909–923.

Newcomb, William A (1961). "Convective instability induced by gravity in a plasma with a frozen-in magnetic field". In: *The Physics of Fluids* 4.4, pp. 391–396.

Nordlund, Åke, Robert F Stein, and Martin Asplund (2009). "Solar surface convection". In: *Living Reviews in Solar Physics* 6.1, pp. 1–117.

Nozawa, S et al. (1992). "Emergence of magnetic flux from the convection zone into the solar atmosphere. I-Linear and nonlinear adiabatic evolution of the convective-Parker instability". In: *Astrophysical Journal Supplement Series (ISSN 0067-0049), vol. 78, Jan. 1992, p. 267-282. Research supported by Japan Society for Promotion of Science.* 78, pp. 267–282.

Pariat, Etienne, Sophie Masson, and Guillaume Aulanier (2009). "Current buildup in emerging serpentine flux tubes". In: *The Astrophysical Journal* 701.2, p. 1911.

Parker, Eugene N (1955). "The Formation of Sunspots from the Solar Toroidal Field." In: *Astrophysical Journal, vol. 121, p. 491* 121, p. 491.

Patsourakos, S et al. (2008). "STEREO SECCHI stereoscopic observations constraining the initiation of polar coronal jets". In: *The Astrophysical Journal* 680.1, p. L73.

Priest, Eric (2014). *Magnetohydrodynamics of the Sun.* Cambridge University Press.

Raouafi, NE et al. (2016). "Solar coronal jets: observations, theory, and modeling". In: *Space Science Reviews* 201, pp. 1–53.

Scherrer, P H, R S Bogart, et al. (1995). "The solar oscillations investigation—Michelson Doppler imager". In: *The soho mission*, pp. 129–188.

Scherrer, P H, Jesper Schou, et al. (2012). "The helioseismic and magnetic imager (HMI) investigation for the solar dynamics observatory (SDO)". In: *Solar Physics* 275, pp. 207–227.

Schmieder, Brigitte (2022). "Solar jets: SDO and IRIS observations in the perspective of new MHD simulations". In: *Frontiers in Astronomy and Space Sciences* 9, p. 820183.

Schou, Jørgen et al. (2012). "Design and ground calibration of the Helioseismic and Magnetic Imager (HMI) instrument on the Solar Dynamics Observatory (SDO)". In: *Solar Physics* 275, pp. 229–259.

Shen, Yuandeng (2021). "Observation and modelling of solar jets". In: *Proceedings of the Royal Society A* 477.2246, p. 20200217.

Shen, Yuandeng et al. (2012). "On a coronal blowout jet: the first observation of a simultaneously produced bubble-like CME and a jet-like CME in a solar event". In: *The Astrophysical Journal* 745.2, p. 164.

Shibata, Kazunari, Yoshinori Ishido, et al. (1993). "Observations of X-ray jets using Yohkoh soft X-ray telescope". In: *International Astronomical Union Colloquium.* Vol. 141. Cambridge University Press, pp. 343–346.

Shibata, Kazunari and Tetsuya Magara (2011). "Solar flares: magnetohydrodynamic processes". In: *Living Reviews in Solar Physics* 8.1, pp. 1–99.

Sigalotti, Leonardo Di G and Fidel Cruz (2023). "Unveiling the mystery of solar-coronal heating". In: *Physics Today* 76.4, pp. 34–40.

Steinhilber, Friedhelm and Jürg Beer (2011). "Solar activity–the past 1200 years". In: *PAGES news* 19.1, pp. 5–6.

Strous, LH, G Scharmer, and TD Tarbell (1996). "Title, AM, and Zwaan, C". In: *Phenomena in an emerging active region. I. Horizontal dynamics*, pp. 947–959.

Sturrock, PA (1966). "Model of the high-energy phase of solar flares". In: *Nature* 211.5050, pp. 695–697.

Sturrock, Zoe et al. (2015). "Sunspot rotation-i. a consequence of flux emergence". In: *Astronomy & Astrophysics* 582, A76.

Syntelis, P, V Archontis, and K Tsinganos (2017). "Recurrent CME-like eruptions in emerging flux regions. I. On the mechanism of eruptions". In: *The Astrophysical Journal* 850.1, p. 95.

Syntelis, P., V. Archontis, and A. Hood (Mar. 2019). "Successful and Failed Flux Tube Emergence in the Solar Interior". In: *The Astrophysical Journal* 874.1, p. 15. ISSN: 1538-4357. DOI: 10.3847/1538-4357/ab0959. URL: http://dx.doi.org/10.3847/1538-4357/ab0959.

Syntelis, Petros et al. (2015). "Emergence of non-twisted magnetic fields in the Sun: Jets and atmospheric response". In: *Astronomy & Astrophysics* 584, A10.

Tandberg-Hanssen, Einar and A Gordon Emslie (1988). *The physics of solar flares.* Vol. 14. Cambridge University Press.

Tang, Zehao et al. (2021). "Sympathetic standard and blowout coronal jets observed in a polar coronal hole". In: *The Astrophysical Journal Letters* 912.1, p. L15.

Toriumi, Shin, Yukio Katsukawa, and Mark CM Cheung (2017). "Various local heating events in the earliest phase of flux emergence". In: *The Astrophysical Journal* 836.1, p. 63.

Wachter, R et al. (2012). "Image quality of the helioseismic and magnetic imager (HMI) onboard the solar dynamics observatory (SDO)". In: *The Solar Dynamics Observatory*, pp. 261–284.

Watanabe, H et al. (2008). "Spectropolarimetric observation of an emerging flux region: triggering mechanisms of Ellerman bombs". In: *The Astrophysical Journal* 684.1, p. 736.

Wyper, Peter F, Spiro K Antiochos, and C Richard DeVore (2017). "A universal model for solar eruptions". In: *Nature* 544.7651, pp. 452–455.

Yokoyama, Takaaki and Kazunari Shibata (1996). "Numerical simulation of solar coronal X-ray jets based on the magnetic reconnection model". In: *Publications of the Astronomical Society of Japan* 48.2, pp. 353–376.

Young, Peter R and Karin Muglach (2014). "A coronal hole jet observed with Hinode and the Solar Dynamics Observatory". In: *Publications of the Astronomical Society of Japan* 66.SP1, S12.